The Effect of Manufacturing Tolerances and Header Design on Heat Exchanger Effectiveness

by

Charles Booten

B.S. Mechanical Engineering,
Massachusetts Institute of Technology (2000)

Submitted to the Department of Mechanical Engineering
in partial fulfillment of the requirements for the degree of

Master of Science in Mechanical Engineering

at the

MASSACHUSETTS INSTITUTE OF TECHNOLOGY

May 2001

Author ....
Department of Mechanical Engineering
May 11, 2001

Certified by ....
David Gordon Wilson
Professor of Mechanical Engineering, Emeritus
Thesis Supervisor

Accepted by ....
Ain Sonin
Chairman of Graduate Studies
Department of Mechanical Engineering

The Effect of Manufacturing Tolerances and Header Design on Heat Exchanger Effectiveness

by

Charles Booten

Submitted to the Department of Mechanical Engineering
on May 11, 2001, in partial fulfillment of the
requirements for the degree of
Master of Science in Mechanical Engineering

Abstract

This study seeks to analyze the effect of manufacturing defects and inlet header design on the effectiveness of heat exchangers. A commercial computational fluid dynamics code, FLUENT 5.4, was used to numerically simulate individual and pairs of passages as well as sections of an inlet header and heat-exchanger core. The one- and two-passage models show that the four representative manufacturing defects do not have a large impact on overall effectiveness, even when the defects are quite large relative to the passage dimensions. The core and header sections showed that the basic header contour and the angle of the incoming flow as well as the pressure drop through the core have a significant impact on the flow distribution. Small variations in the header dimensions and the core/header aspect ratio have little effect on the effectiveness. Decreasing the angle the incoming flow turns through and increasing the pressure drop through the core both create a more even flow distribution through the heat exchanger, hence increasing its effectiveness.

Thesis Supervisor: David Gordon Wilson
Title: Professor of Mechanical Engineering, Emeritus

Acknowledgements

I would like to thank Prof. Wilson for his guidance and patience with my work. He is the standard by which I judge other researchers and is, in all respects, a first-rate (the hyphen is for you Dave) person. I am also very grateful to Ford Motor Co. for the fellowship that made this research possible. I would like to thank Fluent Inc., and especially Ruth Shepard, who were very generous in allowing me to use their CFD code. None of this work would have been possible without these people and organizations.

Contents

List of Figures

List of Tables

Nomenclature

A=surface area

A_c= cross-sectional area

a_P= coefficient used in linearizing governing equations in FLUENT

b= coefficient used in linearizing governing equations in FLUENT

c_1= constant 1.44 in standard and realizable k-ϵ models and 1.42 in the RNG model

c_2= constant 1.92 in standard and realizable k-ϵ models and 1.68 in the RNG model

C_{ij}= 3x3 diagonal matrix specified by user to account for viscous momentum loss

c_p= heat capacitance per unit mass, if sub j' is for species j'

C_μ= constant in turbulence models, default value 0.09 in standard k-ϵ model and 0.0845 in RNG k-ϵ model

D_h= hydraulic diameter, $\frac{4A_c}{Perimeter}$

D_{ij}= 3x3 diagonal matrix specified by user to account for inertial momentum loss

E= energy, also constant equal to 9.793 in equations 2.28, 2.67 and 2.69

F_i= momentum source term added in porous medium model (equation 2.12)

f= Darcy friction factor (equation 2.6)

G = mass-flow rate per unit area (equation 2.1)

G_k= generation of turbulent kinetic energy due to mean velocity gradients [16]

G_b= generation of turbulent kinetic energy due to bouyancy [16]

Y_m= contribution of the fluctuating dilitation in compressible turbulence to turbulent dissipation rate [16]

g_c= proportionality factor in Newton's second law

$h_{j'}$= enthalpy per unit mass of species j'

$\bar{h}$= average heat-transfer coefficient

I= turbulence intensity equation 2.77, also identity matrix in equation 2.51

$J_{j'}$= diffusion flux of species j' in equation 2.15

k= turbulent kinetic energy in k-ϵ turbulence model(defined equation 2.47), sub f is thermal conductivity in fluid, sub P is turbulent kinetic energy at point P

K_c= exit loss coefficient (see Appendix B)

K_e= entrance loss coefficient (see Appendix B)

k_{eff}= effective thermal conductivity of fluid accounting for turbulent enhancement (equation 2.17)

k_T= turbulent thermal conductivity (equation 2.18)

L= length

L_{ch}= characteristic length scale

$\dot{m}$= mass-flow rate

Nu= Nusselt number

P= static pressure

Pr_T= turbulent Prandtl number, default value 0.85 in standard and realizable k-ϵ models

Q= heat transfer rate

q''= heat flux

R= radius of curvature of streamline, also Reynolds stress tensor in equation 2.49, gas constant in equation 3.4

Re= Reynolds number (equation 2.5)

r_h= hydraulic radius, $\frac{D_h}{2}$

S= sub h is energy source term in equation 2.15, sub $\phi$is source term per unit volume of a scalar ϕ

T= temperature

T^*= dimensionless temperature (equation 2.28)

t= time

U= velocity vector in equation 2.49

u= velocity

u_T= friction velocity

u'= velocity fluctuation

V= volume

$\mathbf{v}$= velocity vector

y= distance from wall

y_v= viscous sublayer thickness

$y^*{}_v$= constant equal 11.225

y^*= dimensionless distance from wall

$y^*{}_T$= non-dimensional thermal sublayer thickness

z= height along direction of gravitational acceleration

Greek

$\alpha= \frac{1}{Pr_T}$, also is the under relaxation factor in equation 2.46

Γ_ϕ= diffusion coefficient of scalar ϕ

$\frac{\partial}{\partial n}$= derivative normal to the streamline along radial direction

$\frac{\partial}{\partial s}$= derivative along the streamline coordinates

δP= static pressure drop

ϵ= heat-exchanger effectiveness in equation 2.36, also turbulent dissipation rate in k-ϵ models in equation 2.48

κ= Von Karman constant, default value in FLUENT of 0.42

λ_k= Kolmogorov turbulence length scale

μ= molecular viscosity

μ_T= turbulent viscosity (equation 2.19)

$\mu_{eff}= \mu + \mu_T$

ν= velocity, sub m is mean, sub 1 or 2 is entrance or exit respectively (equation 2.1), kinematic viscosity in equation 2.48

ν_T= eddy viscosity

ϕ= arbitrary scalar quantity

ρ= density

σ= ratio of open area to total area of surface (i.e. porosity)

τ_t= shear stress in fluid

τ_w= wall shear stress

τ_{ij}= deviatoric stress tensor in fluid [16]

Chapter 1

Introduction

Modern regenerators are used to transfer heat in a variety of applications. Regenerators are essential components in many industrial processes and power generation. Rotary regenerators are used primarily in gas-turbine applications, both stationary and mobile. Even with such an apparently narrow focus, much of the research presented here can be generalized for application to many types of regenerators and other matrix based product like catalytic converters.

1.1 Regenerator Background

The idea of reusing the heat from combustion is an old one, essentially as old as human control of fire. Modern regenerator application became widespread, however, with its application to glass-making in 1856 by Friedrich Siemens. The idea of applying the regenerator to the smelting of iron ore was facilitated by his brother Sir Charles Siemens with the invention of the open-hearth furnace in 1861. Peirre and Emile Martin first applied the technology in 1864 in France. The result was a quality of steel superior to that of Bessemer Steel. Edward Cowper used the idea in 1860 to patent a hot or Cowper stove that heats the air before going into a blast furnace [3].

Figures 1-1 and 1-2 show an early Cowper stove [40]. The hot gas enters through the center chimney and then passes through the checkered refractory bricks to transfer heat to them. When the bricks have been sufficiently heated, the exhaust valve is

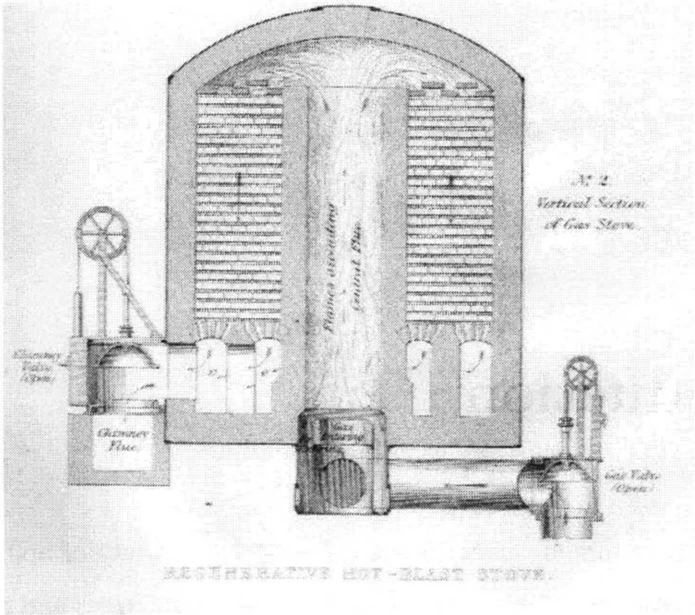

Figure 1-1: An early Cowper Stove with refractory being heated by exhaust from a blast furnace [21]

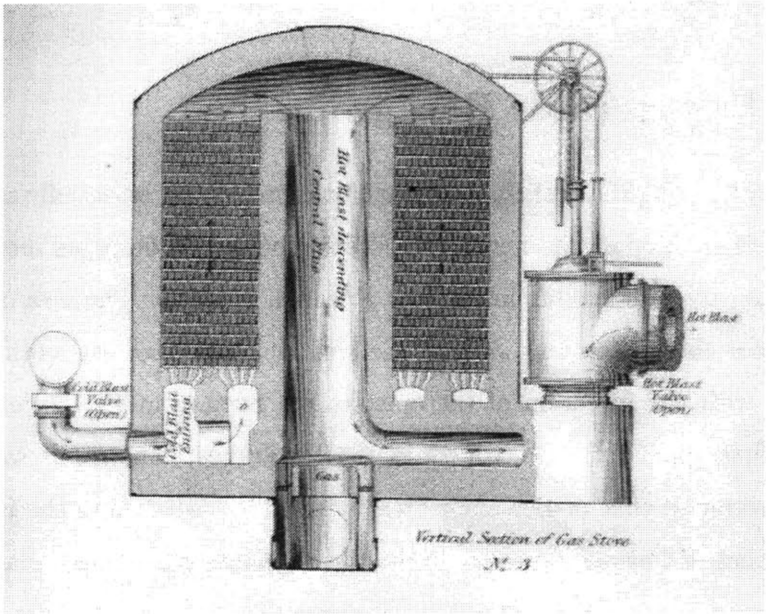

Figure 1-2: An early Cowper Stove providing heated air as a "blast" to a furnace [21]

closed and the flow is reversed allowing cool air to enter the stove, extracting the heat from the brick and sending it to the blast furnace to facilitate combustion. Cowper Stoves and blast furnaces were made very large: by 1890 some were as large as 16 ft. in diameter and 75 ft. high capable of heating 20,000 cubic feet of air per minute to 1500° Fahrenheit (815°C) [2]. Modern stoves can be as much as 10 m in diameter and 40 m high capable of heating air to over 1200° Centigrade for over 40 minutes.

1.2 Rotary Regenerators

The first rotary regenerator was developed by Fredrik Ljungstrom in 1920. It was used to recover the heat from gases in steam power plants to preheat air before reaching the combustion chamber. This provided up to a 20% savings in fuel cost. Today these pre-heaters are still widely used in power generation as well as a variety of other situations where high-efficiency heat removal is required, from gas and steam turbines to swimming-pool heating [19]. The largest rotary regenerators, sometimes called heat wheels, can be up to 10 m in diameter. The first application of rotary regenerators to gas turbines was at the National Gas Turbine Establishment in Britain in the 1940s. Development was soon discontinued, however. Early rotary regenerators were made from essentially corrugated stainless wound tightly in a circle between flat sheets. By the 1960s ceramic materials were being used to produce matrix type regenerators as in Figure 1-3.

In 1963 Chrysler tested 50 prototype cars with regenerative gas-turbine engines. One of the major problems with the gas turbines was the high production cost. Gas turbines at the time cost approximately $8 per horsepower where spark-ignition engines could be produced for around $1.50. The high cost was primarily due to the expensive alloys; the nickel-chromium-cobalt alloys used for the regenerator were a significant part of this cost. Chrysler decided not to produce the cars after a three-month test period where the cars were driven by selected members of the public [48]. Regenerator development was continued by Corning Glass. A Corning ceramic regenerator was used as part of the gas-turbine-powered car made by Rover and BRM

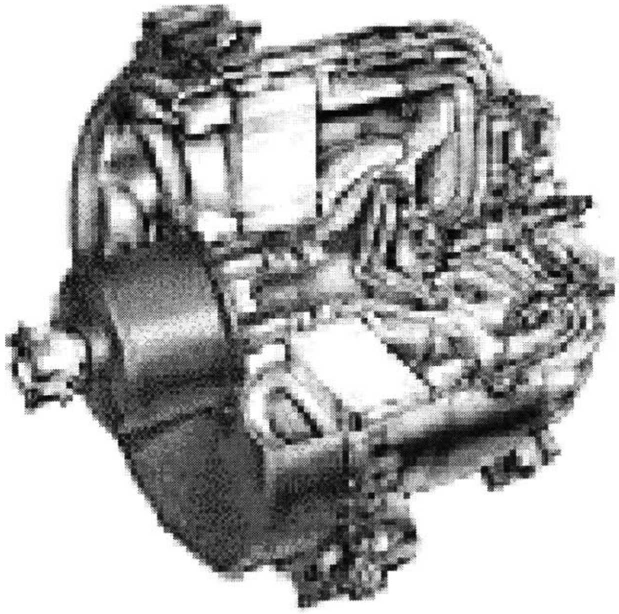

Figure 1-3: AGT-101 gas turbine

for the 1963 Le Mans road race. The car ran well in the race, finishing 7th and being beaten by 6 Ferraris, but subsequent attempts to improve on this performance by Rover-BRM were unsuccessful and gas-turbine development was soon discontinued [32]. Other attempts have been made to develop an automotive gas turbine that is competitive with conventional diesel and spark-ignition engines. The Garrett and Ford Motor Co. developed a prototype engine, the AGT-101 shown in Figure 1-3 in the 1970s.

Research was done on using ceramic components when possible to reduce production cost and increase fuel economy. The Garrett/Ford AGT-101 had a ceramic radial-inflow turbine rotor, regenerator and even some bolts [33]. Ford decided not to continue research into gas-turbines after developing the AGT-101 because of the expense and complications in large-scale production of the engines. Lycoming developed the AGT-1500 gas turbine engine, which is the only automotive turbine in production, to be used in the MI Abrams tank. It is a three-shaft recuperated engine and is shown in Figure 1-4. The stainless-steel recuperator had an effectiveness of

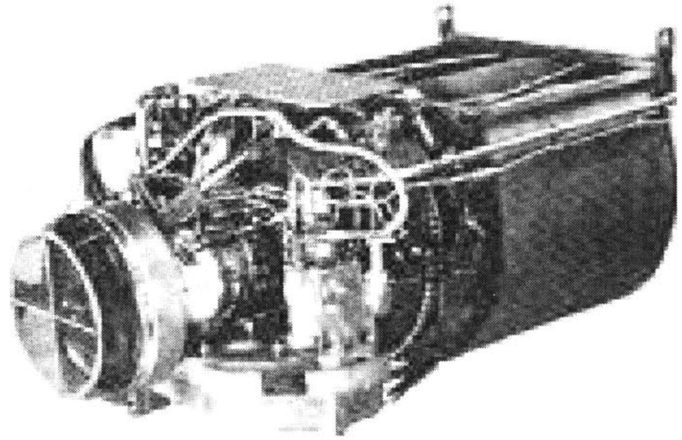

Figure 1-4: Lycoming AGT-1500 gas turbine

approximately 68% and also had a short life expectancy.

1.3 Current Regenerator Research

1.3.1 Materials

Current regenerator research is focused on improving the performance of ceramic regenerators rather than improving on metallic ones. This is in part because of the extreme temperatures that current gas turbines operate at. The turbine outlet gas temperature can be as high as 1000° Celsius [21][11]. Other factors that are important to regenerator performance are strength, chemical resistance, thermal expansion and manufacturing cost. There are a select few materials that are currently being investigated for possible use in regenerators [11][29][10][25]:

- aluminosilicates (AS)
- lithium aluminosilicates (LAS)
- magnesium aluminosilicates (MAS)
- aluminum titanates (AT)

- zirconium phosphates (NZP)

Aluminosilicates (AS) are among the most widely used and well tested of these materials. They have very low thermal expansion coefficients and thermal conductivity with moderate strength. The operation temperatures (1000° C) are marginal for today's gas turbines. AS products require three firings plus machining for a relatively high cost.

Lithium aluminosilicates (LAS) have been in use since the 1940s; the first ceramic regenerators were LAS. They are commonly known under brand names like Corning Ware and Visions. They have low thermal expansion coefficients and high temperature capability (1200° C), but still require two firings and machining. They are also susceptible to chemical corruption from sulphur in exhaust and from road salts.

Magnesium aluminosilicates (MAS) also known as cordierite were developed in the 1970's for automotive catalytic converters. Cordierite has a moderate thermal expansion coefficient, moderate strength, low thermal conductivity and a high maximum use temperature (1200° C). There is anisotropy in the thermal expansion and fatigue is also a concern because of the micro-cracks inherent in the crystal structure.

Aluminum titanate (AT) was also developed for automotive catalytic converters. Operating temperatures are higher than necessary for regenerators but cycling effects are a concern. The chemical reactivity of the titanium with iron is also of concern.

Zirconium phosphates (NZP)have not been studied as much as the other materials. They most likely have the thermal expansion and operating temperature characteristics that are necessary but are quite expensive ($100 per pound) and their chemical durability under these conditions is not well established.

1.3.2 Header Design

There is also interest in improving regenerator efficiency by improving the flow distribution into the regenerator. Improving header designs is vital to increasing the heat-exchanger effectiveness of rotary regenerators. Header design can also be generalized to apply in different circumstances such as stationary heat exchangers and automotive catalytic converters. It has been known for some time that the design of inlet headers has a dramatic impact on the flow distribution through a heat exchanger[45][20]. Inlet headers have still commonly been designed without significant regard to the flow distribution they create in the heat exchanger or regenerator, especially in gas turbines where the complexity of the design may require compromises that detract from optimal header design. There has been research, however, attempting to quantify the effects of flow distribution on heat-exchanger performance [8][38][50]. There has also been some work on how to design inlet headers to achieve a more even flow distribution in heat exchangers and catalytic converters [45][14][44]. However, none of these has covered enough of a range in inlet-header designs and configurations to be of satisfactory use to a designer.

1.3.3 Seal Design

Rotary regenerators have a further problem of seal wear. The rotating nature of these regenerators means that there is constant slipping and friction between the seal and the regenerator itself. Over a period of time this can lead to a a leakage of over 15% [13]. A recent patent obtained by the Massachusetts Institute of Technology has demonstrated a potential improvement in the area of seal leakage. The patent is for a seal and regenerator system that discontinuously rotates. When the seal moves with respect to the regenerator it pulls slightly away so as to reduce friction and then rotates and forces itself against the matrix to create a tight seal again [46].

1.3.4 Thesis Research

The work presented in this thesis is to determine the effect of manufacturing tolerances and header design on the effectiveness of rotary regenerators. FLUENT, a commercial computational fluid-dynamics code (CFD) was used to perform numerical analysis of many types of manufacturing inaccuracies, flow maldistributions and inlet-header designs.

Manufacturing Inaccuracies

Extruded ceramic matrices can develop variable passage sizes or shapes during the curing process or even during extrusion. The non-uniformities studied here include

- different channel aspect ratios and size
- variation of channel width in the direction of fluid flow
- corner radii

Small variations in any of these areas can potentially be important because of the demand for very high regenerator effectiveness in many smaller turbine applications [48].

Inlet-Header Effects

The impact of different inlet-header configurations was also analyzed. Typically regenerators do not have a straight-conical-diffuser-type inlet header. Geometrical constraints usually require tight bends and large area changes in the inlet pipe and header over short distances that can result in an uneven distribution of flow through the regenerator. The effect of the angle of incoming flow was studied as well as header curvature to determine the effect on the flow distribution into the regenerator and pressure drop through the inlet header. Typical velocities into regenerator passages are 5-10 m/s with a pressure drop on the order of 3000 Pa. The velocities out of the compressor can be from 100-200 m/s before entering the inlet header.

Chapter 2

Mathematical Correlations

There are several aspects of the simulations that were analyzed and compared to theoretical predictions to ascertain the trustworthiness of the numerical results. Pressure differences including streamline-curvature and entrance and exit effects are important to the regenerator designer and were bench-marked whenever possible. The heat transfer into passages is directly related to the regenerator effectiveness and was also studied carefully. Finally the numerical modeling techniques are examined to determine the most appropriate method of simulating the regenerators.

2.1 Pressure-Drop Calculations

2.1.1 Straight Passages

The pressure drop associated with flow through a heat-exchanger core can be expressed as [36]

$$\frac{\Delta P}{P_1} = \frac{G^2 \nu_1}{2 g_c P_1}[(K_c + 1 - \sigma^2) + 2(\frac{\nu_2}{\nu_1} - 1) + f\frac{A}{A_c}\frac{\nu_m}{\nu_1} - (1 - \sigma^2 - K_e)\frac{\nu_2}{\nu_1}] \tag{2.1}$$

where the terms inside the brackets account for entrance effects, flow acceleration, core friction and exit effects respectively. The porosity, or ratio of free flow area to total surface area of the entrance of the core is σ and the entrance and exit loss coefficients K_c and K_e have been established analytically for a few geometries and are presented in Appendix B [49]. The surface area of a given passage is A and A_c is the cross-sectional area of that passage. Their ratio can be expressed as

$$\frac{A}{A_c} = \frac{L}{r_h} \tag{2.2}$$

where r_h is the hydraulic radius. G is the mass flow rate per unit area. Therefore the coefficient on the right-hand side of equation 2.1 can be interpreted as

$$\frac{G^2 \nu_1}{2 g_c P_1} = \frac{\frac{V_1^2}{2g_c}}{\frac{P_1}{\rho_1}} = \frac{\textit{dynamic head}}{\textit{static head}} \tag{2.3}$$

It is common to neglect entrance and exit effects because they normally constitute only a few percent of the total-pressure drop. If only the passages are considered, rather than including the up and downstream hardware, then all the terms in equation 2.1 are zero except the core-friction term. Equation 2.2 can then be substituted into equation 2.1 and rearranged to obtain

$$\Delta P = \frac{1}{2} f \rho \frac{L}{D_h} V^2 \tag{2.4}$$

Using the definition of the Reynolds Number (Re)

$$Re \equiv \frac{\rho V D}{\mu} \tag{2.5}$$

and substituting into equation 2.4 yields

$$fRe = 2 \frac{\Delta P \rho A_c D_h^2}{\dot{m} \mu L} \tag{2.6}$$

where f is the Darcy friction factor for the conditions in the channel. Equation 2.6 is a convenient non-dimensional form for comparing the frictional effects for fully developed flow in straight passages.

2.1.2 Streamline Curvature

Streamline-curvature effects on pressure distribution are important in situations where non-uniform passages cause the flow field to bend at the entrance and exit. Many of the simulations have a plenum chamber where the flow enters and then splits into different passages. It is in the entrance region that the streamline curvature produces pressure gradients normal to the flow. Most research that has been published on pressure drops in regenerators neglects entrance effects of this nature; however, it was deemed important to be able to see how well FLUENT simulated this type of situation.

The Euler equations for incompressible and inviscid flow are

$$\frac{\partial}{\partial s}\left(\frac{P}{\rho}+\frac{V^2}{2}+\rho g z\right)=0 \tag{2.7}$$

$$\frac{\partial}{\partial n}(P+\rho g z)=\frac{\rho V^2}{R} \tag{2.8}$$

where the s-direction is along the streamline and the n-direction is normal to the streamline in the radial direction. The flow velocities are small enough to assumer incompressibility, see Appendix A. The gravitational potential energy change from one position to another can be neglected when the change in height is very small compared to the static pressure drop as the case is here. If the velocity is approximately constant along a streamline, which is true if the pressure is approximately constant along the streamline, equation 2.8 can be integrated

$$\int_{P_o}^{P_R} \partial P = \int_{R_0}^{R} \frac{\rho V^2}{r} \partial r \tag{2.9}$$

giving

$$P_R - P_0 = \rho V^2 \ln\left(\frac{R}{R_0}\right) \tag{2.10}$$

Equation 2.10 can be used to calculate the expected pressure gradient given the radii of curvature that is produced in the FLUENT simulation.

2.1.3 Porous Media

The computational expense of modeling a large section of regenerator and the complexity of modeling the laminar flow through the regenerator and the highly turbulent flow in the headers simultaneously is prohibitive. A porous medium was used to represent the regenerator instead. FLUENT defines a porous medium as region where the momentum equations can be written

$$\frac{\partial}{\partial t}(\rho u_i) + \frac{\partial}{\partial x_j}(\rho u_i u_j) = -\frac{\partial P}{\partial x_i} + \rho g_i + F_i \tag{2.11}$$

where F_i is a momentum source/sink term that is defined by the user in FLUENT. Equation 2.11 is the Navier-Stokes equations using Einstein summation notation with the addition of a source term, F_i. F_i has two parts, a viscous and an inertial term. It is defined in FLUENT as

$$F_i \equiv \sum_{i=1}^{3} D_{ij}\mu V_j + \sum_{i=1}^{3} C_{ij}\frac{1}{2}\rho \mid v_j \mid v_j \tag{2.12}$$

The user defines the terms in the diagonal matrices C_{ij} and D_{ij} to achieve the desired pressure drop through the medium in any direction. They can be represented by

$$C_{ij} = \begin{bmatrix} C_x & 0 & 0 \\ 0 & C_y & 0 \\ 0 & 0 & C_z \end{bmatrix} \tag{2.13}$$

$$D_{ij} = \begin{bmatrix} D_x & 0 & 0 \\ 0 & D_y & 0 \\ 0 & 0 & D_z \end{bmatrix} \tag{2.14}$$

In order to define the porous media as accurately as possible the total static-pressure drop desired was split into an inertial and a viscous component. This was achieved by using the ratio of the flow-acceleration and the core friction terms in equation 2.1 to assign fractions of overall pressure drop to both terms in equation 2.12. Each term was then solved for the respective constant. Only the z-direction was considered because in an actual regenerator the flow is totally in that direction. The other entries in the diagonal matrices C_{ij} and D_{ij} were artificially set to values several orders of magnitude higher than for the z-direction. This ensured that the flow was forced in the z-direction because flow in the x or y directions would have required enormous pressure gradients which do not exist.

The porosity of the porous medium is also specified by the user. A regenerator is not truly a porous medium, so the ratio of open face area to the total face area was substituted as the porosity. Ceramic regenerators and other extruded matrix monoliths such as catalytic-converter cores have a porosity in the range 0.58-0.78 [20][10]. All the porous media in this study were modeled with a porosity of 0.7, a common value for gas-turbine regenerators.

2.2 Heat Transfer

Many of the simulations included heat transfer into or out of the passages through the walls. It is therefore helpful to understand how FLUENT calculates heat transfer given the particular boundary conditions imposed by the user and then to see how best to check the validity of the numerical results.

2.2.1 Energy Equation

FLUENT uses the energy equation for an inertial reference frame in the form

$$\frac{\partial}{\partial t}(\rho E) + \frac{\partial}{\partial x_i}(u_i(\rho E + P)) = -\frac{\partial}{\partial x_i}(k_{eff}\frac{\partial T}{\partial x_i} - \sum_{j'} h_{j'}J_{j'} + u_j(\tau_{ij})_{eff}) + S_h \quad (2.15)$$

$J_{j'}$ is the diffusion flux of species j' and S_h is a source term containing viscous dissipation (if applicable) and any other sources defined by the user. $h_{j'}$ is defined as

$$h_{j'} \equiv \int_{T_{ref}}^{T} c_{p,j'}dT \quad (2.16)$$

where T_{ref} is set at a default of 298.15° C. k_{eff} is the effective conductivity of the fluid defined as

$$k_{eff} \equiv k + k_T \quad (2.17)$$

where k_T is the turbulent thermal conductivity defined by the turbulence model being used; it is zero for laminar flow. The k-ϵ models (see section 2.3.2) define it as

$$k_T \equiv \frac{\rho c_P \mu_T}{Pr_T} \quad (2.18)$$

where μ_T is the turbulent viscosity defined as

$$\mu_T \equiv C_\mu \bar{\rho}\frac{k^2}{\epsilon} \quad (2.19)$$

and $Pr_T = 0.85$ by default in the standard and realizable k-ϵmodels. Pr_T in the RNG model (see section 2.3.2) is calculated from

$$\mu_T^{-1} = |\frac{\alpha - 1.3929}{.3929}|^{.6321}|\frac{\alpha + 2.3929}{3.3929}|^{.3679} \tag{2.20}$$

where α is the inverse turbulent Prandtl number to be used in equation 2.18. Equation 2.20 is combined with equation 2.19and used to solve for α. Then one over α, the turbulent Prandtl number, can be used in equation 2.18.

FLUENT solves the energy equation iteratively for each element as is discussed in more detail in section 2.3.

Boundary Conditions

FLUENT allows specification of wall boundary conditions by the heat flux through the walls or the wall temperature. Either condition can be specified as a constant or by any function defined by the user. The laminar-flow simulations of one or two passages had user-specified wall temperatures. The functions that defined the temperature profile are

$$T(z) = 525 + 8000z \tag{2.21}$$

$$T(z) = 1150 - 8000z \tag{2.22}$$

for all cases where the fluid was heated or cooled, respectively. The z-direction is in the direction of fluid flow. The temperature profile was uniform peripherally for all tests. When two or more volumes share a common boundary FLUENT creates "shadow" boundaries (discussed in section 2.3.4). Therefore, one wall will transfer heat to all volumes it bounds in order to keep the peripherally uniform wall conditions. These functions were derived in order to best simulate temperatures at the inlet and outlet of actual rotary regenerators [21][23]. A linear function was used as a first approximation to any real temperature profiles because there are no data that suggest a more appropriate form.

In rotary regenerators there is no heat generation in the passages and because of the laminar nature of the flow there is no viscous heating either. Therefore, no source terms were specified in the energy equation for any simulations. All simulation were modeled as incompressible with no work transfer through the walls.

Analytical Calculations

The first law was also used to calculate heat transfer analytically. The form of the first law that was used in the corner-radii simulations includes the flow-work term

$$Q = \dot{m}[(c_p T_m + \frac{P}{\rho})_{out} - (c_p T_m + \frac{P}{\rho})_{in}] \tag{2.23}$$

where Q is the heat transferred into the fluid, T_m is the bulk fluid temperature at the particular passage cross-section. Equation 2.23 can be rearranged to solve for the outlet bulk temperature if the total heat transferred is known

$$T_{out} = \frac{Q}{(\dot{m}c_p)_{out}} + \frac{(c_p T)_{in}}{c_{p,out}} + \frac{1}{c_{p,out}}[(\frac{P}{\rho})_{in} + (\frac{P}{\rho})_{out}] \tag{2.24}$$

2.2.2 Wall Heat Transfer

Laminar Flow

FLUENT solves the energy equation iteratively within the fluid. To calculate the heat transfer through the walls for laminar flow given a time-invariant wall temperature it uses the discrete form of Fourier's conduction law for each cell bordering the wall

$$q'' = k_f \frac{\partial T}{\partial n}|_{wall} \tag{2.25}$$

where the n-direction is normal to the wall and k_f is the fluid thermal conductivity. The temperature gradient is

$$\frac{\partial T}{\partial n} = \frac{T_{wall} - T_{element}}{L_{center}} \tag{2.26}$$

where L_{center} is the distance from the wall to the center of the element next to the wall.

Turbulent Incompressible Flow

When modeling turbulent, incompressible flow in FLUENT with wall functions (see section 2.3.3) the segregated solver (see section 2.3.1) determines the wall heat flux by [16]

$$q'' \equiv \frac{(T_{wall} - T_{element})\rho c_p C_\mu^{1/4} k_P^{1/2}}{T^*} \tag{2.27}$$

where T* is a dimensionless temperature and can be expressed as

$$T^* = \begin{cases} Pr \cdot y^* & y^* < y_T^*, \\ Pr_t[\frac{1}{\kappa}\ln(Ey^*) + P] & y^* > y_T^* \end{cases} \tag{2.28}$$

where Pr_t=0.85 at the wall, E=9.793 is a wall function constant, A=26 is the Van Driest constant, $\kappa = 0.42$ Von Karman constant. The non-dimensional distance y* is

$$y^* \equiv \frac{\rho C_\mu^{1/4} k_P^{1/2} y_P}{\mu} \tag{2.29}$$

and y^*_T is

$$y_T^* \equiv y^* Pr \tag{2.30}$$

and P is computed from

$$P = \frac{\pi/4}{\sin(\pi/4)}(\frac{A}{\kappa})^{1/2}(\frac{Pr}{Pr_t} - 1)(\frac{Pr_t}{Pr})^{1/4} \tag{2.31}$$

Dimensional Analysis

The numerical calculation of heat transfer into the fluid in some of the simulations was checked by using Newton's Law of Cooling

$$q'' = \overline{h}(T_{wall} - T_{element}) \tag{2.32}$$

where $T_{element}$ is the temperature of the fluid element next to the wall at a given position. The definition of the Nusselt number yields

$$\overline{h} = \frac{Nu \cdot k}{D_h} \tag{2.33}$$

$$D_h \equiv \frac{4A_c}{Perimeter} \tag{2.34}$$

where k is the fluid thermal conductivity and Nu is the Nusselt number.

When the corner-radii simulations were analyzed it was useful to define a new hydraulic diameter. This hydraulic diameter is defined as the diameter of a circle with the same cross-sectional area as whatever configuration is being analyzed

$$D_{hyd,new} = \frac{2}{\sqrt{\pi}} A_c \tag{2.35}$$

The Nusselt number is a function of the channel cross section and thermal boundary conditions. The Nusselt numbers for many geometries and boundary conditions are tabulated in [34]. The most common types of boundary conditions are with either constant wall temperature or constant heat flux along the direction of flow. For each of these conditions there are several variations in the peripheral conditions, such as a combination of sides being adiabatic or including radiation heat flux, etc. [34].

This posed a challenge to using equation 2.32 to verify numerical results for certain tests. When the wall temperature profile is specified but not constant then neither the wall heat flux or, by definition, the wall temperature are constant along the direction of flow. Therefore no tabulated Nusselt numbers are applicable to the simulations performed in this study. The arithmetical mean of the Nusselt numbers for constant heat flux and constant wall temperature with uniform peripheral thermal boundary conditions was used as an approximation to determine the average heat-transfer coefficient.

2.2.3 Effectiveness

The information that is useful to the regenerator designer is how different manufacturing inaccuracies or header designs change the effectiveness of the regenerator. The heat-exchanger effectiveness is defined as

$$\epsilon \equiv \frac{heat\ transfered}{maximum\ possible\ heat\ transfer} \tag{2.36}$$

where the subscripts c and h stand for the cold and hot fluids respectively. The simulations performed in this study were only of a single fluid, however. This is because in a rotary regenerator, the hot fluid heats the core material and then the core material later releases the heat to the cold fluid. Therefore, a more appropriate definition of the effectiveness here is

$$\epsilon' = \frac{T_{f,out} - T_{f,in}}{T_{th,h} - T_{f,in}} \tag{2.37}$$

where $T_{th,h}$ is the theoretical temperature at which the hot fluid would be coming into the regenerator and the subscript f corresponds to the fluid being heated.

For the case of the hot fluid being modeled the effectiveness becomes

$$\epsilon' = \frac{T_{f,out} - T_{f,in}}{T_{th,c} - T_{f,in}} \tag{2.38}$$

2.3 Numerical Flow

FLUENT 5.4 uses a finite-volume method with multiple choices for solvers and discretization schemes. The user can also specify various turbulence models and parameters as appropriate.

2.3.1 Solver

The segregated (uncoupled) solver was used for all simulations. This solver iterates each equation separately as described in [16]

- Fluid properties are updated, based on the current solution. (If the calculation has just begun, the fluid properties will be updated based on the initialized solution.)

- The u, v, and w momentum equations are each solved in turn using current values for pressure and face mass fluxes, in order to update the velocity field.

- Since the velocities obtained in Step 1 may not satisfy the continuity equation locally, a "Poisson-type" equation for the pressure correction is derived from the continuity equation and the linearized momentum equations. This pressure correction equation is then solved to obtain the necessary corrections to the pressure and velocity fields and the face mass fluxes such that continuity is satisfied.

- Where appropriate, equations for scalars such as turbulence, energy, species, and radiation are solved using the previously updated values of the other variables.
- When interphase coupling is to be included, the source terms in the appropriate continuous-phase equations may be updated with a discrete-phase trajectory calculation.
- A check for convergence of the equation set is made.

This process is repeated until the desired level of convergence is obtained.

Linearization of Discretized Equations

The governing equations must be discretized and linearized before they can be solved. FLUENT uses a finite-volume approach to discretization, so that the governing equations are solved for each volume element. The segregated solver in FLUENT uses, by default, an implicit linearization scheme that solves for an entire variable field simultaneously. It then uses an algebraic multi-grid method to solve for the dependent variable (i.e. u,v,w velocity, etc.) in each cell.

Discretization of the governing equations can be demonstrated, for a time-independent case as in this study, by taking the integral form of conservation for an arbitrary scalar quantity ϕ and volume V

$$\oint \rho\phi\mathbf{v} \cdot dA = \oint \Gamma_\phi \nabla_\phi \cdot dA + \int_V S_\phi dV \tag{2.39}$$

where Γ_ϕ is the diffusion coefficient of ϕ and S_ϕ is the source term per unit volume of ϕ. Equation 2.39 can be rewritten as

$$\sum_f^{n_{faces}} \mathbf{v}_f \phi_f A_f = \sum_f^{n_{faces}} \Gamma_\phi (\nabla\phi)_n A_f + S_\phi V \tag{2.40}$$

This equation must next be linearized. FLUENT creates

$$a_P \phi = \sum_{nc} a_{nc}\phi_{nc} + b \tag{2.41}$$

for each cell where nc stands for neighboring cell and a_P and b are linearized coefficients. A first-order differencing scheme calculates ϕ_f as the value it has in the cell where the scalar entered from. A second-order scheme calculates ϕ_f by

$$\phi_f = \phi + \nabla\phi \cdot \Delta s \tag{2.42}$$

where $\nabla\phi$ is computed using the discrete form of the divergence theorem

$$\nabla\phi = \frac{1}{V}\sum_{f}^{n_{faces}} \tilde{\phi}_f A \tag{2.43}$$

where $\tilde{\phi}_f$ is the average of the two cells adjacent to the face.

For example, when this method is applied to the time-independent mass and x-momentum equations they become

$$\sum_{f}^{n_{faces}} \rho v_n A_f = 0 \tag{2.44}$$

and

$$a_P u = \sum_{nc} a_{nc} u_{nc} + \sum P_f \cdot \imath A + S \tag{2.45}$$

respectively. The linearized set of equations of this form is what is solved using, in this case, the algebraic multi-grid (AMG) solver.

Differencing Scheme

In equation 2.39 the values of ϕ are those at the cell boundaries. FLUENT, however, stores the values of variables at cell centers. The values at cell interfaces must then be interpolated. The default methods in FLUENT were used in this study for each variable [16].

The Standard pressure-interpolation scheme in FLUENT uses the momentum equation coefficients at the cell faces to interpolate the pressure gradient. This method provides inaccurate answers in situations where body forces are important such as swirling flow or where there is flow curvature. The result is inaccurate pressure values and possibly velocity vectors that are directed into or out of walls. The best method

Table 2.1: Differencing Schemes for Flow Field Variables

Variable	Differencing Scheme
Pressure	Standard
Momentum	First & Second-Order Upwind
Pressure-Velocity coupling	SIMPLE
Energy	First Order Upwind
Turbulent Kinetic Energy	First & Second-Order Upwind
Turbulent Dissipation Rate	First & Second-Order Upwind

for preventing these situations is to create a fine-enough mesh that there are not large pressure gradients between adjacent cells.

The Semi-Implicit Method for Pressure Linked Equations (SIMPLE) scheme is described in [31]. It uses a pressure-correction equation to help the momentum equations converge to satisfy continuity. It is less likely than SIMPLEC to have convergence problems if convergence is being limited by the pressure-velocity coupling. See [16][31] for more details.

The First Order Upwind Differencing scheme is used as the default scheme for the energy, turbulent-kinetic-energy and the turbulent-dissipation-rate equations. This scheme sets the value of ϕ at any surface equal to the value at the center of the cell on the "upwind" side. The "upwind" side is the side from which fluid flows into the element. The idea behind this is that any fluid flowing into a cell would have the properties of the cell from which it came, assuming that the old cell had a uniform distribution of ϕ. See [31][4] for details.

Second-Order Upwind Differencing is generally more appropriate than First Order when the flow is either not perpendicular to the cell faces, such as when using a triangular or tetrahedral mesh. Generally a Second Order Upwind scheme does not converge as well as First Order and so takes more computational expense.

Table 2.2: Typical Under-Relaxation Factors in Turbulence Models

Equation	Under-Relaxation Factor
Pressure	0.3
Momentum	0.7
Energy	1
Turbulent Kinetic Energy	0.9
Turbulent Dissipation Rate	0.9
Viscosity	1
Density	1

Under-Relaxation Factors

When divergence becomes a problem, under-relaxation factors can be applied to the changes in scalar quantities ϕ to limit the change from one iteration to the next. The value of a given quantity is established by

$$\phi_{current} = \phi_{old} + \alpha\Delta\phi \tag{2.46}$$

where α is the under-relaxation factor and can vary from 0 to 1 and $\Delta\phi$ is the change in ϕ computed on the given iteration. When the flow is "well behaved" under-relaxation factors tend to affect only the speed of convergence, but if the mesh is too coarse or when using turbulence models they can help prevent divergence as well. For most tests the under-relaxation factors used are presented in table 2.3.1.

When laminar flow was simulated the turbulent equations were not applicable and therefore no under-relaxation factor was specified.

2.3.2 Turbulence Modeling

The models of portions of the inlet header and regenerator have very turbulent flow in the header region. There were areas of strong curvature, separation and recirculation to be modeled. Turbulence models do not always provide accurate results under theses conditions. Therefore three variations of the k-ϵ turbulence model were used and the results compared with literature to ascertain which model is most appropriate under these circumstances.

Standard k-ϵ Model

The k-ϵ model was introduced by Launder and Spalding (1972) [6]. It consists of two equations in addition to the Navier-Stokes equations, one for the turbulent kinetic energy (k) and one for the dissipation rate of the turbulent kinetic energy ϵ. The models are defined in [5]. The definitions of k and ϵ are

$$k \equiv \frac{1}{2}\langle |u'|^2 \rangle \tag{2.47}$$

and

$$\epsilon \equiv \frac{\nu}{2}\langle |\nabla u' + \nabla u'^T|^2 \rangle \tag{2.48}$$

The Reynolds-averaged Navier-Stokes equations can be written

$$\frac{\partial U}{\partial t} + U\nabla U + \nabla P - \nu\Delta U - \nabla R = 0 \tag{2.49}$$

where U is the mean flow, P is the mean pressure and $R \equiv R(k, \epsilon, \nabla U + \nabla U^T)$ is the Reynolds stress tensor. This assumes incompressibility

$$\nabla \cdot U = 0 \tag{2.50}$$

The Reynolds tensor can be written as

$$R = -\frac{2}{3}kI + (\nu + c_\mu \frac{k^2}{\epsilon})(\nabla U + \nabla U^T) \tag{2.51}$$

This can be substituted into the Reynolds-averaged equation and then the final three equations for the k-ϵ model are

$$D_t k - \nabla \cdot (\nu_T \nabla k) - c_\mu \frac{k^2}{\epsilon} E + \epsilon = 0 \tag{2.52}$$

$$D_t \epsilon - \nabla \cdot (\frac{c_\epsilon}{c_\mu} \nu_T \nabla \epsilon) - c_1 k E + c_2 \frac{\epsilon^2}{k} = 0 \tag{2.53}$$

$$D_t U + \nabla P^* - \nabla \cdot [(\nu + \nu_T)(\nabla U + \nabla U^T)] = 0 \tag{2.54}$$

Realizable k-ϵ Model

In certain flow situations, when the strain is large, the Reynolds stress tensor as defined in equation 2.51 can become negative. To quantify when this happens we define

$$\nu_T \equiv c_\mu \frac{k^2}{\epsilon} \tag{2.55}$$

When this is substituted into equation 2.51 and one of the component directions is looked at, say the x-direction, then the Reynolds-stress tensor becomes negative when

$$\frac{k}{\epsilon}\frac{\partial U}{\partial x} > \frac{1}{3C_\mu} \simeq 3.7 \tag{2.56}$$

The realizable k-ϵ model corrects for this as describe in [16] by allowing C_μ to be a function of the mean flow and k

$$C_\mu = \frac{1}{A_0 + A_s \frac{U^* k}{\epsilon}} \tag{2.57}$$

where

$$U^* \equiv \sqrt{S_{ij}S_{ij} + \tilde{\Omega}_{ij}\tilde{\Omega}_{ij}} \tag{2.58}$$

$$\tilde{\Omega}_{ij} = \bar{\Omega}_{ij} - 3\epsilon_{ijk}\omega_k \tag{2.59}$$

Omega is the angular velocity and $\bar{\Omega}_{ij}$ is the mean rate-of-rotation tensor from the rotating reference frame rotating at angular velocity ω. The constants are $A_0 = 4.04$ and $A_s = \sqrt{6}\cos\phi$. The variable ϕ is defined by

$$\phi \equiv \frac{1}{3}\arccos(\frac{\sqrt{6}S_{ij}S_{jk}S_{ki}}{\sqrt{S_{ij}S_{ij}}}) \tag{2.60}$$

where

$$S_{ij} \equiv \frac{1}{2}(\frac{\partial u_j}{\partial x_i} + \frac{\partial u_i}{\partial x_j}) \tag{2.61}$$

The correction for the negative Reynolds stress means that the realizable k-ϵ model is better suited to flow with high strain rates than the standard k-ϵ model.

RNG k-ϵ Model

The RNG (Renormalization Group Theory) k-ϵ model was introduced by Yakhot and Orszag in 1986 [43]. It is similar in form to the standard k-ϵ model. The turbulent kinetic energy and dissipation rates are of the form

$$\rho\frac{Dk}{Dt} = \frac{\partial}{\partial x_i}(\alpha_k \mu_{eff}\frac{\partial k}{\partial x_i}) + G_k + G_b - \rho\epsilon - Y_M \tag{2.62}$$

$$\rho\frac{D\epsilon}{Dt} = \frac{\partial}{\partial x_i}(\alpha_\epsilon \mu_{eff}\frac{\partial \epsilon}{\partial x_i}) + C_{1\epsilon}\frac{\epsilon}{k}(G_k + C_{3\epsilon}G_b) - C_{2\epsilon}\rho\frac{\epsilon^2}{k} - R \tag{2.63}$$

where $C_{1\epsilon}, C_{2\epsilon}$ and $C_{3\epsilon}$ are constants established by Yakhot and Orszag and also listed in [9]. The default values in FLUENT are from the updated RNG model by Yakhot and Smith [42].

The parameters G_k, G_b and Y_M represent the turbulent-kinetic-energy generation from mean velocity gradients and buoyancy effects, when modeling compressible and turbulent flow, to the overall dissipation rate as described in [16]. In the simulations performed here the buoyancy and compressibility effects were negligible. Therefore G_k is the only important source term and is defined as

$$G_k \equiv -\rho\overline{u_i'u_j'}\frac{\partial u_j}{\partial x_i} \tag{2.64}$$

To evaluate G_k in a way consistent with the Boussinesq hypothesis use the form

$$G_k = 2\mu_T S_{ij}S_{ij} \tag{2.65}$$

where

$$S_{ij} = \frac{1}{2}(\frac{\partial u_i}{\partial x_j} + \frac{\partial u_j}{\partial x_i}) \tag{2.66}$$

Comparisons among the standard, realizable and RNG k-ϵ models have shown that there can be substantial differences in results between the three. In the classic case of a backward-facing step the improved RNG k-ϵ model used here has been shown to be far more accurate in predicting reattachment than the standard k-ϵ and even the original RNG model [9]. The RNG model is also more accurate in modeling high strain and streamline curvature, such as recirculating flows, than the standard k-ϵ model [16][18]. The realizable k-ϵ model has been shown to be more accurate than the standard k-ϵ model in predicting spreading in jet flow and when shear in the fluid is very large [39].

The advantages of the RNG and realizable k-ϵ models over the standard model do not preclude its use, however. Certain classes of flows have been shown to be more accurately predicted by the standard model, such as confined co-flow jets [18]. It is therefore worthwhile to give at least a cursory examination of all three models.

2.3.3 Wall Functions

Creating a mesh that is fine enough along the walls to resolve the boundary-layer properties requires a great deal of computational power and time. To circumvent this problem wall functions can be applied that impose law-of-the-wall profiles for all variables of interest within the necessary elements close to the walls. Wall functions typically separate the cell next to the wall into a viscous sublayer and a turbulent sublayer. This ensures that the boundary-layer effects on the main flow may be accounted for without extra computational time and complexity of resolving the boundary layer.

There are two options for wall-function types in FLUENT:

- standard
- non-equilibrium

The non-equilibrium wall functions are more capable of accounting for complex flows involving severe pressure gradients, separation and reattachment or rapidly changing flows. The recirculation and separation encountered in most of the turbulent simulations required accuracy in modeling these effects so the non-equilibrium functions were applied to all turbulent cases.

The law-of-the-wall applies in the turbulent region of the boundary layer, sometimes called the log-layer, and is typically expressed as

$$\frac{U}{u_T} \equiv \frac{1}{\kappa} \ln(E \frac{u_T y}{\nu}) \tag{2.67}$$

where

$$u_T \equiv \sqrt{\frac{\tau_w}{\rho}} \tag{2.68}$$

and E=9.8 and κ is the von Karman constant with a typical value of 0.42. This is true when standard wall functions are applied. The non-equilibrium wall functions redefine the dimensionless velocity to account for pressure gradients [37]

$$\frac{\tilde{U} C_\mu^{1/4} k^{1/2}}{\tau_w/\rho} = \frac{1}{\kappa}\ln(E\frac{\rho C_\mu^{1/4} k^{1/2} y}{\mu}) \tag{2.69}$$

where

$$\tilde{U} = U - \frac{1}{2}\frac{dP}{dx}[\frac{y_v}{\rho\kappa^* k^{1/2}}\ln(\frac{y}{y_v}) + \frac{y-y_v}{\rho\kappa^* k^{1/2}} + \frac{y_v^2}{\mu}] \tag{2.70}$$

where y_v is the thickness of the viscous sublayer defined as

$$y_v \equiv \frac{\mu y_v^*}{\rho C_\mu^{1/4} k_P^{1/2}} \tag{2.71}$$

where y_v^*=11.225 and k is the turbulent kinetic energy. When this type of wall function is applied certain assumptions are made

$$\tau_t = \begin{cases} 0 & y < y_v \\ \tau_w & y > y_v \end{cases} \tag{2.72}$$

$$k = \begin{cases} (\frac{y}{y_v})^2 k_P & y < y_v \\ k_P & y > y_v \end{cases} \tag{2.73}$$

$$\epsilon = \begin{cases} \frac{2\nu k}{y^2} & y < y_v \\ \frac{k^{3/2} C_\mu^{3/4}}{\kappa y} & y > y_v \end{cases} \tag{2.74}$$

This profile is identical to that from the standard wall function approach if the pressure gradient is zero, so there are no adverse effects of this approach even where a standard function would suffice. The profile described above can be used to obtain the cell-averaged production, $\bar{G}_k$ and dissipation rate $\bar{\epsilon}$ of k by integration

$$\bar{G}_k \equiv \frac{1}{y_n}\int_0^{y_n} \tau_t \frac{\partial U}{\partial y} dy = \frac{1}{\kappa y_n}\frac{\tau_w^2}{\rho C_\mu^{1/4} k_P^{1/2}}\ln(\frac{y_n}{y_v}) \tag{2.75}$$

$$\bar{\epsilon} \equiv \frac{1}{y_n}\int_0^{y_n} \epsilon dy = \frac{1}{y_n}[\frac{2\nu}{y_v} + \frac{k_P^{1/2}}{\kappa C_\mu^{-3/4}}\ln(\frac{y_n}{y_v})]k_P \tag{2.76}$$

These can then be substituted into equations 2.52 and 2.53 to solve for the k and ϵ values near the wall.

2.3.4 Boundary Conditions

There are many types of flow boundaries that can be specified in FLUENT: each of these has many parameters that can be specified by the user. Only a subset of these boundaries was necessary in this study to simulate actual conditions as closely as possible

- Velocity Inlet
- Pressure Outlet
- Wall
- Shadow
- Symmetry

In all of the tests performed in this study, the flow entered the model in one opening. Velocity inlets are ideal for flow entering a domain at one place. The user can specify the direction and magnitude of the flow into the model, the inlet temperature of the fluid and the value of turbulence quantities (if applicable). All of these can be specified as functions of time or position across the inlet face. Specifying the turbulence quantities can be difficult because of the unknown value of the velocity fluctuations that they are defined by in equations 2.47 and 2.48. FLUENT allows the user to estimate the values of k and ϵ by specifying the turbulence intensity, I, and length scale, l

$$I = \frac{u'}{\bar{u}} \cong .16 Re_{D_h}^{\frac{-1}{8}} \tag{2.77}$$

$$l = .07 L_{ch} \tag{2.78}$$

where L_{ch} is the characteristic length scale of the entrance, most likely the D_h. The turbulent kinetic energy, k, and the turbulent energy dissipation rate, ϵ, can be derived from these definitions by

$$k = \frac{3}{2}(\bar{u}I)^2 \tag{2.79}$$

$$\epsilon = C_\mu^{3/4}\frac{k^{3/2}}{l} \tag{2.80}$$

The pressure-outlet boundary condition allows the user to specify the gauge pressure and back-flow fluid temperature and turbulence quantities (if applicable). They can be user-defined functions of time or position across the outlet face. Pressure boundaries are useful in speeding up convergence when there is back-flow into the fluid domain.

Wall boundary conditions are used to define an interface between solid and fluid regions. The no-slip condition is applied by default (although it can be altered) and was used in all simulations. Adiabatic conditions can be specified as well as heat flux or temperature conditions (see section 2.2.1) that can be defined as functions of temperature or position by the user.

Shadow boundaries are automatically employed by FLUENT when one wall serves as a boundary for two or more fluid regions. The shadow boundaries occupy the same space as the original boundary but the specified conditions hold for one fluid region (per shadow) and the conditions on the original boundary apply for one region as well.

Symmetry boundary conditions are used when only a part of a fluid region is being modeled. Symmetry conditions set all gradients equal to zero on the boundary so that all variables have equal values on both sides. This is a good approximation to having nothing to interfere with the flow; however, in cases where there would normally be gradients across the boundary, such as three-dimensional turbulence, they might not be an accurate representation of reality.

Chapter 3

Numerical Models

There were three basic model designs that were used to perform most of the simulations in this study. There are, however, many variations of these designs that were used to ascertain the effects of different non-uniformities. In each set of basic models careful attention was paid to the mesh to assure that all relevant phenomena were captured and modeled as accurately as possible given the solving techniques employed.

3.1 Two-Passage Models

Many of the simulations were of two passages of a theoretical regenerator. This means that all of the non-uniformities were essentially modeled as occurring in half the passages in the regenerator. One half of the passages became larger; the other half became smaller as a result of the non-uniformity. Modeling more passages requires much more computational expense and the only gain would be to vary the percentage of channels with a given variation; it was decided that this was not justifiable given the limited computational resources available. There were four types of geometries with two passages and non-uniformities .

- With an inlet plenum chamber and center wall offset
- Fully developed flow with the center wall offset

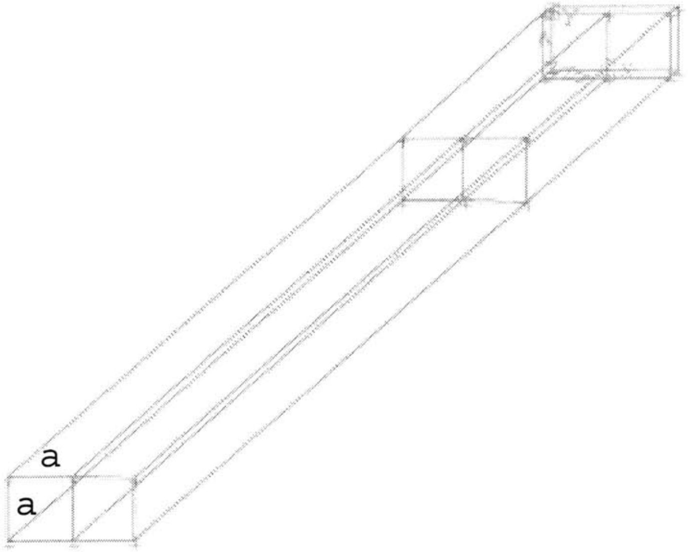

Figure 3-1: Profile of Aspect Ratio=1 Test, a=0.0005 m Is Passage Width and Height

- The passage width varying along the flow direction
- A bend in the center wall

The first simulations were of two passages that had a plenum chamber attached to the inlets. This was to ensure that the total mass flow rate through the passages could be controlled without specifying what percentage of the flow would go through each chamber. Three aspect ratios were modeled: 1, 0.5, 0.25. The cross-sections of the geometries are presented in figures 3-2, 3-3 and 3-4. A profile of the aspect ratio 1 test with an inlet plenum chamber is in 3-1. The passage dimensions for the case of identical passages were based on actual rotary-regenerator passages [20][21][28][7]. The nominal (referring to the case of uniform passages) hydraulic diameters for the three aspect ratios are listed in Table 3.1.

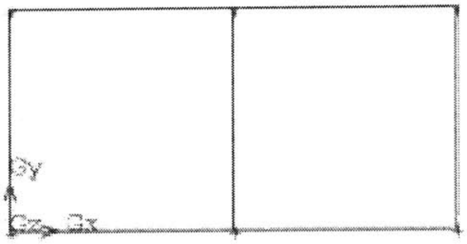

Figure 3-2: End View of Aspect Ratio=1 Configuration

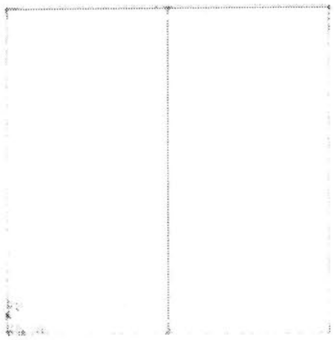

Figure 3-3: End View of Aspect Ratio=0.5 Configuration

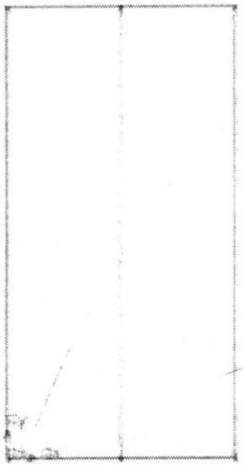

Figure 3-4: End View of Aspect Ratio=0.25 Configuration

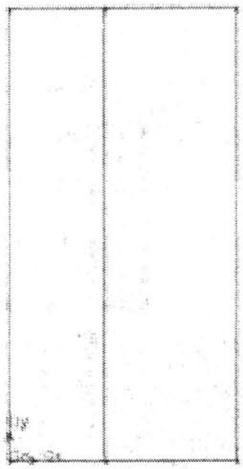

Figure 3-5: End View of Aspect Ratio=0.25 Configuration With Maximum Channel Deviation

Table 3.1: Hydraulic Diameters for Different Aspect Ratios of Two-Passage Center Wall Offset Models

Aspect Ratio	Hydraulic Diameter
1	5eE-4 m
0.5	4.71E-4 m
0.25	4E-4 m

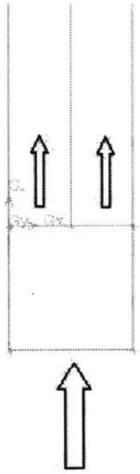

Figure 3-6: Inlet Section of Aspect Ratio 1 Test

The inlet plenum chamber was 0.001 m long. This is long enough (approximately 2 hydraulic diameters, see Figure 3-6) so that flow-curvature effects do not extend to the inlet of the chamber, but it does not contribute significantly to the overall number of mesh elements. The length of the passages was 0.075 m. This is approximately 160 hydraulic diameters so the exiting flow is hydrodynamically fully developed.

For each of these aspect ratios the center wall dividing the two channels was offset up to approximately 20% of the nominal passage width. The simulations were performed at a constant temperature of 300° K. The fully developed velocity profiles were recorded so that they could be reused in simulations of fully developed flow .

3.1.1 Fully Developed Tests

The outlet velocity profiles from the above tests were used as profiles for the inlets of the fully developed tests. The inlet plenum chamber was eliminated but geometries were otherwise identical. Three sets of thermal boundary conditions were simulated with these geometries

- Adiabatic Walls
- Heated Walls
- Cooled Walls

The adiabatic-walls tests were used to compare pressure drop and frictional characteristics with literature to establish the modeling techniques for these simulations.

The heated and cooled walls had wall-temperature profiles as specified by equations 2.21 and 2.22. Both heating and cooling were simulated to see if the change in regenerator effectiveness from non-uniformities was a function of whether the air (cold) side or gas (hot) side of the regenerator was being modeled. The inlet fluid temperatures for all cases using equation 2.21 was 525° K and for all cases using equation 2.22 was 1125° K.

3.1.2 Variable-Property Effects

The fully developed heated tests mentioned previously were selected to determine how variable properties affect the overall heat-exchanger effectiveness for a given geometry. The standard method of determining property values such as density, viscosity, etc. is to take the mean value within the fluid. This is usually done by taking the average inlet and outlet temperatures, finding the mean and specifying all properties constant throughout the fluid at the values corresponding to the mean temperature. There has been some work attempting to quantify how much this approach (called the single-element method) changes the outlet temperature and pressure drop compared to having properties values set at the local temperature of an element [41]. The results suggested little difference between the single-element method and a multiple-element method (where the flow is split into several sections and each is evaluated at a mean temperature). The effect on the heat transfer into the passage was not considered explicitly.

Variable properties were specified by a polynomial curve-fit from data in [17]

$$C_p(T) = 881.68 + .32424T - 6.6287 \cdot 10^{-5}T^2 \tag{3.1}$$

$$k(T) = -1.8422 \cdot 10^{-2} + 1.7776 \cdot 10^{-4}T - 1.4687 \cdot 10^{-7}T^2 + 5.3897 \cdot 10^{-11}T^3 \tag{3.2}$$

$$\mu(T) = -1.2678 \cdot 10^{-6} + 7.6243 \cdot 10^{-8}T - 4.7071 \cdot 10^{-11}T^2 + 1.4417 \cdot 10^{-14}T^3 \tag{3.3}$$

The density, ρ, was specified as conforming to that for an incompressible ideal gas as

$$\rho(T) = \frac{P_{atm}}{RT} \tag{3.4}$$

This closely approximates an ideal gas because the maximum pressure difference between the inside and the atmosphere is small compared to atmospheric pressure (see Appendix A). All tests were performed using the variable-property method except the heated fully developed tests that were used to compare with the variable property effects.

3.1.3 Wall Deviation Along Flow Direction

The next set of tests are based on the geometry of Figure 3-2 with an inlet plenum chamber and two square passages, for the uniform case. Figure 3-7 shows the case with a maximum deviation. The center wall is pivoted from the passage inlets. This sort of deviation could arise with warping of the matrix while curing. The wall temperatures in this series of tests was for heating of the fluid (equation 2.21). Seven tests were performed with different amount of channel deviation. The maximum normalized deviation (end width of channel/starting width of channel) that was simulated was 0.7 as shown in figure 3-7.

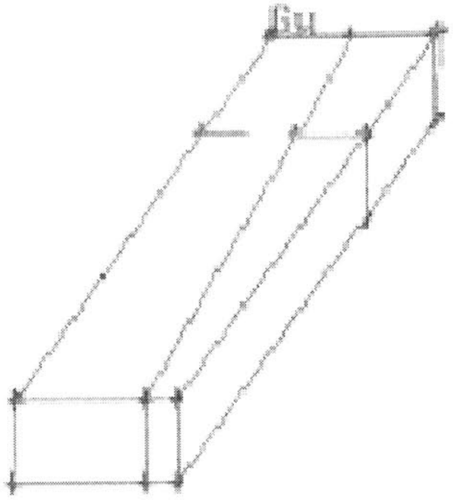

Figure 3-7: Case of Maximum Wall Deviation Along Flow Direction

3.1.4 Wall-Curvature Deviation

It is possible during the curing process for the walls to bend. This could happen if the matrix composition is not completely uniform or if there are slightly different rates of drying across the matrix. This type of non-uniformity was modeled as a bow in the center wall as shown in figure 3-8. Once again the uniform case is the same geometry and fluid properties as for the 1:1 aspect ratio case shown in figure 3-1. Six simulations were performed; the maximum channel deviation (width halfway down channel/starting width of channel) modeled was 0.6.

3.2 Corner-Radii Effects

In reality, no passage is truly square or rectangular. There is always some rounding of the edges. Extruding ceramic regenerator matrices can lead to some corner roundoff. This defect can have substantial effects on the mass flow rate and velocity profile through the individual tubes, thereby reducing the amount of heat transferred in the regenerator.

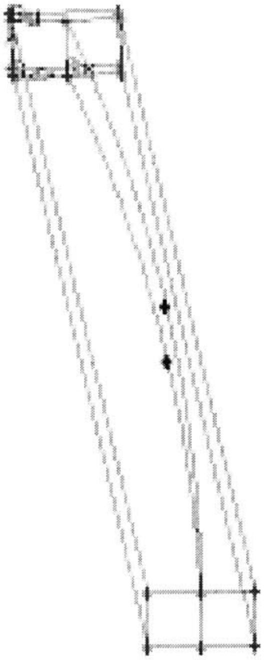

Figure 3-8: Profile of Wavy-Deviation Test With Maximum Deviation

There is no literature on how large of a corner-radius defect can be expected per se. The rough tolerances that can be achieved through extrusion in general vary substantially [22][12]. There is no data that this author is aware of that details the tolerances achieved through wrapping of regenerators. Therefore the entire range of possibilities was modeled. The radius in each of the corners ranged from $1.25 \cdot 10^{-5}$ m to $2.4 \cdot 10^{-4}$ m. This effectively gives a square and a circular cross section respectively. A single passage was modeled in each simulation because a defect in one passage doesn't necessarily induce a defect in a neighboring passage. The mass flow rate per unit cross-sectional area was kept constant at 6.793 kg/m^2s in all tests. This was to simulate an actual regenerator face where differences in passage geometry don't have much effect on the flow impinging upon the regenerator face. The range of passage cross-sections is shown in figure 3-9. The distance from one side to the other on these geometries is $5 \cdot 10^{-4}$ m so that if there were no corner radii they would be the same as a passage from figure 3-1. The length of these passages was

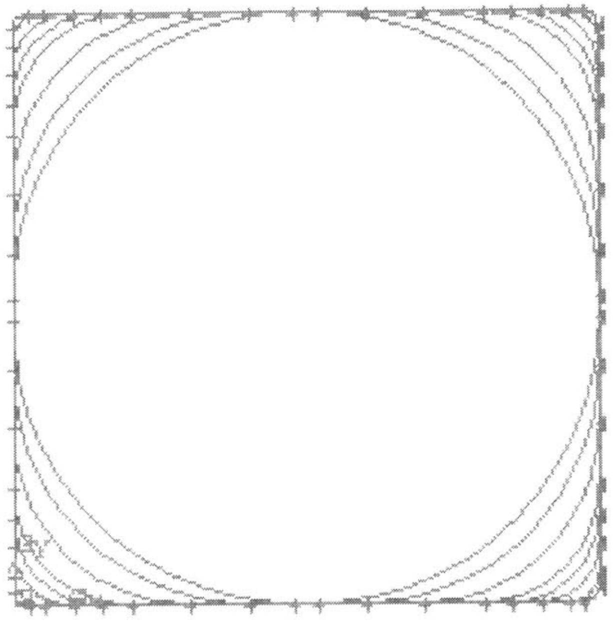

Figure 3-9: Cross-sectional View of Corner Radii Tests

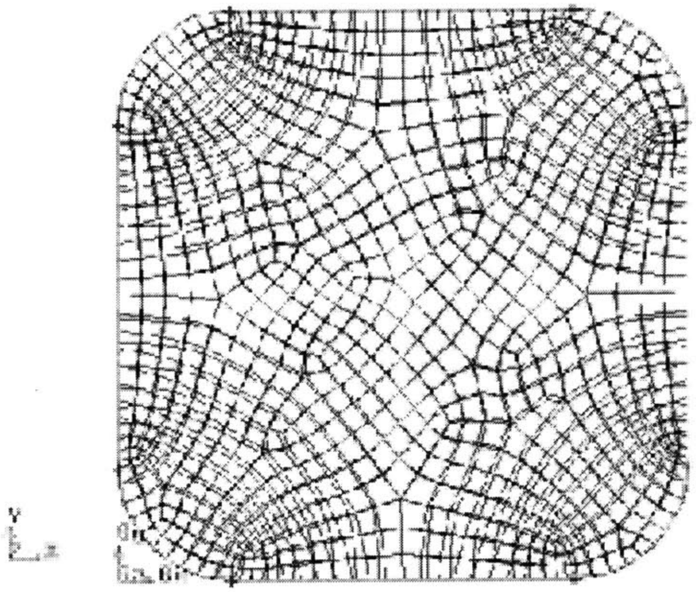

Figure 3-10: Cross-sectional View of Corner Radii Test and Mesh With .0001 m Corner Radii

also the same as previous models: 0.075 m. The exception to this is when performing mesh-independence simulations the passage length was reduced to 0.02 m in order to create a finer mesh. The wall temperature for all cases with corner radii was specified according to equation 2.21.

An unstructured meshing scheme was applied for the corner-radii simulations in order to obtain a more accurate resolution of the near-wall effects of the corners. A sample of the mesh is shown in figure 3-10.

The mesh is much finer around the edges than in the center and the elements become even smaller the closer they are to the corners. This is much easier to create with an unstructured mesh than a structured mesh in this geometry. The variable mesh density throughout the cross-section also allows for more efficient computation by placing more elements where gradients are highest.

3.3 Inlet-Header Models

Another goal of this study has been to provide a more clear understanding of how inlet header designs affect the flow distribution into the regenerator. This can assist in designing headers that provide a more even flow distribution and optimize pressure drop through the regenerator. There are three basic sets of geometries that involved the inlet-header designs. The first was to measure the effect of incident flow on a passage; the second was to verify the porous-medium model; the third was modeling a section of the regenerator and inlet header to measure flow distribution and pressure drop in the header.

3.3.1 Incident Flow

Simple square passages 0.5 mm by 0.5 mm by 20 mm were modeled with heated-wall temperature boundary conditions as specified by equation 2.21 were applied for varying degrees of impinging flow. Figure 3-11 shows the passage inlet and how the angle of incidence is defined. The cross-section and the mesh used were the same as for one passage of the square-two-passage geometry in figure 3-2.

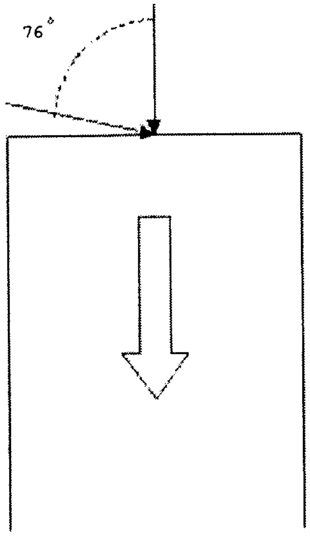

Figure 3-11: Inlet for Incident Flow Tests

These simulations were performed to be able to see the effects of flow incidence on a given channel rather than just in aggregate over the entire regenerator. The inlet temperature for all tests was 525° K. The mass flow was constant in magnitude, but not in direction, at 1.681 kg/s. Only a fraction of this actually flowed through the passage. In an actual regenerator inlet face the angle of incidence of the flow determines the percentage of the flow that goes into the tube and the percentage that flows by the inlet face and enters another passage. This situation was modeled not to determine how or when the incidence occurs, but what happens to the heat transfer and effectiveness assuming that there is incidence. The situations where incidence occurs are modeled in the later simulations.

There were eleven simulations with incidence angles varying from 0° to 76°. In all cases the wall temperature was specified according to equation 2.21, and therefore heated the fluid.

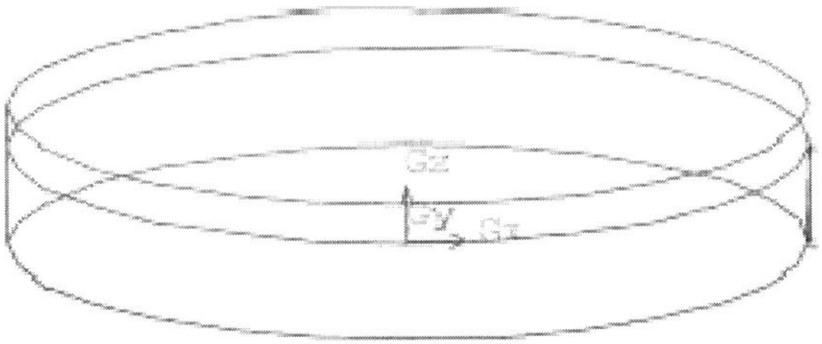

Figure 3-12: Geometry for Validating Porous-Media Model

3.3.2 Porous-Medium Tests

The specification of a porous-medium zone is described in section 2.1.3. Simulations of a tube of diameter 0.6 m and a length of 0.105 m were performed to verify that the method of specifying the porous zone would yield the desired pressure drop. A profile of the geometry is shown in figure 3-12. The inlet flow was specified at 10 m/s uniformly over the inlet section and the porous zone was defined as the lower 0.075 m.

Simulations were performed at temperatures from 550° K to 1150° K in 100° K increments. All simulations were performed at constant temperature; no heat was added through the walls or through the porous medium. This is because the temperature of the porous medium could not be specified as different than the fluid; only a heat flux into the fluid from the medium could be specified. The heat flux is the unknown in these situations and therefore would be useless to specify. The variation in temperature from test to test was to determine how the different properties affect the inertial and viscous parameters that were specified to give the desired pressure drop.

The thermo-physical properties of the porous zone were defined to simulate that of cordierite [10]. Cordierite is part of the magnesium-alumino-silicates family of min-

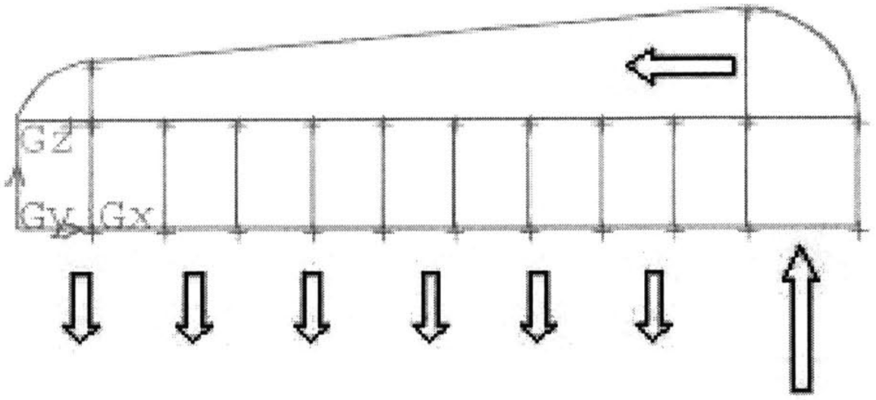

Figure 3-13: Profile of Inlet Header and Regenerator Model with Flow Direction Indicated

erals and is a common material used to produce ceramic regenerators. The porosity of the porous medium was set at 0.7 for all cases to most closely simulate actual regenerators.

3.3.3 Inlet-Header and Regenerator Tests

The actual inlet headers and regenerators modeled were only a section of the entire regenerator. This limitation is due to the computational expense and difficulty in modeling the three-dimensional curvature of an entire inlet header and regenerator.

Several variations on the header shape were tried. The first is shown in figure 3-13. The air enters from the bottom-right and is turned 90° and is then turned again and forced through the regenerator core.

The inlet velocity is 70 m/s; this was set to achieve a reasonable 10.5 m/s velocity through the regenerator. The flow is turbulent in the header. Either the realizable or the RNG k-/epsilon models with non-equilibrium wall functions were applied as described in sections 2.3.2 and 2.3.3. All tests were performed with variable properties and at a temperature of 525° K. No heat addition was included for the same reasons

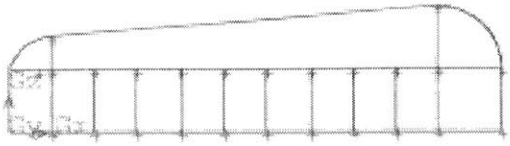

Figure 3-14: Profile of Long Inlet Header

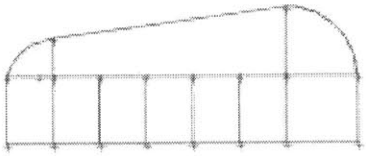

Figure 3-15: Profile of Short Inlet Header

as mentioned in the previous section.

The dimensions of the model in figure 3-13 are 0.575 m wide in the x-direction with the regenerator being the left 0.5 m of that. The inlet section on the right is 0.075 m wide and the turn is a quarter circle, so the height of the header above the regenerator is 0.075 m where the fluid enters the header itself. The left side of the header is 0.0375 m tall, with the slope being linear between there and the inlet turn. The depth of the model into the page varied between tests, smaller depths required less computing power, but the standard was 0.1 m. The regenerator in figure 3-13 appears to be divided into 10 sections; those walls effectively disappear when importing the geometry into FLUENT from the pre-processor and should be ignored.

There is no universal shape or aspect ratio for inlet headers. Therefore the aspect ratio for this shape was reduced to see if that has any effect on the velocity and pressure distributions. Figure 3-13 is reproduced as figure 3-14 along with the smallest aspect-ratio model in figure 3-15. There were two intermediate-aspect-ratio configurations that were also studied.

The shortest model, figure 3-15, has a regenerator section of length 0.3 m; the next two models extend that length by 0.065 m each and the longest model, figure 3-14 has a 0.5 m long regenerator. In all four of these models, the inlet section and the inlet turn are identical. In each case the inlet velocity is proportional to the regenerator size, thereby retaining the 10.5 m/s velocity through the regenerator.

Turning Vanes

The 180° turn that the fluid must undergo when passing through the regenerator contributes to the velocity maldistribution. The effect was quantified by taking the

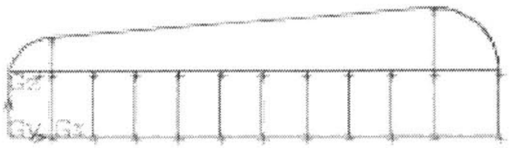

Figure 3-16: Profile of 90° Inlet, Identical to Figure 3-14

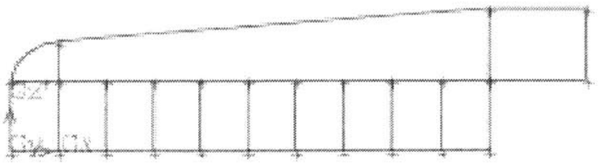

Figure 3-17: Profile of 0° Inlet

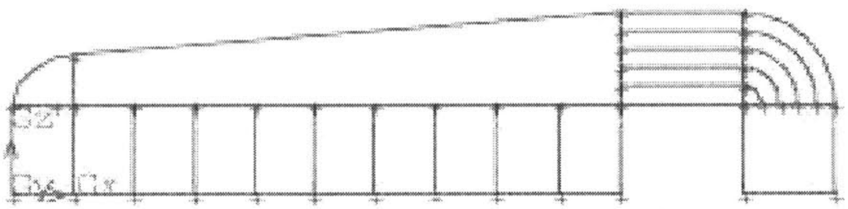

Figure 3-18: Geometry with Turning Vanes

geometry in figure 3-14 and systematically altering the angle at which the fluid enters the model with respect to the regenerator. The two extreme cases are figures 3-16 and 3-17.

There are five other configurations having inlets at approximately 15° intervals between 0° and 90°.

The extreme case shown in figure 3-17 was compared to a geometry that used turning vanes and a straight section for flow settling instead of changing the angle of the inlet pipe. This geometry is displayed in figure 3-18.

There are other configurationss that also have variations that use turning vanes such as figures 3-21 and 3-20. In addition to these turning-vane tests, a test with turning vanes but no settling length that is otherwise identical to figure 3-18 was performed to see if the settling length produced a more uniform flow distribution into

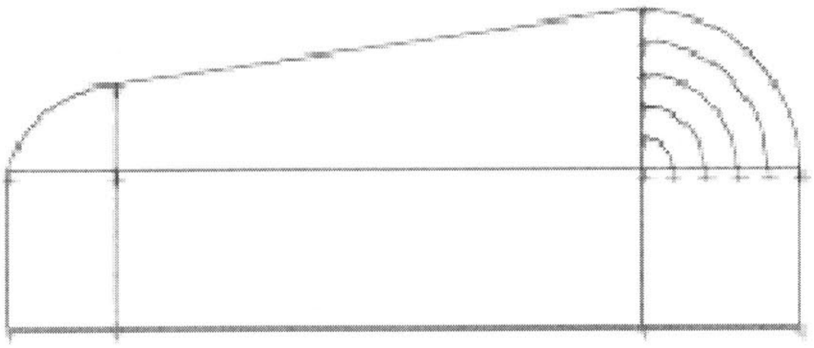

Figure 3-19: Geometry with Turning Vanes and No Settling Length

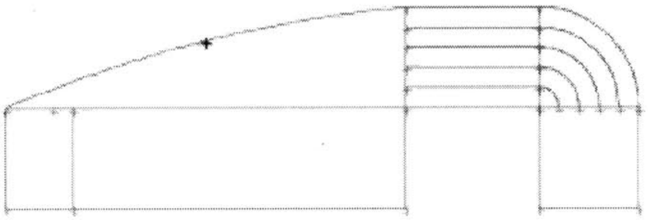

Figure 3-20: Geometry with Turning Vanes

the regenerator.

Several tests were performed with the geometry in figure 3-14 to determine if the depth of the model was important and if the mesh had any effect on the velocity distribution.

Variations on a different header shape in figure 3-22 were simulated to see if small changes in header design could produce significant changes in velocity distribution. The header shape is defined by a circular arc that passes through a point above the center of the regenerator. The center point varied from 0.055 m to 0.075 m above the regenerator face. The inlet turn was modified in each case to ensure a more continuous slope from the inlet turn to the header housing. This entailed reducing the turn from 90° to approximately 75° in the extreme cases.

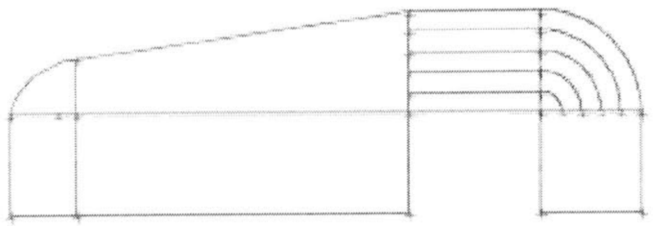

Figure 3-21: Geometry with Turning Vanes

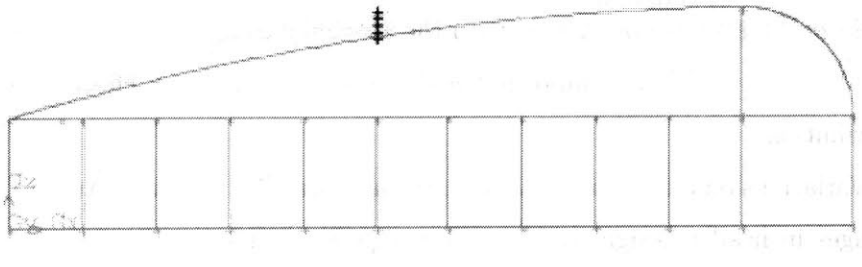

Figure 3-22: Small Variations in Header Shape

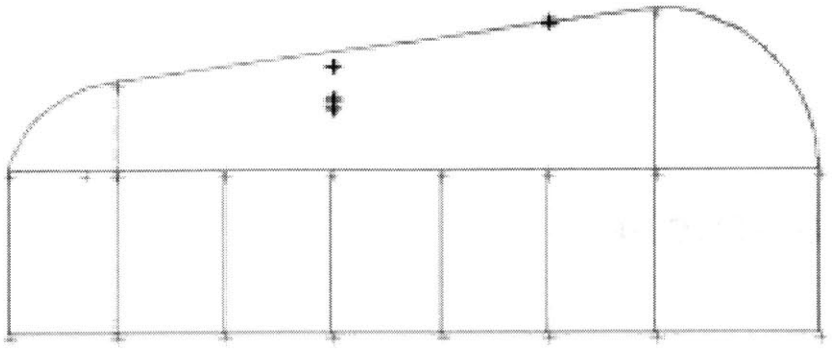

Figure 3-23: Comparison of Header Designs

The smaller-aspect-ratio geometries more closely resemble actual rotary regenerators in size. Tests with further header shapes were based on the 0.3 m radius in the shorter geometries. Figure 3-23 shows the three basic designs that were studied.

Two of these shapes are presented in figures 3-15 and 3-20 (without turning vanes). The third is specified in FLUENT by connecting the four points with a best-fit third-order polynomial that is automatically calculated in FLUENT. The left-of-center point is at 0.15 m from the left end of the regenerator and 0.03 m above the regenerator face. The right-of-center point is 0.25 m from the left end of the regenerator and 0.07 m above its face.

Chapter 4

Results For Two-Passage And Corner-Radii Models

Many of the simulations performed with the two-passage models showed that manufacturing tolerances of the sort that were dealt with here have little effect on overall regenerator efficiency. The corner radii tests showed that larger corner-radii can have a significant effect on the heat-transfer rate into or out of the fluid.

4.1 Two-Passage Models

The two-passage tests all showed a very weak connection between channel deviations and overall effectiveness of the two passages. Other factors such as channel aspect ratio had a more significant impact on overall performance.

4.1.1 Center-Wall Offset Tests

The first tests performed on the square two-passage models were for comparison with published results of analytical solutions for the frictional characteristics to establish the modeling techniques [35][34]. Some of the cross sections are displayed in figures 3-2, 3-3, 3-4 and 3-5. Figure 4-1 shows the numerical results produced in FLUENT compared to the analytical results published by Shah and London (1980) [35]. The

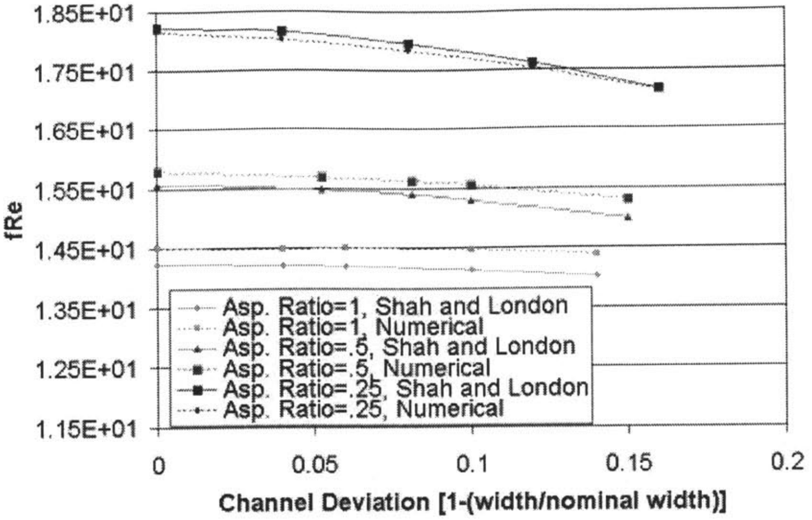

Figure 4-1: Comparison of Numerical Results and Shah and London (1980) Results for Friction Factor Times Reynolds Number Vs. Channel Deviation

graph plots the friction factor times the Reynolds number against the channel deviation for three nominal aspect ratios of 1, 0.5 and 0.25. The analytical and numerical results match well for all aspect ratios and show identical trends as the channel deviation increases. The close agreement between analytical and numerical models supports the accuracy of numerical techniques employed.

In addition to figure 4-1 a graphical technique was used to confirm the differences in pressure at the passage inlets. Tests that used an inlet plenum chamber did not have identical pressures at either the passage inlets or outlets. This was shown to be due to streamline curvature. When one of the passages is larger than the other, a disproportionate amount of fluid flows through that passage. Streamline curvature results from this type of flow situation.

The graphical technique consisted of approximating the radius of curvature of the streamlines from a FLUENT generated profile of the flow-field. Then equation 2.10 was used to calculate the pressure difference over a given distance. This value was compared to the numerically generated pressures at those locations. Figure 4-2 shows

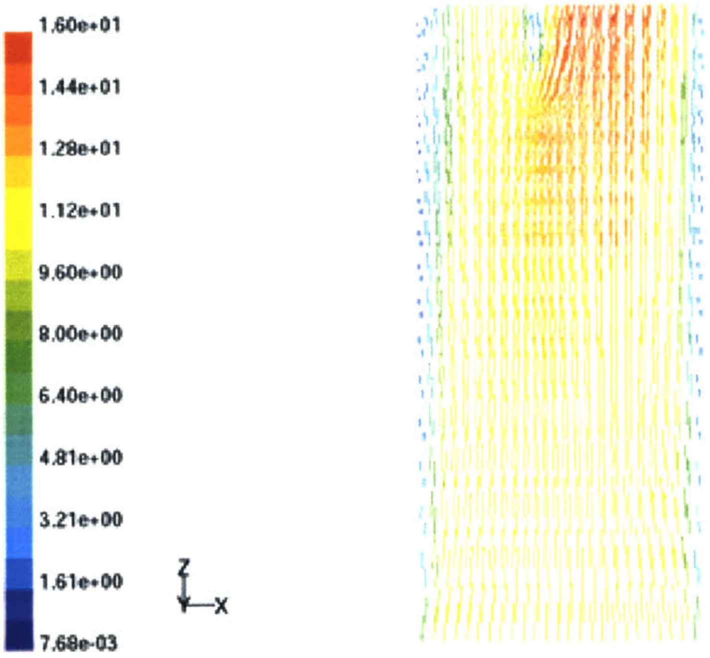

Figure 4-2: Inlet Velocity Profile for a Two-Passage Offset Wall Test. Flow Enters From Bottom and Splits Into Passages Near the Top

a typical profile for these tests in the inlet region.

The approximate method predicted a pressure difference of 27 Pa and the numerical difference was 38 Pa. These values are of the same order of magnitude and suggest that the numerical pressure-field calculations are probably accurate. Better agreement between the two methods is unlikely because of the approximations built in to the graphical technique such as approximating a constant radius of curvature as well as the radius itself, assuming constant velocity along the streamline, etc. These pressure differences are small, on the order of a percent of the total static-pressure drop through the passage.

Mesh Independence

Several simulations were run with the two-square-passage geometry shown in figure 3-2 using various mesh densities to determine whether the mesh used was fine enough to provide reliable results.

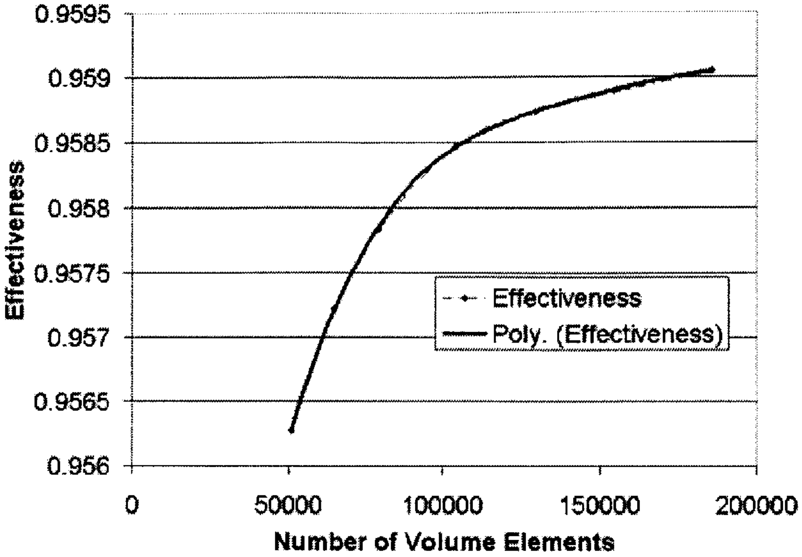

Figure 4-3: Mesh Dependence of Effectiveness on Volume Elements in Two-Passage Square Model

Figure 4-3 shows that although the true effectiveness is not reached until the number of volume elements is around 200,000 the final effectiveness can be estimated from simulations using far fewer elements. The scale should also be noted; there is very little difference in effectiveness over a large range of elements: 0.25% change from 40,000 to 185,000 elements. For most applications it is not necessary to extrapolate the true effectiveness at all, the estimate obtained by running a simulation with a mesh density similar to the one with 40,000 elements would provide an adequate estimate.

The pressure drop was measured at various mesh densities as well. Figure 4-4 shows the trend and curve fit of points. The change in pressure drop over this interval is small and the approximation obtained by using a relatively small number of elements will be adequate in most design situations.

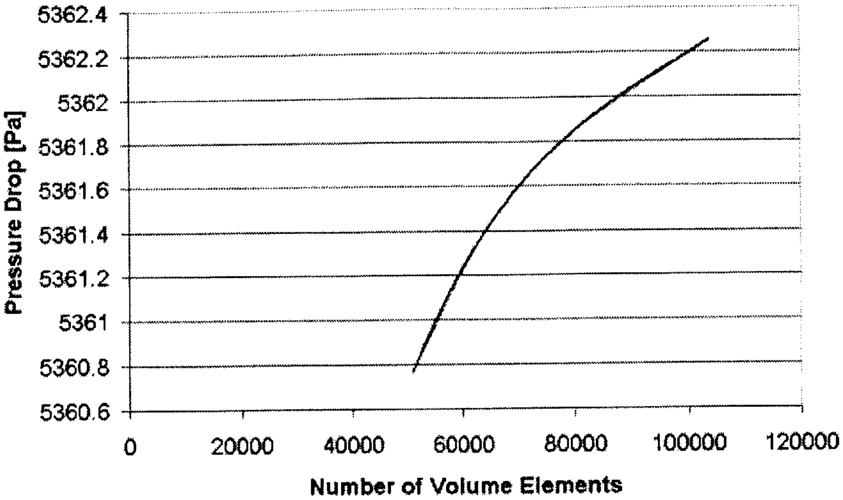

Figure 4-4: Mesh Dependence of Pressure Drop on Volume Elements in Two-Passage Square Model

Cooling Tests

In rotary regenerators each passage is cyclicly heated and cooled. Therefore simulations were performed where the walls cooled the fluid instead of heating it. The same geometries and mass flow rates were used and the same variable property effects were measured as with the heated cases. Figure 4-5 shows that using variable properties gives a more conservative estimate of the effectiveness than using constant properties; the opposite effect that is seen in the heated tests.

4.1.2 Variable Property Effects

When designing or modeling heat exchangers the properties of the working fluids are typically specified at some average temperature and assumed constant throughout the heat exchanger. This can potentially lead to errors in calculating effectiveness, required mass flow rates, pressure drops, etc. The change in effectiveness for each individual property being specified at the average temperature of the fluid, instead of being specified according to the appropriate polynomial in section 3.1.2, is shown

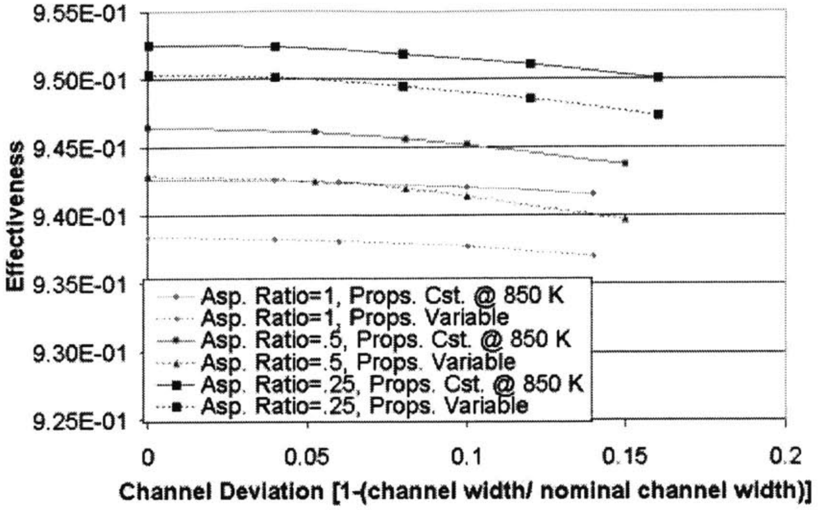

Figure 4-5: Two-Passage Model Variable and Constant Property Comparison With Fluid Being Cooled

in figures 4-6, 4-7, 4-8 and 4-9

Figures 4-6 and 4-7 show that specifying the density as an incompressible ideal gas (a Bousinesq approximation) and viscosity according to equation 3.3 do not result in any appreciable difference in the heat-exchanger effectiveness. Figure 4-8 shows a slightly lower predicted effectiveness for variable, as opposed to constant, heat capacitance for the hot-wall tests.

The fluid property that has by far the largest effect on the heat-exchanger effectiveness is the thermal conductivity. Figure 4-9 shows that a variable thermal conductivity increases the effectiveness by about 0.4%; this is for the cases with a nominal aspect ratio of one. This is not a large increase, however, if the deviation of the effectiveness from unity is measured then the change is 8.1% less defect from perfect efficiency using a variable thermal conductivity.

The net effect of using all variable properties versus all constant properties is shown in figure 4-10. The trend of higher predicted effectiveness for variable properties is dominated by the thermal-conductivity contribution.

All other tests in this study, except the ones presented here, are using variable

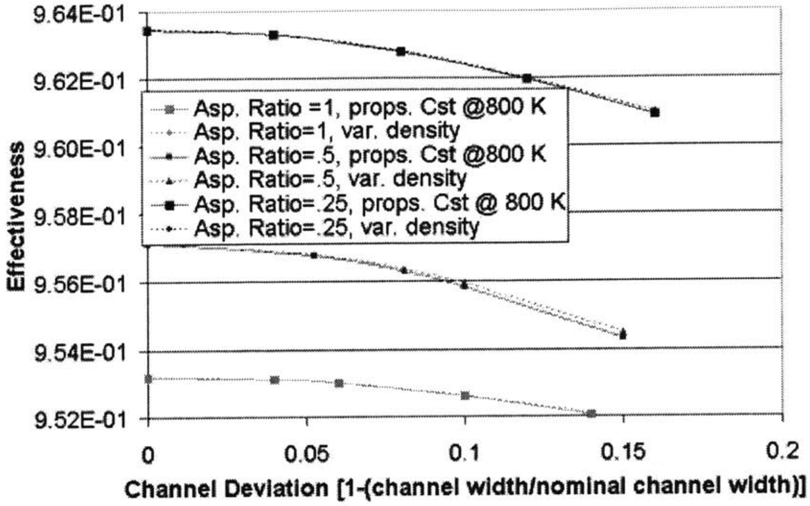

Figure 4-6: Effectiveness vs. Channel Deviation, Heated Two-Passage Cases, Comparison of All Properties Constant @ 800 K and Variable Density

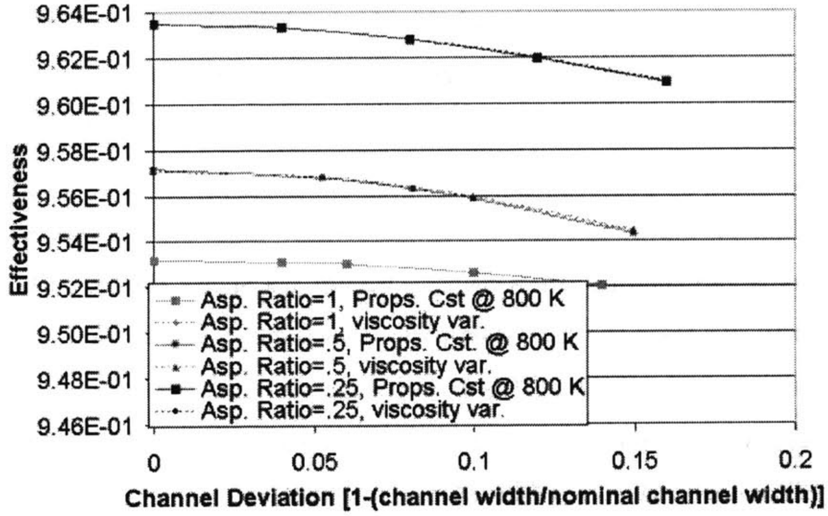

Figure 4-7: Effectiveness vs. Channel Deviation, Heated Two-Passage Cases, Comparison of All Properties Constant @ 800 K and Variable Viscosity

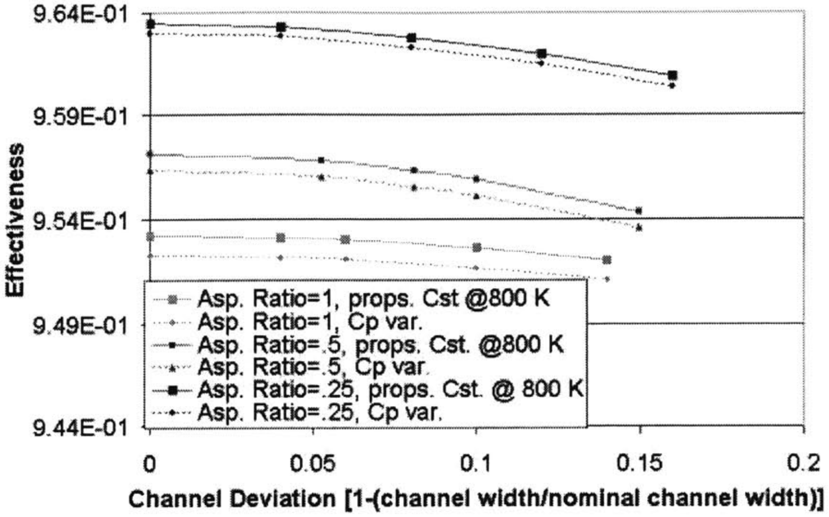

Figure 4-8: Effectiveness vs. Channel Deviation, Heated Two-Passage Cases, Comparison of All Properties Constant @ 800 K and Variable Specific Heat

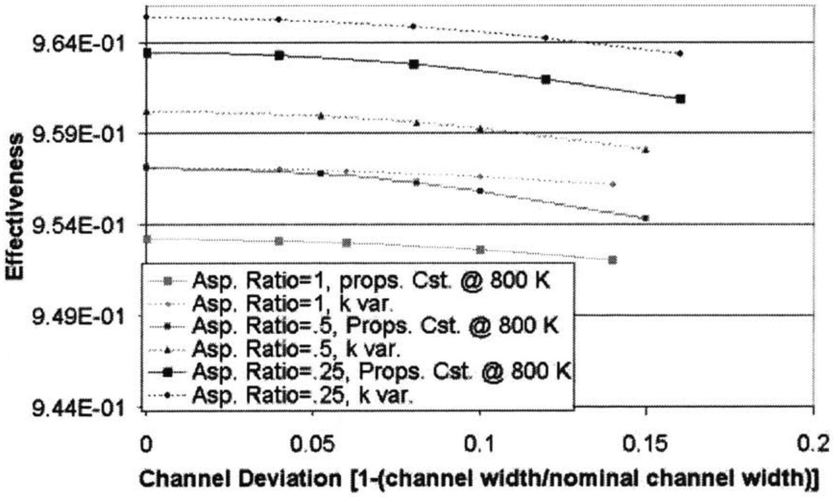

Figure 4-9: Effectiveness vs. Channel Deviation, Heated Two-Passage Cases, Comparison of All Properties Constant @ 800 K and Variable Thermal Conductivity

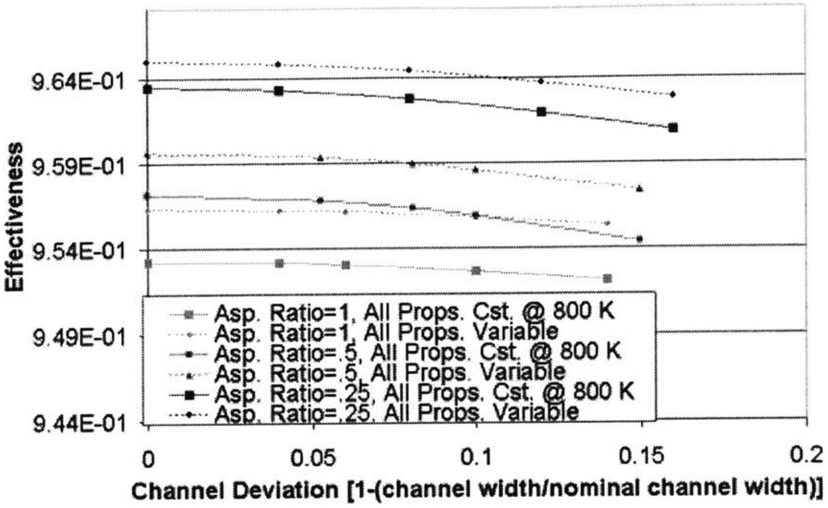

Figure 4-10: Effectiveness vs. Channel Deviation, Heated Two-Passage Cases, Comparison of All Properties Constant @ 800 K and All Properties Variable

properties. There is little extra expense associated with using variable properties so that the slightly more accurate results justify using the variable-property method.

Another aspect of property specifications that was investigated was the sensitivity of the effectiveness to the temperature at which the properties are specified. Two temperatures were compared, 800° K and 830° K. The two-square-passage geometry with the fluid being heated was used for the comparison shown in figure 4-11

There is virtually no difference in effectiveness between the tests at the two temperatures. The percentage change in 1-ϵ is 0.85%, so there is no significant change. Some of the other simulations were run at 800° K when the actual mean temperature is closer to 830° K. No distinction is made in these tests because figure 4-11 demonstrates that any differences are negligible.

All of the simulations with these offset-wall deviations have shown that the heat-exchanger effectiveness is very insensitive to the wall offset type of non-uniformities. The aspect ratio of the passages has an order of magnitude larger impact on the effectiveness than the channel deviation.

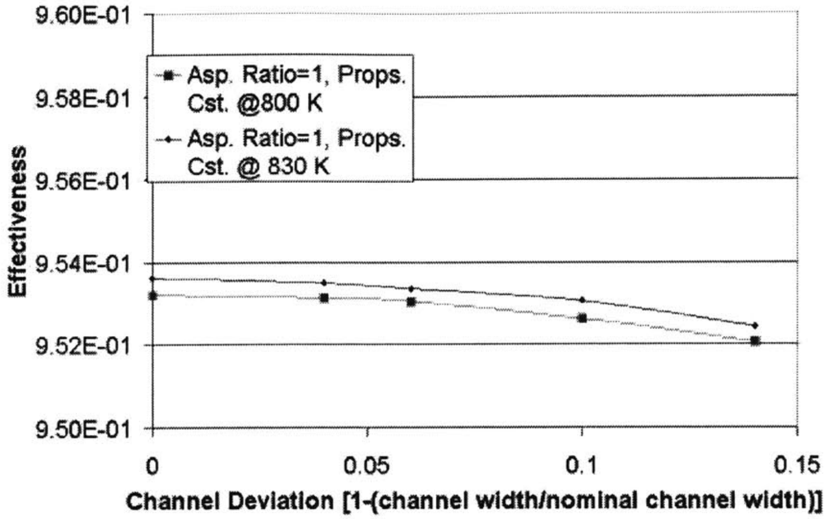

Figure 4-11: Effectiveness vs. Channel Deviation, Heated Two-Passage Cases, Comparison of Properties Constant @ 800 K and 830 K

4.1.3 Two-Passage Models With Center-Wall Deviation in Flow Direction

The simulations performed using geometries similar to that in figure 3-7 showed again that there is very little change in effectiveness even with large channel deviations. Figure 4-12 shows that the percentage change in effectiveness for a channel deviation as large as 0.7 compared to no deviation is about 0.8%. If 1-ϵ is used as an indication the change is 15%, which is still relatively small given how large the channel deviation is.

The pressure drop in the individual passages is more sensitive to the channel deviation and also to the mesh density than is the effectiveness. Figure 4-13 shows that the passage deviation results in a significantly larger pressure drop in the smaller passage although it remains approximately constant in the larger passage. This trend can be explained qualitatively by noting that the smaller channel size means more streamline-curvature effects on the channel inlet and, to a lesser extent, the outlet. The streamline curvature creates a slightly higher inlet pressure in the smaller passage;

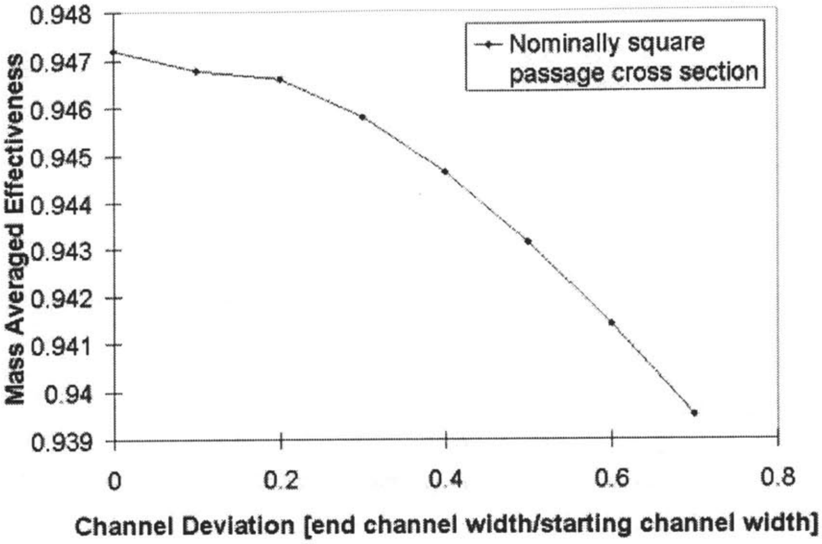

Figure 4-12: Effectiveness vs. Channel Deviation, Heated Two-Passage Cases, Channel Width Changing in Flow Direction

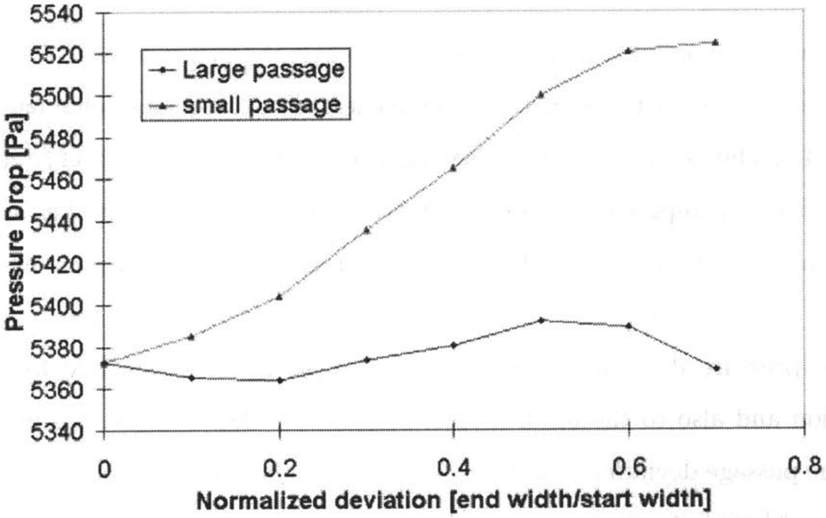

Figure 4-13: Presure Drop vs. Channel Deviation, Heated Two-Passage Cases, Channel Width Changing in Flow Direction

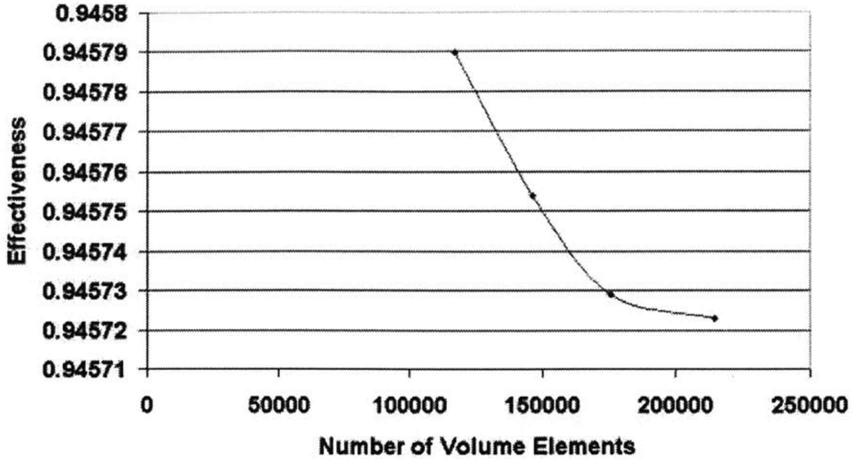

Figure 4-14: Effectiveness vs. Number of Volume Elements, Heated Two-Passage Cases, Center Wall Deviation Along Flow Direction

while the added mass flow rate to the larger passage and its width expansion that cause a diffuser-like effect offset the otherwise expected decreased pressure drop.

The inflection points and zero-slopes in the curves in figure 4-13 are related to the mesh distribution as discussed below and should not be used as any more than a guideline for the relationship between pressure and channel deviation.

Mesh Independence

The dependence of the effectiveness on the mesh was determined using the geometry with a normalized deviation of 0.3. Four levels of mesh density were used to record the effectiveness and pressure drop dependence. Figures 4-14 and 4-15. Unlike the other mesh independence tests, figure 4-14 shows a slight decrease in effectiveness as the mesh density increases. The scale should be noted: the change in effectiveness is less than 0.01% and is therefore negligible. The predicted effectiveness at approximately 100,000 elements, which is the density used for the rest of this set of simulations, can be considered the true effectiveness.

The pressure-drop to channel-deviation relationship displayed in figure 4-13 shows

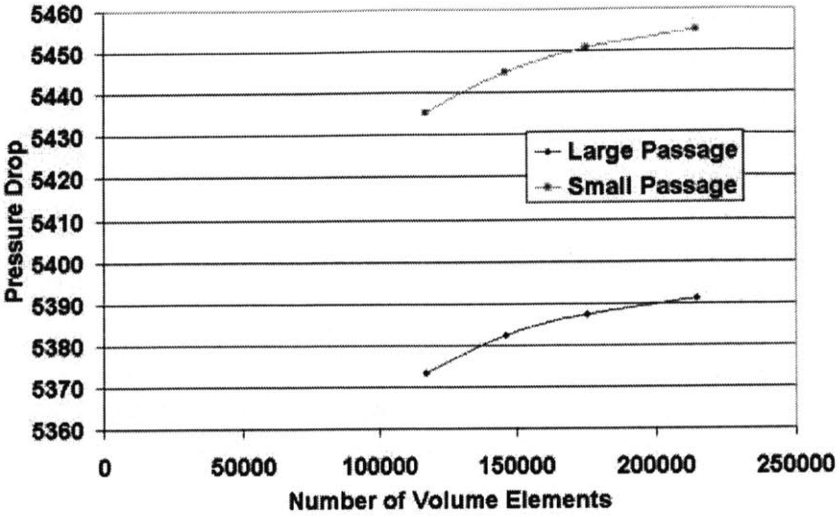

Figure 4-15: Pressure Drop vs. Number of Volume Elements, Heated Two-Passage Cases,Center Wall Deviation Along Flow Direction

a correlation between the pressure drop and the mesh density in each passage. As the channel deviation becomes larger, more cells were added to the larger passage so that the cells at the large passage outlet would not become so large as to give inaccurate results. A consequence of this is that the mesh at the large passage inlet became finer as the channel deviation became larger (the channel did not change size at the inlet, but as more cells were added to one end they had to be added to the other in the structured meshing scheme that was used). The smaller passage experienced similar mesh changes: only the number of cells was constant and the volume became smaller as the channel deviation increased. The mesh was changed when the channel deviation was 0.3, 0.5 and 0.7. These deviations correspond to sections on the two curves where the slope changes, suggesting that there is some bias in the pressure drop because of mesh-density variations. The effect is more pronounced in the large passage because the number of elements was changed at certain intervals as well as the mesh-density fluctuation from changing the channel size at every test.

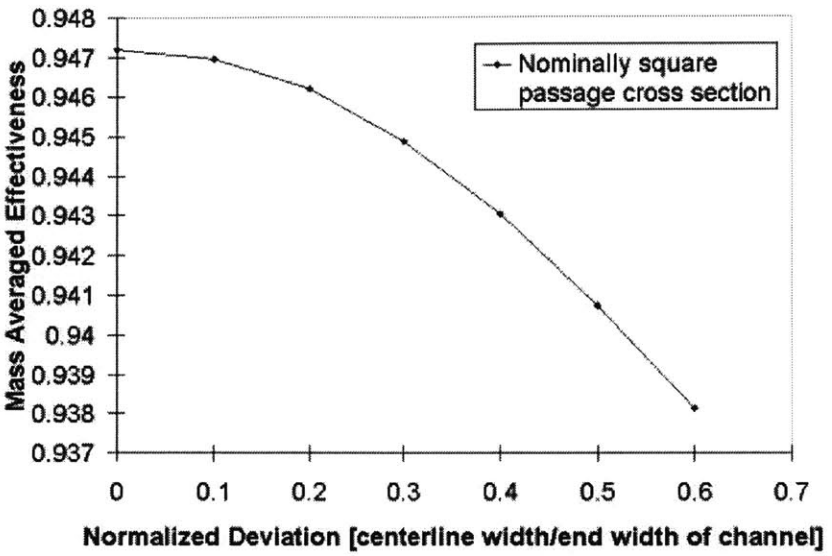

Figure 4-16: Effectiveness vs. Channel Deviation, Heated Two-Passage Cases, Wavy Center Wall Deviation

4.1.4 Center-Wall With Wavy-Deviation Tests

The warped center-wall deviation tests again showed little change in overall effectiveness for the two passages even with large deviations. Figure 4-16 shows the mass averaged effectiveness of both channels versus the channel deviation. Note that the actual effectiveness drop is only 0.96%. The difference between the maximum plotted deviation and zero deviation if 1-ϵ is measured is 14.7%.

The channel-deviation versus pressure-drop relation is shown in figure 4-17. The change in mesh density over the range of deviations is similar to the previous cases where the larger channel has more cells added as the deviations get larger and the smaller channel has the same number of cells but they are more compact as the deviation grows.

In contrast to the previous set of tests, the wavy-deviation tests show that the pressure drop increases significantly in both channels as the deviation grows. Changes of greater than 4% were recorded for the large passage and up to 6.7% for the small

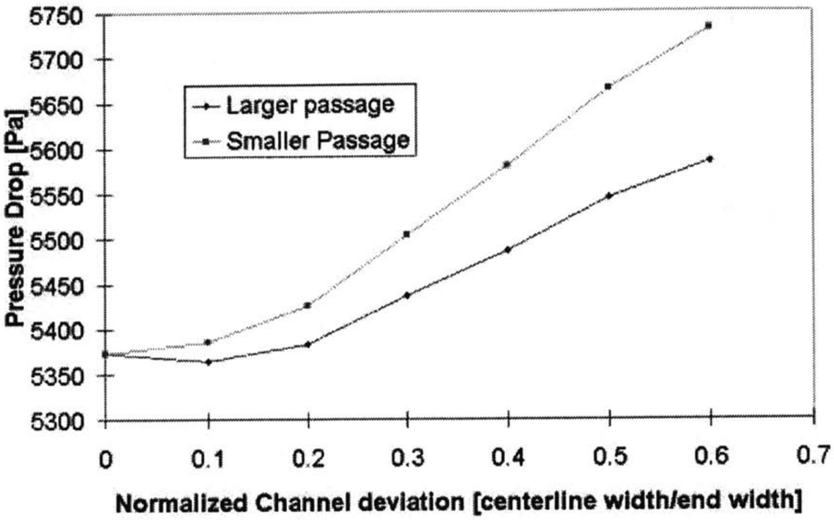

Figure 4-17: Pressure Drop vs. Channel Deviation, Heated Two Passage Cases, Wavy Center Wall Deviation

passage. An increase in pressure-drop in the small passage is expected. The increase in pressure-drop in the large passage is due to the nature of the non-uniformity. The bend in the center wall acts as a diffuser and nozzle in series; they cancel each other out so to speak. The increase in mass flow through the passage is the cause of the increased pressure-drop. The changes in the slope of the pressure curves correspond to the tests where the number of mesh elements were changed. The change in slope is not large and therefore the dependence of the pressure drop on the mesh density is less than in the previous tests. This is demonstrated in the next section.

Mesh Independence

Similar to the previous two types of non-uniformities, one of the geometries with wavy deviations was simulated with various mesh densities to see the impact on effectiveness and pressure drop. The geometry simulated had a maximum normalized deviation of 0.1. Figure 4-18 shows that the change in effectiveness over the range of mesh sizes is only 0.1%, essentially negligible.

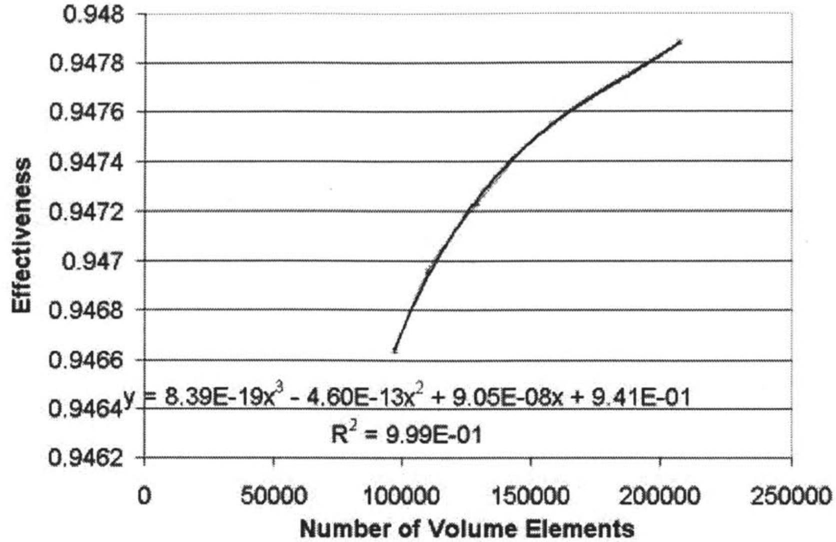

Figure 4-18: Effectiveness vs. Number of Volume Elements, Heated Two-Passage Cases, Wavy Center Wall Deviation

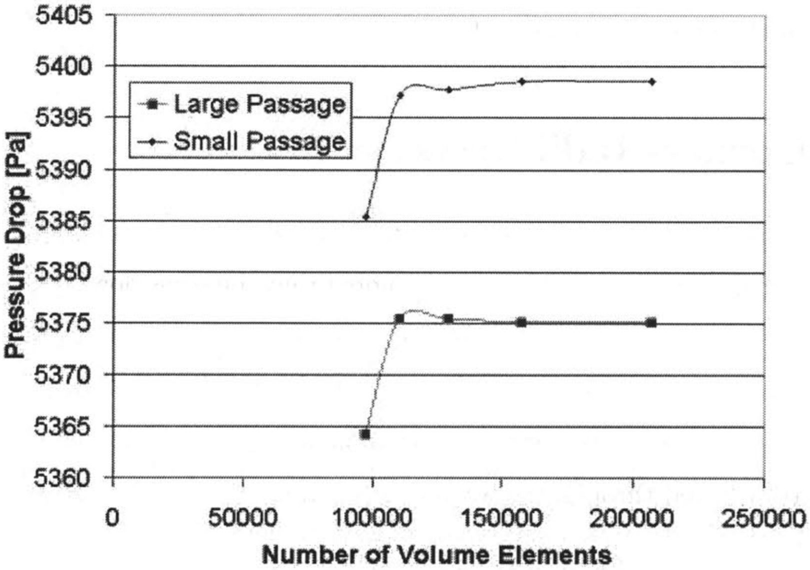

Figure 4-19: Pressure Drop vs. Number of Volume Elements, Heated Two-Passage Cases, Wavy Center Wall Deviation

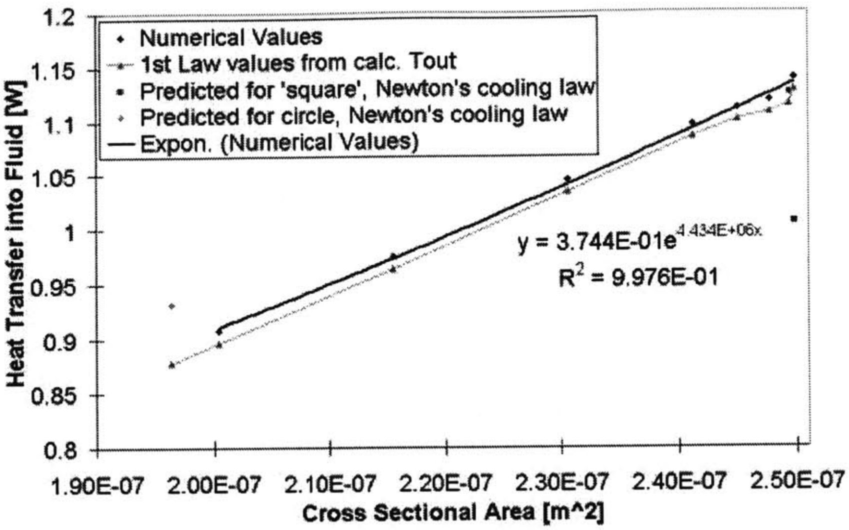

Figure 4-20: Heat Transfer Into Fluid vs. Cross-Sectional Area

Figure 4-19 shows that for more than about 110,000 volume elements the pressure drop in either passage is approximately constant. That is for the test with a maximum normalized channel deviation of 0.1.

4.2 Corner-Radii Tests

The single-passage tests with varying corner radii shown in figure 3-9 all have essentially identical effectiveness. It should be noted that the mass flow rate per unit area in all the tests was held constant, not the total mass flow rate. The lack of variation in effectiveness between tests suggested the use of overall heat transfer through the walls as a measure of the performance variation among geometries. Figure 4-20 shows the heat transferred through the walls as a function of the cross-sectional area of the model.

The first law calculations plotted in figure 4-20 are based on the temperatures and pressures calculated in FLUENT and account for flow work. That does not say anything about whether the temperatures and pressures calculated in FLUENT are correct, only that the first law is satisfied. The two extreme cases here are nearly square cross-section and a nearly circular cross section. The Nusselt numbers for these cross sections are well established; therefore analytical solutions for the heat transfer can be obtained. These are also plotted in figure 4-20. The analytical solutions do not match well because the boundary conditions that the Nusselt numbers are based on do not hold under these circumstances. An average Nusselt number was obtained and the heat transfer calculated was based on that average Nusselt number (see section 2.2.2). The analytical prediction of heat-transfer is in the same order of magnitude as the numerical prediction. This is about as accurate as one can hope to obtain given that the heat transfer coefficient is based on an approximated Nusselt number and on the idea of a hydraulic diameter.

The heat flow per unit mass flow through the walls was also plotted against the cross-sectional area. Figure 4-21 shows that as the cross-sectional shape changes from almost circular to a square, the heat transfer per unit mass flow rate decreases. This is not surprising: the heat-transfer coefficient it higher for a circle than for a square given the same hydraulic diameter and thermal conductivity. The higher heat transfer per unit mass flow suggests that perhaps circular passages could be implemented in place of traditional square passages without penalties in heat-exchanger efficiency.

An unexpected anomaly surfaced when attempting to define the hydraulic diameter in these cases. The hydraulic diameter as defined in equation 2.33 rises and then drops when changing the cross-sectional area as shown in figure 4-22. It is difficult to rationalize this anomaly; therefore a different hydraulic diameter was used and compared against the numerical results and other analytical results for pressure drop calculations in figure 4-23.

The new hydraulic diameter is based on equating the cross-sectional area of the passage to a circle with equal cross-sectional area and using the diameter of that circle as the hydraulic diameter of the passage.

The new hydraulic diameter eliminates the drastic predicted increase in pressure drop that is obtained calculating with a standard hydraulic diameter shown in 4-23. The trend is similar to the numerically produced trend; however, the accuracy of

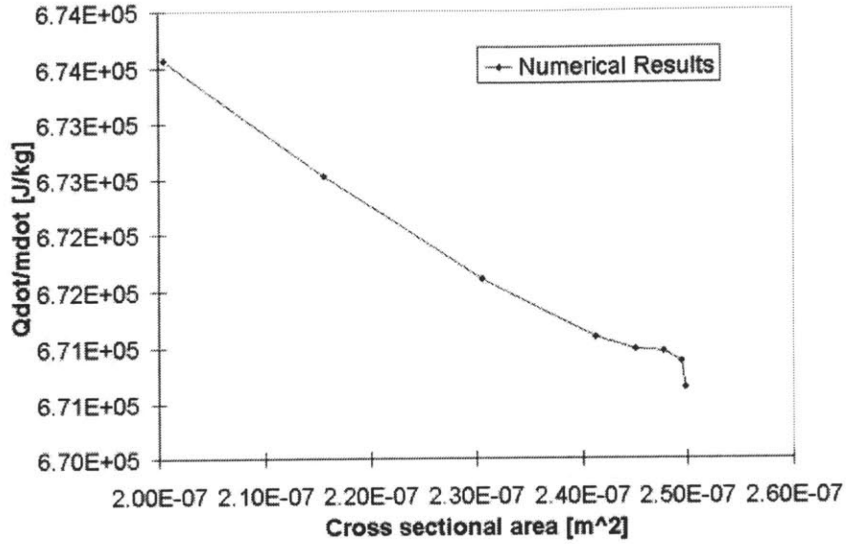

Figure 4-21: Heat Transfer Into Fluid Per Unit Mass Flow vs. Cross-Sectional Area

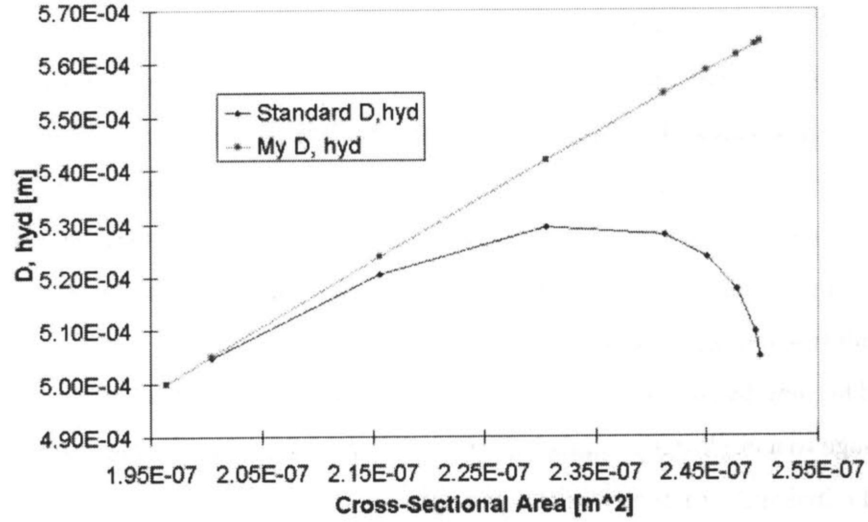

Figure 4-22: Hydraulic Diameter vs. Cross-Sectional Area

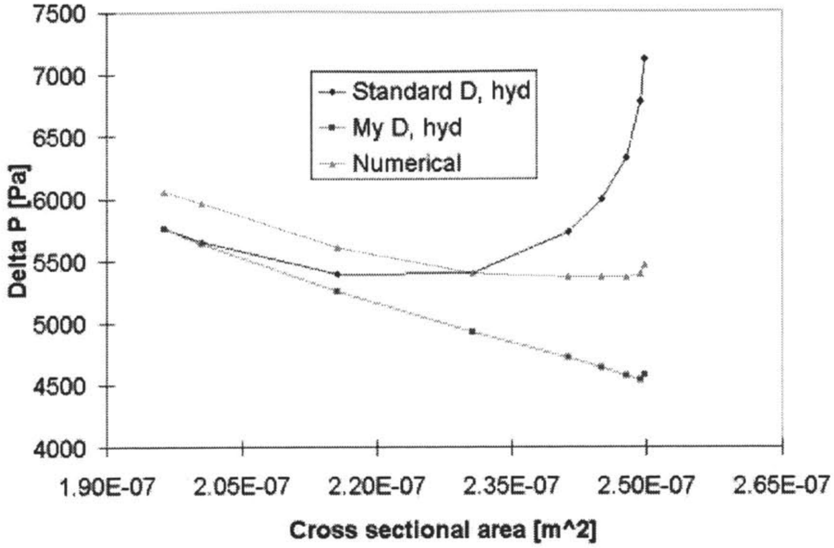

Figure 4-23: Pressure Drop vs. Cross-Sectional Area

either hydraulic diameter in predicting pressure drop is poor.

Mesh Independence

The heat transferred to the fluid was measured for various numbers of volume elements to determine how much the mesh density affected the heat transfer. Figure 4-24 shows that even for 50,000 elements the predicted heat transfer is approximately 97.6% of the asymptotically approached maximum.

All other corner-radii tests were performed using between 110,000 and 140,000 elements. No extrapolation was done when reporting results of heat transfer because of the insignificant difference between asymptotic maximum and actual numerical results using the above listed number of elements.

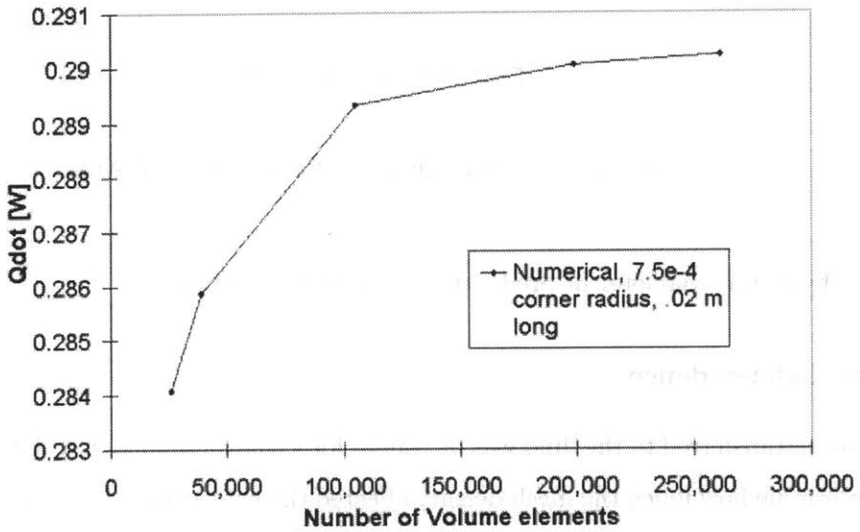

Figure 4-24: Heat Transfer Into Fluid Vs. Number of Volume Elements

Chapter 5

Inlet-Header-Test Results

The simulations of various inlet headers and incident flow show that the header shapes have a very strong effect on the velocity distribution into the regenerator and its effectiveness. None of these tests incorporated heat transfer; only pressure-drop and velocity-distribution data were recorded.

5.1 Incident Flow

The first series of tests was used to determine the effects that incident flow has on the effectiveness of a single regenerator passage. There is a strong correlation between the incidence angle and the overall effectiveness as shown in figure 5-1

The higher effectiveness is partially a result of the lower mass flow rate through the passage as the incidence angle increases. The lower mass flow rate produces a lower average velocity; therefore the fluid has more time to absorb heat, causing the outlet temperature and the effectiveness to go up.

The increased effectiveness is more than offset by the lower mass flow rate in the passage. The result is that the overall heat transferred into the passage decreases significantly as the incidence angle increases. Figure 5-3 shows that at a 75° angle the heat transferred to the fluid, given the identical inlet and boundary conditions, is 27% as much as with no incidence.

These tests can be used to assess the importance of velocity distribution at the re-

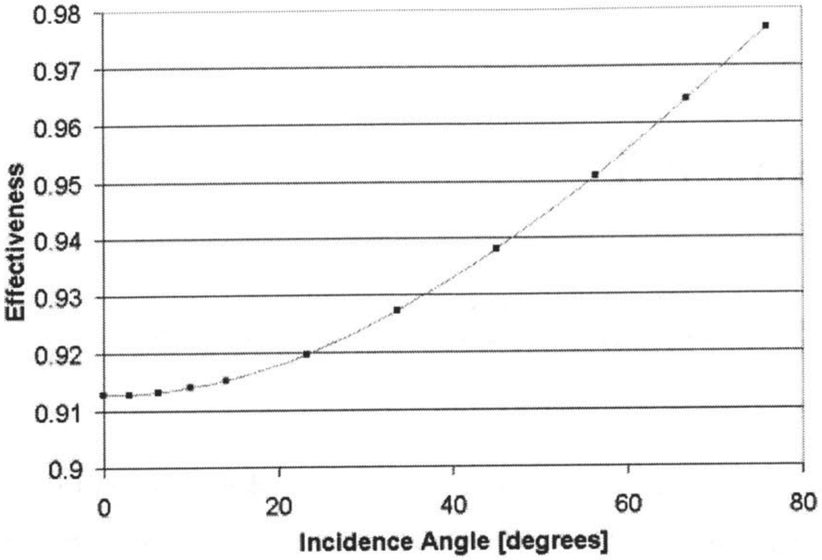

Figure 5-1: Effectiveness Vs. Angle of Incidence for Incident Tests

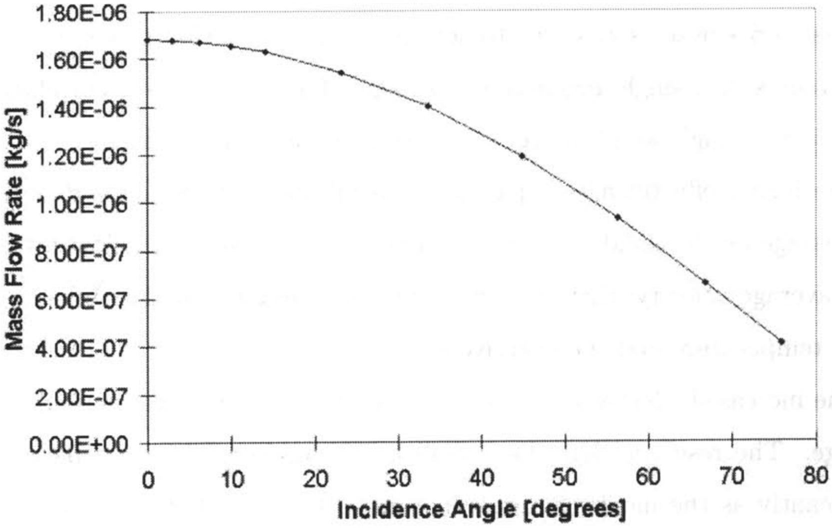

Figure 5-2: Mass Flow Rate Into Passage Vs. Angle of Incidence for Incident Tests

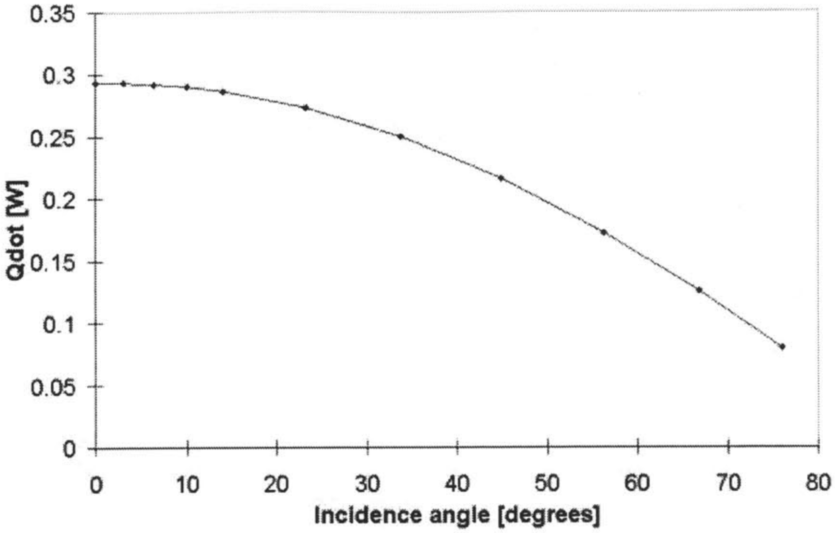

Figure 5-3: Heat Transferred Into Fluid Vs. Angle of Incidence for Incident Tests

generator inlet face. If the flow is highly skewed or poorly distributed the regenerator effectiveness will drop dramatically.

5.2 Porous Medium

Modeling the regenerator and inlet header explicitly required too much computing time. The regenerator was therefore modeled as a porous medium to reduce the mesh resolution required. The ability of the code to reproduce the expected pressure drop through the regenerator core via a porous medium was verified with these tests.

Figure 5-4 shows that over the entire range of temperatures that would be encountered in a typical regenerator the porous-media model produces a pressure drop within 3.5% of the analytical value.

Laminar and turbulent flow in the cylinder were simulated to confirm that neither turbulence or the turbulence model had any effect on the predicted pressure drop in the porous medium. The pressure results for both sets of tests are shown in figure 5-4.

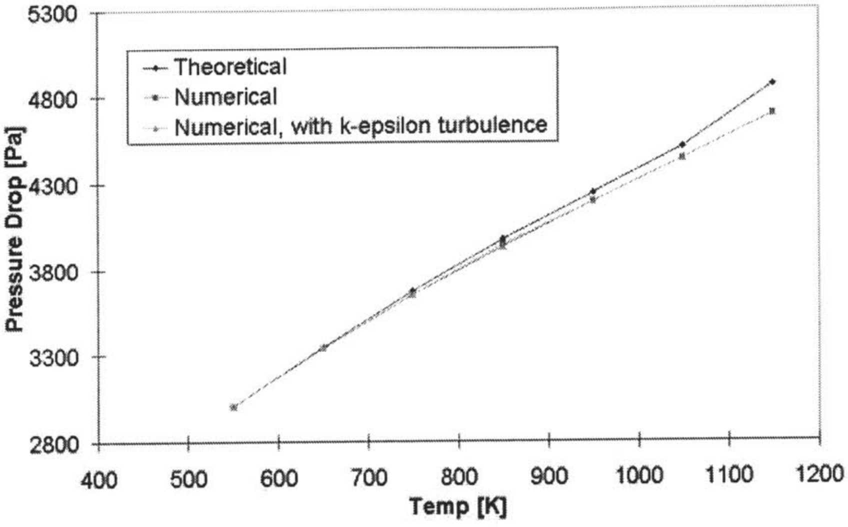

Figure 5-4: Pressure Drop Vs. Temperature for Porous Medium Tests

The percentage error in the numerical prediction of pressure drop and the analytical solution for a regenerator with 0.5 mm by 0.5 mm by 75 mm passages is shown in figure 5-5. At lower temperatures the difference is negligible. All inlet header tests were performed with a constant temperature of 525° K. At this temperature the pressure predictions are essentially identical.

5.3 Inlet-Header and Regenerator Tests

Tests that involved the modeling of the regenerator and the inlet header show that the shape of the header significantly affects the pressure drop in the header and the velocity distribution into the regenerator core.

5.3.1 Width Comparison

The high number of volume elements required for these simulations and the large number of simulations performed meant that any method of reducing the amount of header and regenerator that was modeled saved a significant amount of time. One of

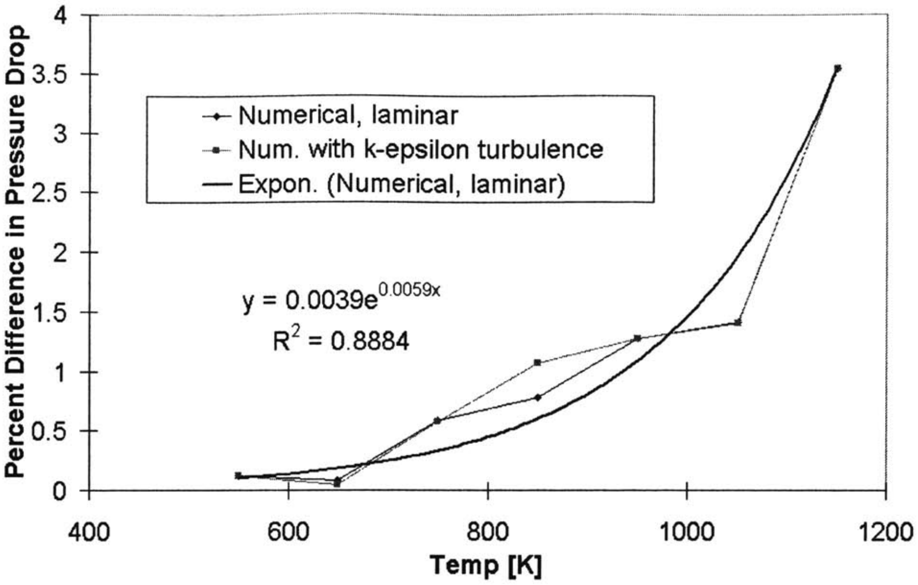

Figure 5-5: Percent Difference in Pressure Drop Vs. Temperature for Porous-Medium Tests

the most obvious methods was to reduce the width of the models. Initially the models were 0.2 m deep in the direction transverse to the flow. In the profiles displayed in Chapter 3 this is the direction into the page. This depth was chosen so that all turbulent eddies would be of a smaller length scale than the smallest dimension of the regenerator and would therefore not be truncated by modeling too small of a section. Another test was performed with a width of 0.1 m under otherwise identical conditions. Both tests have a header shape as displayed in figure 3-14. The pressure and z-velocity distributions at the regenerator inlet are shown in figures 5-6 and 5-7.

The pressure and z-velocity profiles are identical for both widths. The 0.2 m width test has a large enough width to account for even the largest eddies; therefore, the 0.1 m width was considered adequate and was used for most subsequent simulations. The values at 0.5 m show a disturbance in the trend over the inlet face. This is due to the proximity of the wall and also the turning of the flow as it rounds the edge of the wall, creating a small, one cell width, area of recirculation. The effect is observed in all graphs of the regenerator face and does not affect the

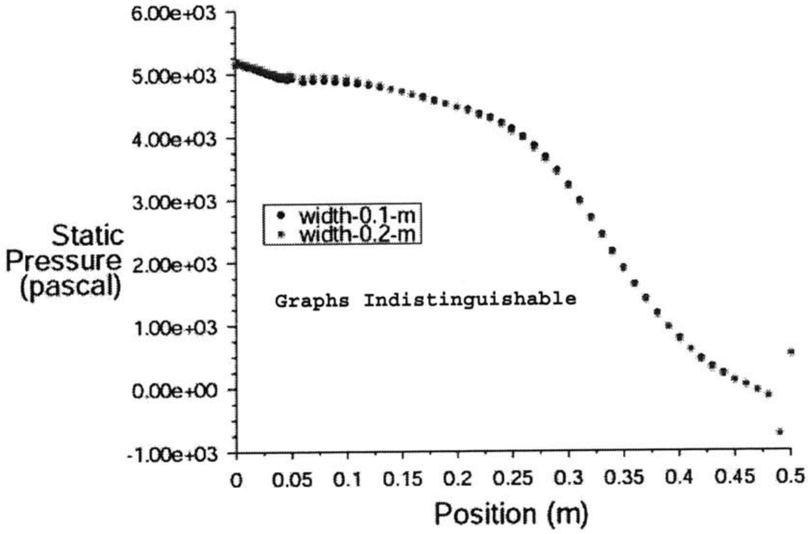

Figure 5-6: Pressure Comparison at Regenerator Inlet for Different Widths

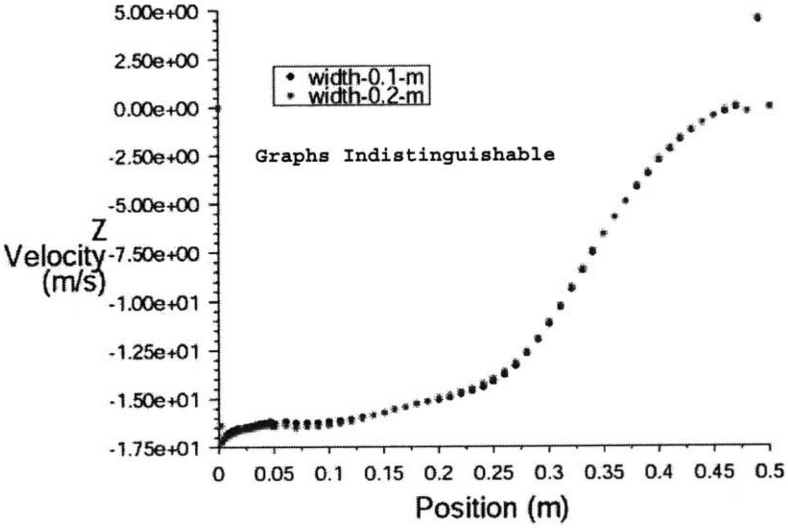

Figure 5-7: Z-Velocity Comparison at Regenerator Inlet for Different Widths

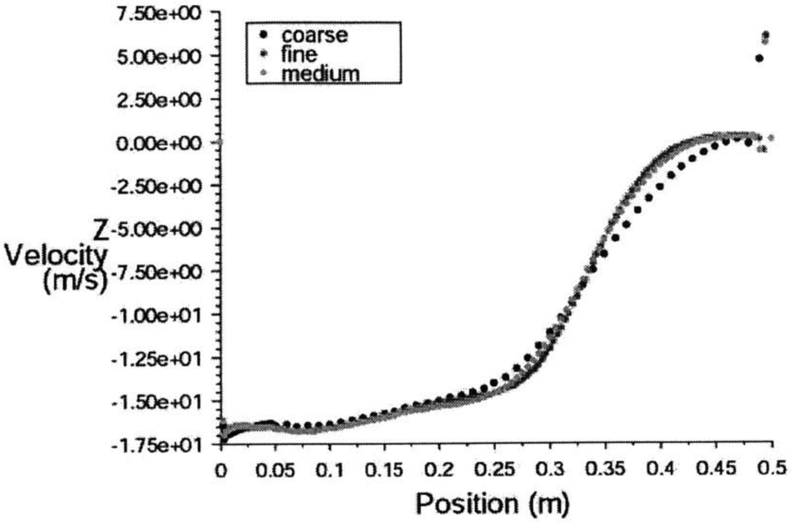

Figure 5-8: Z-Velocity Comparison at Regenerator Inlet for Different Mesh Densities

5.3.2 Mesh Independence

The smaller width that was used for mesh independence testing allowed for a much finer mesh to be used. The header shape that was chosen for this comparison is the same as was used for the width comparison, figure 3-14. Three mesh densities were compared; the velocity and pressure distributions are shown in figures 5-8 and 5-9. The coarsest mesh is that used for the width comparison and consists of approximately 110,000 cells. The finest mesh has approximately 316,000 cells. The smallest mesh dimension in the inlet header in either case is 0.002 m; the Kolmogorov length scale is on the order of $1\dot{1}0^{-6}$ m (see Appendix A). Resolution to the Kolmogorov-microscale is not exceptionally important in this study because changes in z-velocity and pressure that will result from very small turbulent eddies will not alter the average flow and pressure distributions significantly.

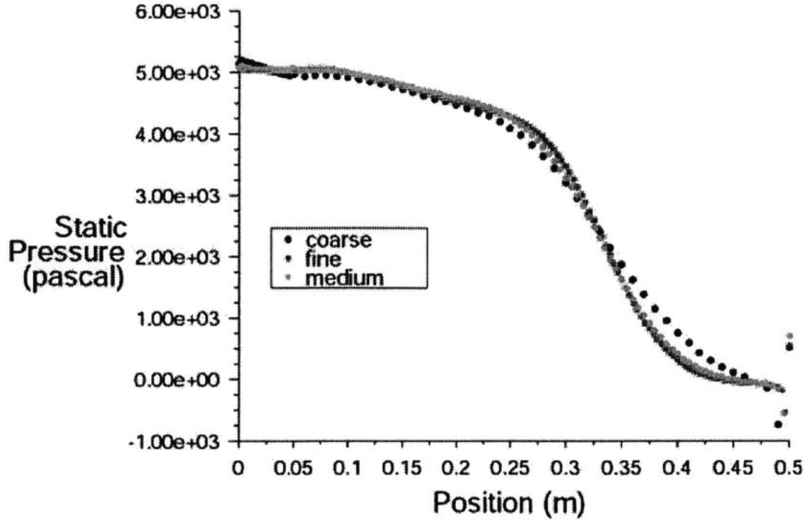

Figure 5-9: Pressure Comparison at Regenerator Inlet for Different Mesh Densities

5.3.3 Turbulence Models

The accuracy with which turbulence models can reproduce pressure and velocity fields is always in question. Many studies have been conducted to ascertain what models are most appropriate for different geometries and flow conditions. The complex geometries that are being simulated in this study mean that there are no direct comparisons among models in the literature with similar geometries. There are comparisons of k-ϵ turbulence models with similar flow conditions and also some experimental evidence that can be used to compare against the turbulence model results.

The header shape that was used for turbulence model comparisons is in figure 3-14. The RNG and realizable k-ϵ models have been shown to be more accurate than the standard k-ϵ model when simulating recirculating or in high shear flows under certain circumstances[39][9]. It is not clear whether this necessarily means that under the circumstances that are imposed in this study that any of the three turbulence models has a clear advantage. Simulations were performed in this study to determine whether the type of k-ϵ model was important in determining the flow distribution. Figures 5-11 and 5-10 show the pressure and z-velocity distributions into the regenerator face

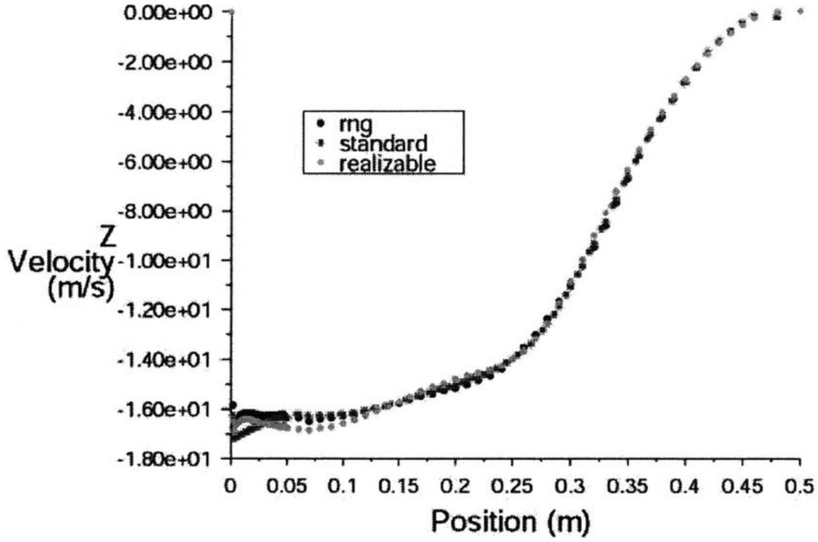

Figure 5-10: Z-Velocity Comparison at Regenerator Inlet for Different Turbulence Models

for the three different k-ϵ models.

The turbulence models all show very similar distributions. The differences among models become larger the farther from the inlet the measurement is. The RNG and realizable models agree more closely than either do with the standard k-ϵ model. The largest pressure difference between the RNG and realizable models is 2.5% and the largest pressure difference among the three is between the standard and realizable models and is 8.9% of the total static pressure at that location. The maximum differences in velocity between the realizable and RNG models is 2.4% and the maximum overall difference is between the standard and realizable models at 3.6%. When the difference in pressure from one end of the regenerator to the other is considered, the differences between models can be seen to be unimportant.

The agreement between models cannot be generalized. Shih et. al [39] have shown that in certain rotating flows, such as the classical backward-facing step, the realizable model predicts pressure and friction coefficients more accurately than the standard model. Speziale and Thangham [9] have shown in a similar backward-facing-step

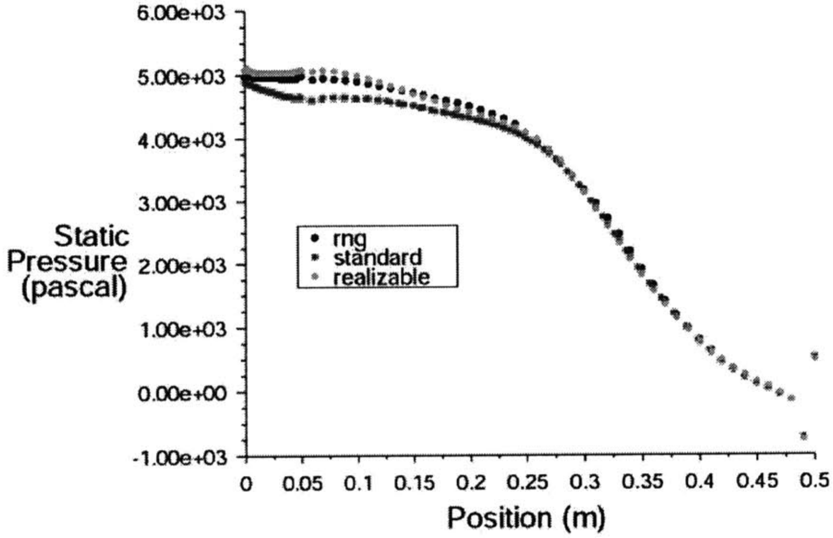

Figure 5-11: Pressure Comparison at Regenerator Inlet for Different Turbulence Models

situation that the RNG k-ϵ model predicts reattachment within 5% of experimental values compared to 12% for the standard model. Results such as these have prompted the use of either the RNG or the realizable models in this study.

There have been some experiments relating inlet header shapes to flow distribution as well. Kutchey and Julien [20] showed that increasing the slope of the header from a relatively flat slope with a sharp increase in slope near the center of the regenerator (equivalent to the left side in all geometries modeled in this study) to a continuous steeper slope can result in a better flow distribution into the regenerator.

Kohler [24] also experimented with altering the header shape to obtain a more uniform velocity distribution into the air-side of the regenerator. He found that a header shape roughly similar to the s-shaped header in figure 3-23 resulted in the most uniform flow distribution. There are several reasons that his findings may not be completely trustworthy. He does not give any detailed information about the header, inlet-pipe dimensions, mass-flow rate or temperatures. This lack of information makes it difficult to reproduce his results or be able to account for the difference between his experimental results and the numerical ones in this study.

5.3.4 Aspect Ratio

The aspect ratio of the regenerator and header can vary significantly. There is little information on how this can affect the flow distribution, if at all, or whether larger or smaller aspect ratios are more common in practice. Neither Kutchey and Julien [20] or Kohler [24] provided any information on the relative size of the regenerator to the header.

The geometry in figure 3-14 was chosen to test how the different aspect ratios impacted the flow distribution. Figures 5-12 and 5-13 show the velocity and pressure distribution along the regenerator inlet. The trends do not change with the different aspect ratios; rather the feature sizes are reduced proportionally. The low-velocity area to the right of the graph is indicative of the recirculation that occurs as the flow turns through the inlet pipe into the header. As the header becomes shorter this feature is simply reduced in width, not in magnitude. The points with zero velocity in the middle of figure 5-12 are the values at the wall, where a no-slip boundary condition is enforced. A similar trend is seen with the pressure graphs. This is important because it demonstrates that the basic shape of the header is more dominant than the actual dimensions. Therefore the same shape of header can be used in heat exchangers of different sizes with similar results.

5.3.5 Variable Pressure Drop in Regenerator Core

This far only a single representative pressure drop has been assigned in the regenerator core. This nominal pressure drop has been based on passages that are 0.5 mm by 0.5 mm by 75 mm. Not all regenerators will have these passage dimensions. It is therefore helpful to the designer to be able to predict the flow distribution into the core with different pressure-drop coefficients (for details about assigning these coefficients see section 2.1.3). The tests performed with the geometry in figure 3-21 and varying pressure-drop coefficients are shown in figures 5-14 and 5-15.

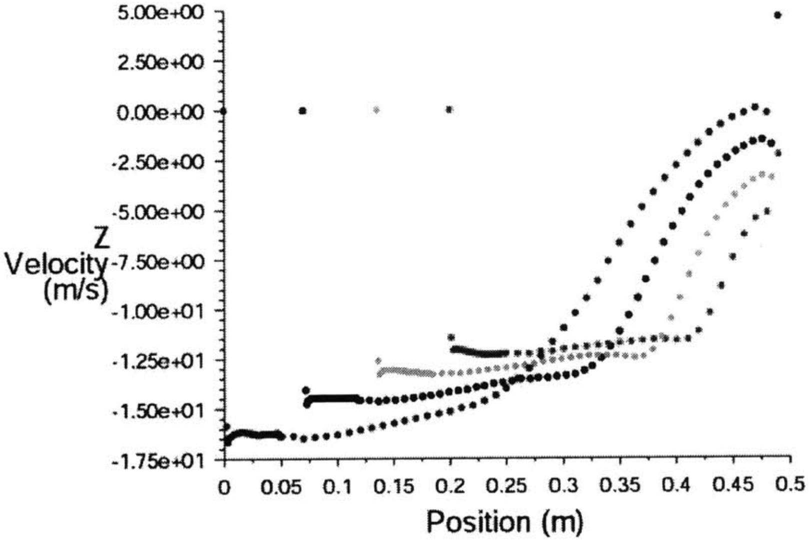

Figure 5-12: Z-Velocity Comparison at Regenerator Inlet for Different Aspect Ratios

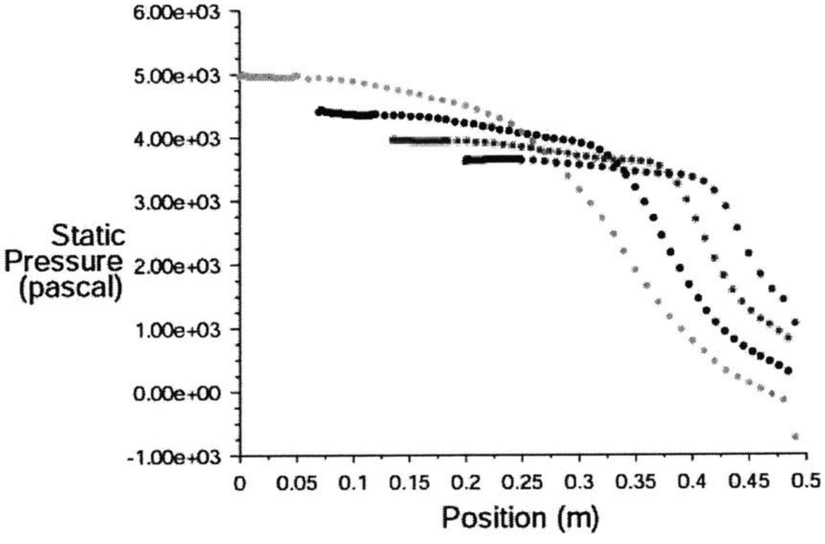

Figure 5-13: Pressure Comparison at Regenerator Inlet for Different Aspect Ratios

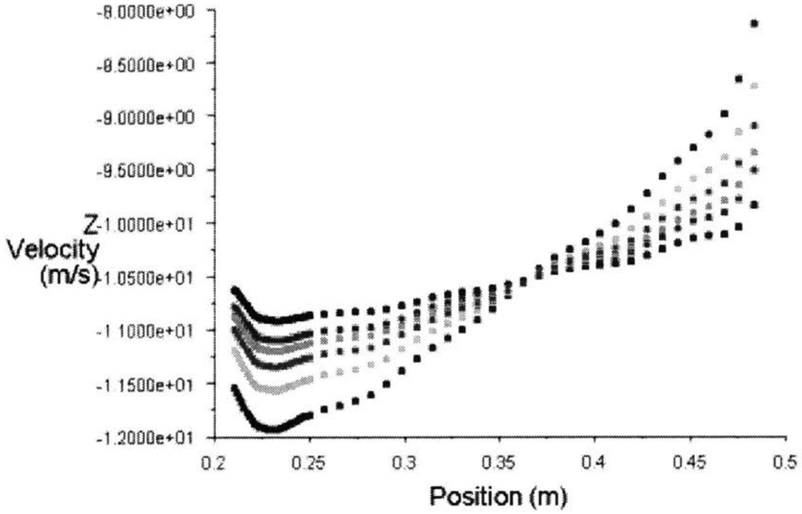

Figure 5-14: Z-Velocity Comparison at Regenerator Inlet for Pressure Drop Coefficients in Core

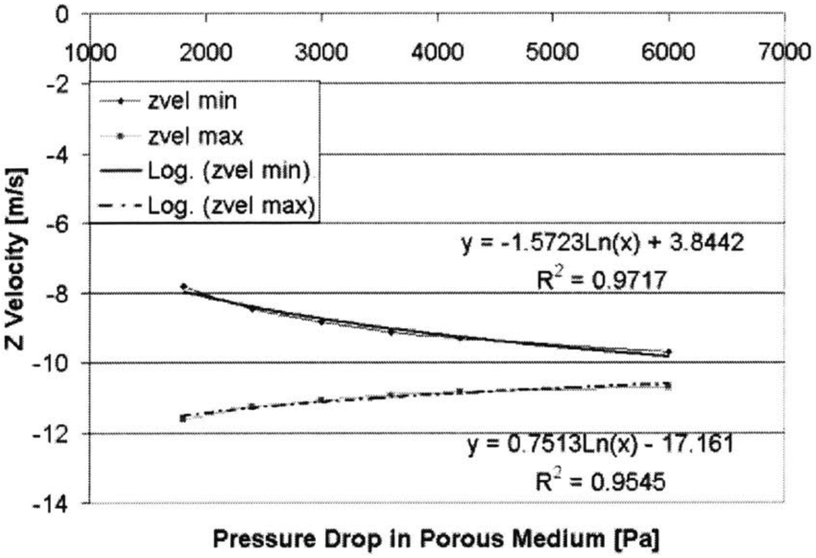

Figure 5-15: Z-Velocity Vs. Specified Pressure Drop in Core for 10.5 m/s Z-Velocity

Figure 5-14 is a profile of the velocity distribution for the various pressure-drop coefficients in the regenerator core. The velocities are negative because the flow is down through the regenerator and in the model that was used the positive direction is up. The more even the velocity distribution is the higher the pressure drop through the regenerator must be. The maximum difference in specified pressure drop is a factor of three, from 2000 Pa to 6000 Pa.

Figure 5-15 plots the maximum and minimum velocity for each curve in figure 5-14 against the pressure drop in a regenerator passage for a velocity of 10.5 m/s through the passage. This is the pressure drop that would occur in the regenerator, under the given conditions, if the flow was uniformly distributed. The trend shows that between 7000 and 9000 Pa pressure drop the maximum and minimum velocities will be approximately 10.5 m/s, yielding essentially uniform flow. For a pressure drop as low as 2000 Pa the difference between the maximum and minimum velocities is 50% of the minimum velocity. Therefore the pressure drop through the regenerator core has a very large impact on the flow distribution.

5.3.6 Turning Vanes

One of the major causes of the flow maldistribution in the previous tests is the fact that the flow must make a sharp 180° turn to pass through the regenerator. This requires too large of a pressure gradient and therefore separation occurs at the very right-hand side of the regenerator core. This can be noticed in all velocity and pressure graphs because the velocity drops off sharply in this region and the pressure is lower due to the recirculation that occurs. The two methods that were studied to remedy this, reducing the angle of the turn and adding turning vanes, produced similar results. In both types of simulations the velocity distribution was significantly improved over similar geometries that did not have these modifications.

The tests with varying angles for the incoming flow are represented by figure 3-17. The velocity and pressure distributions are presented in figures 5-16 and 5-17. The 90° angle refers to the case with the flow coming in horizontally at the inlet and the 0° case refers to the flow being vertical at the inlet. This angle produces significant

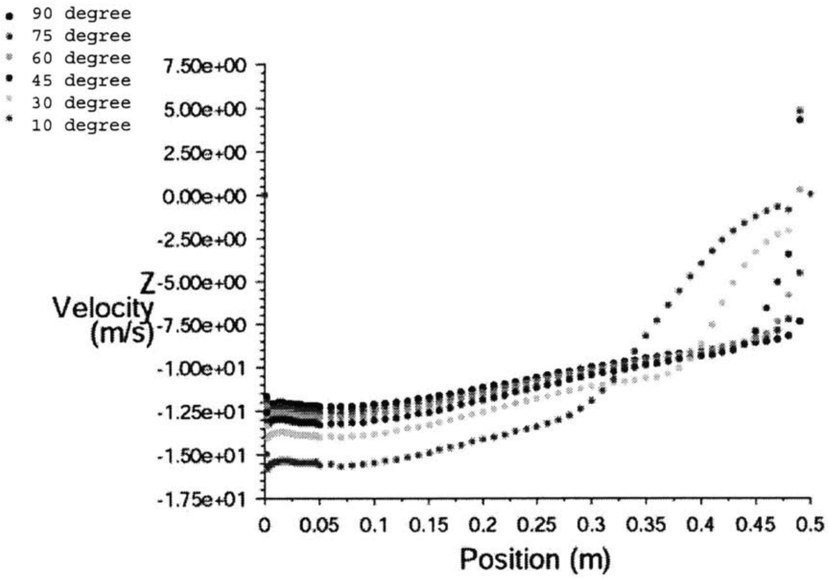

Figure 5-16: Z-Velocity Comparison at Regenerator Inlet for Various Flow Inlet Angles

changes in the flow distribution. The most important feature is the disappearance of the recirculation as the angle increases. The recirculation is the major disruption in the flow across the regenerator; eliminating this is essential to obtaining a uniform distribution. These tests show that one way of accomplishing that is to have the flow enter the inlet horizontally.

Another method of eliminating recirculation is to add turning vanes into the quarter turn before the flow enters the header. Two methods were studied: with and without a settling length after the turn. The settling length will ensure that no upward momentum of the flow will enter the header from the inlet turn, but is costly in terms of space and manufacturing. The more economical approach is to install turning vanes only into the turn itself. The no-settling-length approach provides an almost identical flow distribution to the settling-length tests as shown in figures 5-19 and 5-20.

Figure 5-18 shows the surfaces that are labeled as inlet stations zero through three in figure 5-19. The flow initially enters the model on the lower right-hand side at inlet

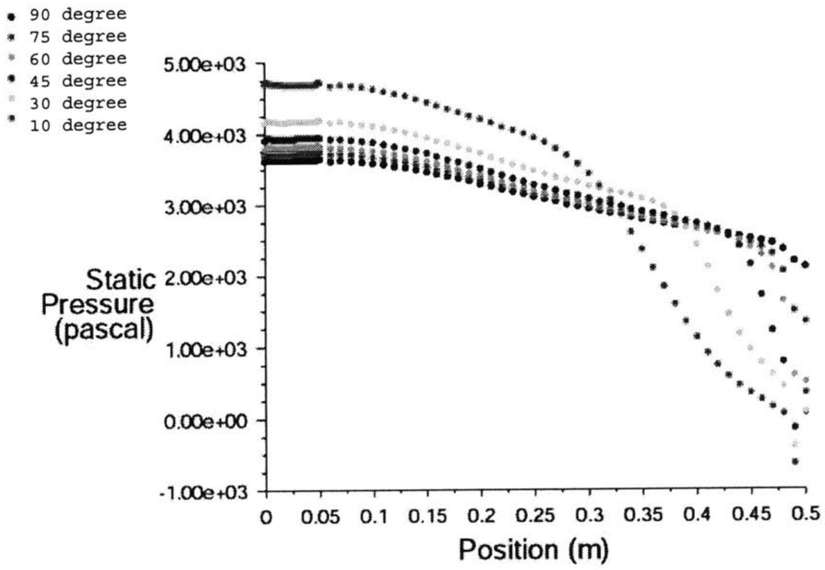

Figure 5-17: Pressure Comparison at Regenerator Inlet for Various Flow Inlet Angles

0. Moving counter-clockwise the inlets are 1, 2 and 3. Figure 5-19shows the average static pressure on each face for both the settling-length and no-settling-length tests. The pressures are almost identical in either case; the largest difference is at inlet 0 and is only 0.8% of the pressure in the no-settling-length test. The pressure drop that occurs from inlet 0 to 1 is due to the boundary-layer growth along the inlet pipe. The pressure drop from inlet 1 to 2 is much greater because of the multiple passages between turning vanes. This results in a much higher percentage of the flow area being occupied by boundary layers and hence a much higher pressure drop. The pressure recovery from inlet 2 to 3 is a result of the header acting like a diffuser. The average velocity entering the domain is about 42 m/s; the average velocity entering the regenerator at inlet 3 is 10.5 m/s. The loss of dynamic head contributes to the recovery in static pressure.

Figure 5-20 shows the velocity profile at the regenerator inlet, or inlet 3. The profiles are very similar, with the no-settling-length test having an average of 0.285 m/s, or 2.5%, higher velocity than the settling-length test. The two profiles begin to differ at the upwind side of the regenerator face. The no-settling-length test shows a

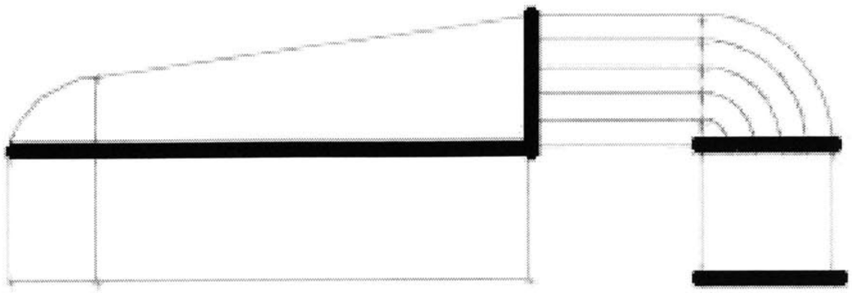

Figure 5-18: Profile Highlighting Inlet Stations for Pressure Comparison Between Settling-Length and No-Settling-Length Tests

sharp increase in the downward velocity, suggesting that there might be some sort of recirculation still occurring albeit on a smaller scale than in other simulations.

The settling-length method was compared to the identical inlet-header-shape test without turning vanes or a reduced inlet angle. The results shown in figures 5-21 and 5-22 emphasize the improvements in flow distribution that can be achieved through adding turning vanes.

The two methods were compared with each other, using the test with a settling length to compare to the 90° inlet test. Figures 5-23 and 5-24 demonstrate that the two methods produce approximately equal flow distributions.

5.3.7 Inlet-Header Shapes

The contour of the header itself is an important factor in determining flow distribution. There were two types of comparisons with different header contours. The first was to pick a contour and make slight variations; the second is to pick significantly different contours and compare them.

The geometry that was used for comparison of small differences was that in figure 3-22. The velocity and pressure distributions are shown in figures 5-25 and 5-26. As the space between the contour and the regenerator face becomes larger a sharp increase in velocity forms. This increase in velocity is due to the increase in size of the

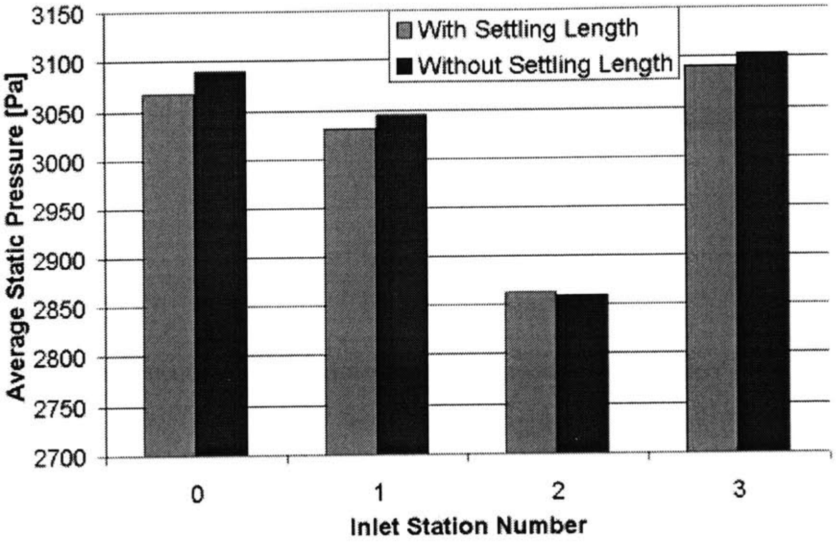

Figure 5-19: Pressure Comparison at Various Inlets for Settling-Length and No-Settling-Length Tests

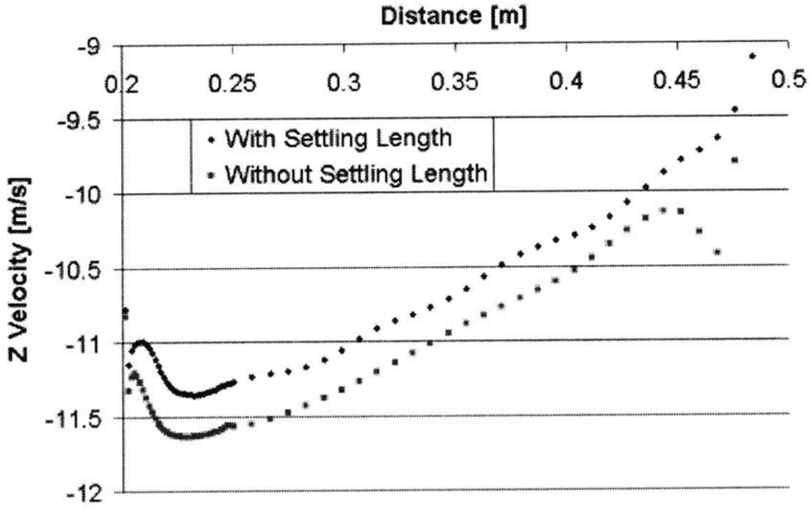

Figure 5-20: Z-Velocity Comparison at Regenerator Inlet for Turning Vane With Settling-Length Test and No-Settling-Length Test

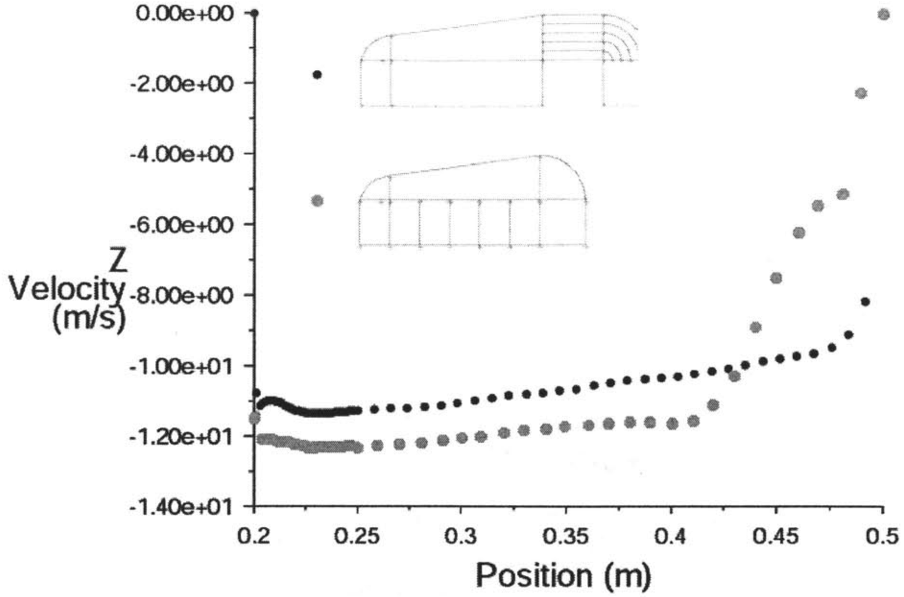

Figure 5-21: Z-Velocity Comparison at Regenerator Inlet for Turning Vane With Settling-Length Test and No Turning Vane Test

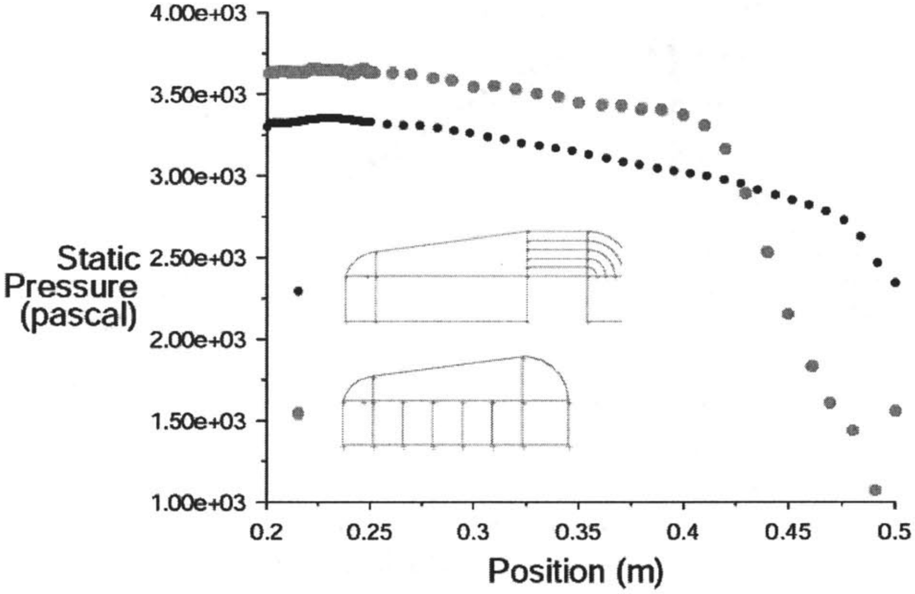

Figure 5-22: Pressure Comparison at Regenerator Inlet for Turning Vane With Settling-Length Test and No-Turning-Vane Test

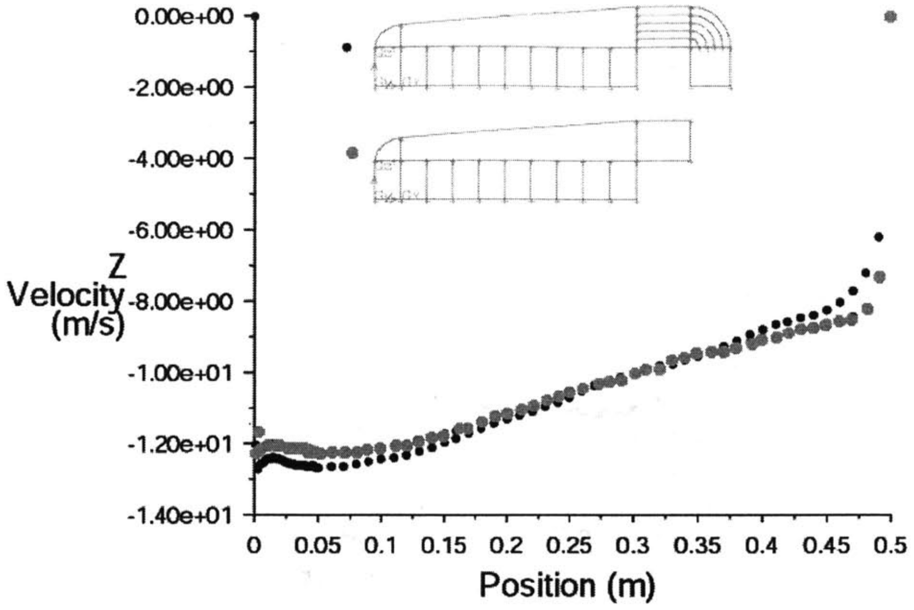

Figure 5-23: Z-Velocity Comparison at Regenerator Inlet for Turning Vane With Settling-Length Test and Horizontal-Inlet-Flow Test

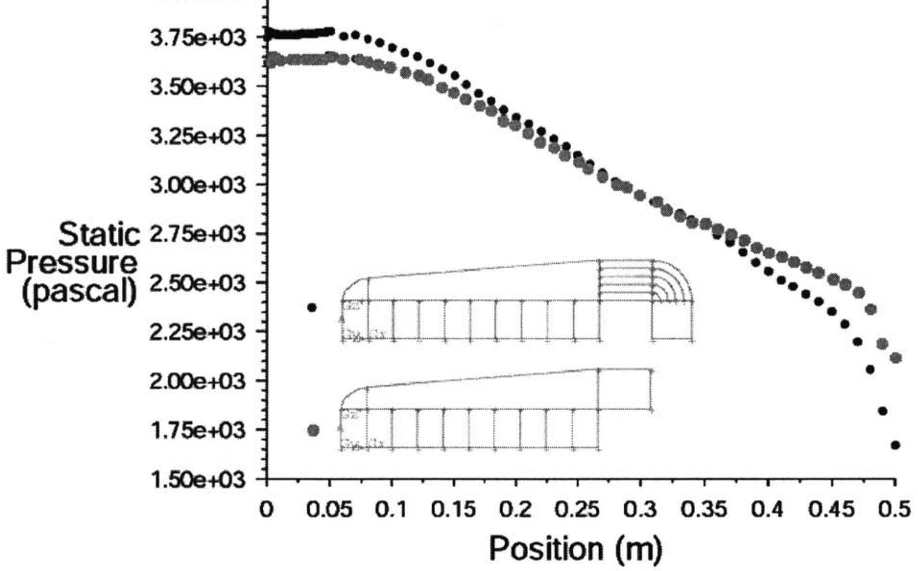

Figure 5-24: Pressure Comparison at Regenerator Inlet for Turning Vane With Settling-Length Test and Horizontal-Inlet-Flow Test

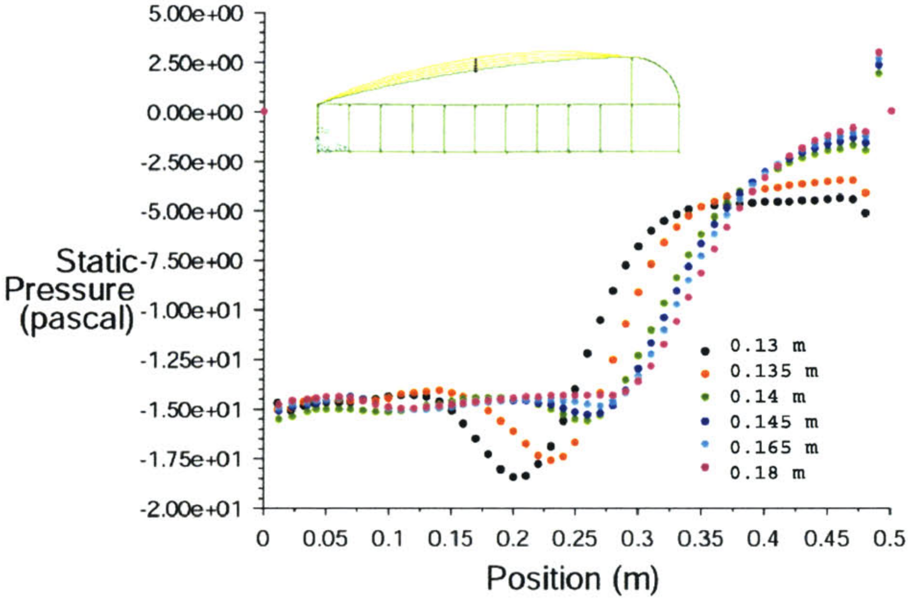

Figure 5-25: Z-Velocity Comparison for Tests with Slight Changes in Header Contour

vortex at the regenerator face. As the vortex grows, which it does as the header moves farther up, it "pinches" off the flow above. The flow then is essentially turned into a jet impinging on the surface of the regenerator. The change in curvature of the header contour also makes the jet impinge more directly on the regenerator inlet rather than the more oblique impingement for the lower-height cases. These impingement effects can be ascertained by the spike in velocity in figure 5-25. The velocity profiles in the model for the two extreme cases in figure 5-25 are shown in figures 5-27 and 5-28.

In figures 5-27 and 5-28 the recirculation vortex and the impingement of the "jet" on the regenerator are clear.

Even though the effect of the recirculation is magnified by the changes in header contour, the overall flow distribution follows a consistent pattern. That pattern is determined by the general form of the header contour more than its specific dimensions.

The comparisons between generally different header shapes revealed that there is a significant change in flow distribution when varying the contours. Figures 5-29 and 5-30 show the velocity and pressure distributions for the four different contours

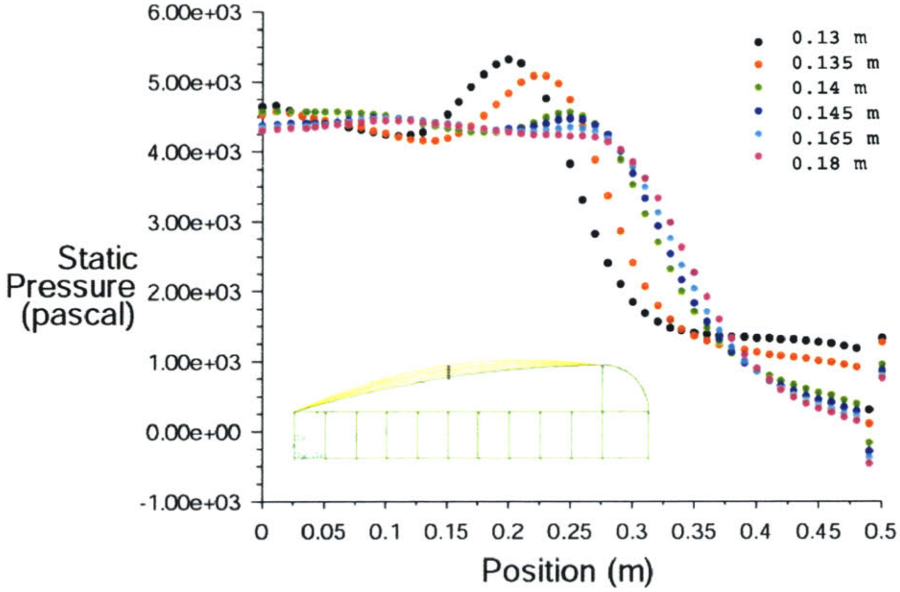

Figure 5-26: Pressure Comparison for Tests with Slight Changes in Header Contour

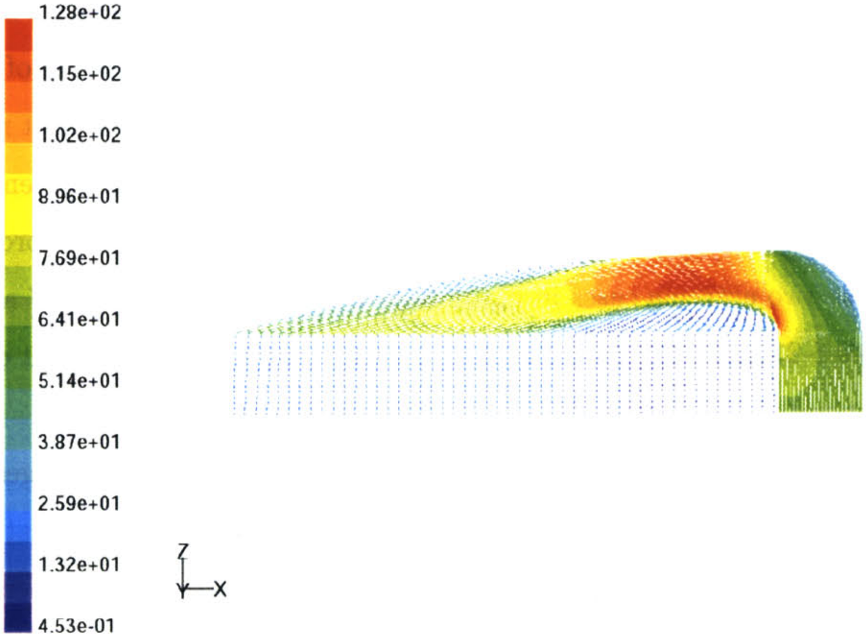

Figure 5-27: Velocity Profile for Simulation With Header 0.13 m Above Regenerator Face At Center

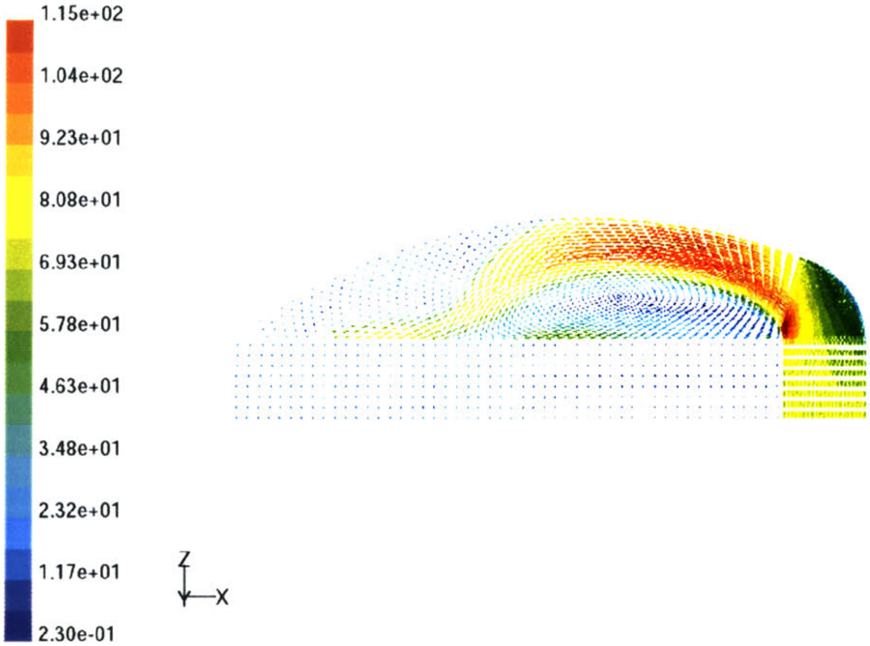

Figure 5-28: Velocity Profile for Simulation With Header 0.18 m Above Regenerator Face At Center

tested.

The most even distribution is from the geometry with a circular arc contour. Two of the geometries are similar to ones that Kohler [24] experimented with. He found the opposite in terms of flow distribution. The s-shaped contours he found to give a fairly even flow distribution. The contour with the largest area he found to give a poor distribution. Some of the differences between this study and his are discussed earlier in this section. Kutchey and Julien [20] used a header that was roughly similar to the header that in this comparison has the most even distribution; they also found this to provide improved distribution over a header somewhat similar to the one with the largest area underneath in this figure.

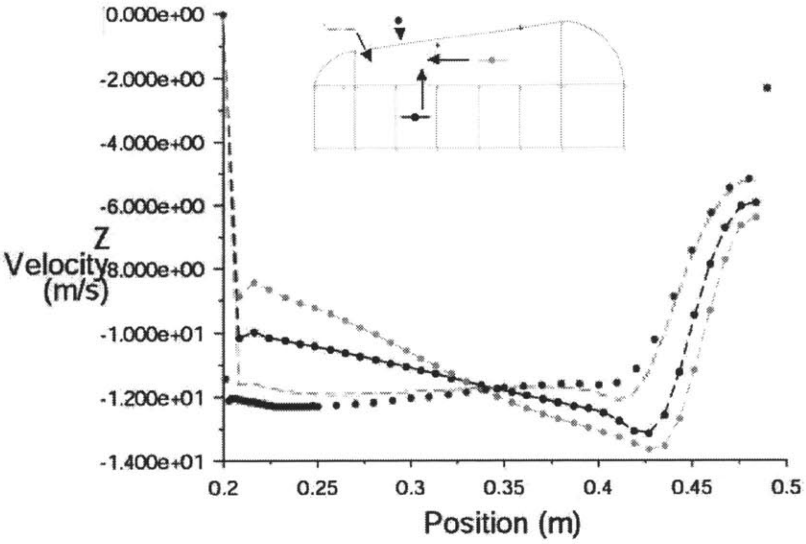

Figure 5-29: Velocity Profile for Simulation With Header 0.13 m Above Regenerator Face At Center

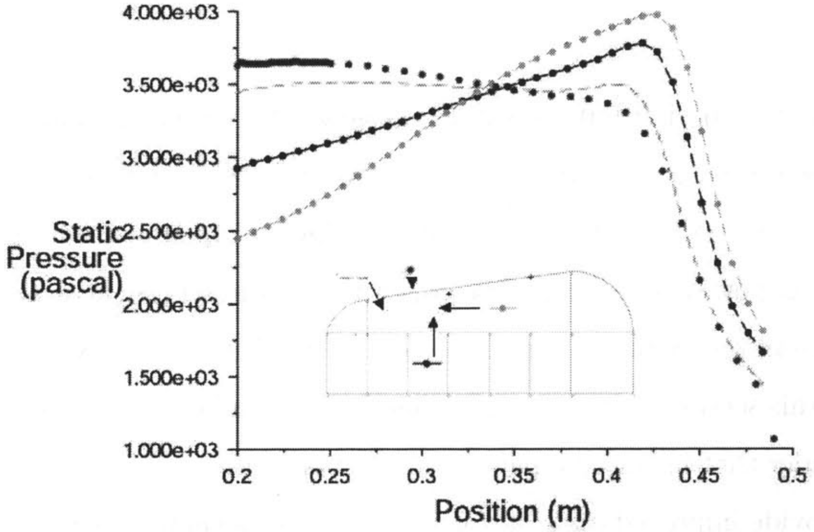

Figure 5-30: Velocity Profile for Simulation With Header 0.18 m Above Regenerator Face At Center

Chapter 6

Conclusions

This study used numerical simulations using FLUENT to analyze the effect of manufacturing inaccuracies and inlet-header design on heat-exchanger effectiveness. Three basic models were simulated:

- two-passage model with center wall deviation;
- single-passage model with corner roundoff;
- section of heat-exchanger core with inlet header

The single and two-passage models added heat through the walls to the fluid; the inlet-header design models added no heat transfer and instead provided a profile of the flow distribution into the regenerator core.

6.1 Two-Passage Models

The two-passage models showed that even large deviations had little effect on the mass-averaged effectiveness of the passages. Three different aspect ratios with center-wall offsets were compared to the results of Shah and London [11] with good accuracy to establish the numerical modeling technique. The nominally square-passage tests were selected and modified with a center-wall offset deviation, a deviation that changed along the flow direction and also a center-wall wavy deviation. These tests all had walls that heated the fluid, variable properties and constant overall, fully developed mass flow.

The net effect on a cyclical heat exchanger of variable properties as opposed to properties at bulk average temperature is negligible. Variable-property effects were quantified by simulating the nominally square-passage tests with offset center walls with properties specified at the average bulk fluid temperature. These tests were compared to the tests with variable properties. Specification of variable properties showed that, when heating the fluid, having variable properties resulted in a slightly higher effectiveness. When cooling the fluid the variable properties gave a slightly lower effectiveness.

Modeling passages that cooled the fluid resulted in the same small changes in effectiveness for large deviations. The opposite wall temperature conditions were imposed on the model for the nominally-square, two-passage geometry and the same trends in effectiveness vs. channel deviation were observed as with the heated cases.

Future Work

Future work with these tests should be focused on extending the range of non-uniformities, modeling more passages and varying the boundary conditions. There are other types of non-uniformities that might arise while manufacturing ceramic-heat-exchanger cores. For example surface roughness or gas bubbles, possibly burst, could form during the cooling process with varying frequency. These could form in addition to other non-uniformities. Modeling multiple uniformities simultaneously was not undertaken in this study. More work in this area might show that a simple superposition of the effects does not adequately reflect actual behavior.

Modeling more passages would be useful because different frequencies and magnitudes of non-uniformities could be modeled together in a range of ratios rather than 1:1. This would also be helpful in evaluating the impact of non-uniformities on each other. Modeling dozens or hundreds of passages is also more realistic than just two. The edge effects could be minimized whereas, when modeling two passages, edge effects on the incoming flow (i.e. the adjustment of pressures at the passage inlets by the plenum chamber walls) could be significant. Simulating a model of a large number of passages could also result in modeling the turbulent flow into the passages and could tie into the inlet-header-design study as well.

Applying different boundary conditions such as the wall temperature and altering the mass flow rate need to studied. The wall temperature was set based on a typical rotary-regenerator temperature distribution. If a particular system has different operating temperatures this could change whether any manufacturing inaccuracies have a large impact on the effectiveness. Using constant wall temperatures or different temperature gradients along the passage length should be studied so that a more generalized recommendation on the effects non-uniformities can be formed. One method of accomplishing this would be to use a time-dependent model that incorporates the heat capacitance of the walls and both the heating and cooling cycles as in a rotary regenerator. Less a priori knowledge is required to simulate this system and therefore artificial boundary conditions that can alter the flow and heat-transfer characteristics could be minimized. The drawback to this is the computational power required; this was far beyond the available capacity for these simulations.

The mass-flow rate into the tubes should be varied. The current mass flow rate was chosen so that the average velocity was comparable to a typical rotary regenerator. Some of the tests on the incidence effect indicated that a lower mass flow rate could reduce the change in effectiveness; similarly, a higher mass flow rate could exacerbate the effect.

6.2 Corner-Radii Tests

The single-passage models with rounded corners showed that changing the corner radius had little impact on the effectiveness given the somewhat artificial constant mass flow per unit area into the passage. The walls were heated with a constant temperature gradient along the passage length (0.075 m). The passage cross-section was nominally square with corner radii that varied between tests such that the cross-section changed from almost square to essentially circular with several test in between.

The heat transferred to the fluid, in contrast to the effectiveness, was decreased by 21.7% from the square cross-section to the circular one. If the excess mass flow that cannot flow into the smaller, more circular passages can be accommodated by neighboring tubes, then the same amount of heat will still be transferred to or from the heat-exchanger walls. If this is the situation, rounded corners do not inhibit the efficiency of a heat exchanger.

The pressure drop, when increasing the corner radius, increased by 9% from the square to the circular cross sections. The hydraulic-diameter concept was found to be inadequate for characterizing these cross-sections and it led to wildly inaccurate pressure-drop predictions for the nearly-square cross-sections. The theoretical prediction for the pressure drop through the square tube was overestimated by 30%. The theoretical pressure drop decreased as the corner radius increased in a fashion that mimicked the almost sinusoidal trend of the hydraulic diameter, which in itself is counterintuitive.

Future Work

In addition to the future work mentioned in the two-passage-model section, more work needs to be done in determining how to allow the code to determine the change in mass flow into a passage due to the corner size and allowing for different numbers and sizes of corner radii.

The mass-flow rate into the passages was arbitrarily set so that the mass flow per unit area was constant. This assumption is justified only if the excess fluid can be channelled into other passages with minimal pressure changes. If more passages were modeled with an inlet plenum chamber, the changes in mass flow from one corner-radius size to another would be determined from the equations of motion, not by the user.

The number of corners with roundoff and the size of the roundoff are not necessarily equal in reality. Changing the presence of one or more rounded corners and using multiple radii in a given test could provide a more detailed understanding of how this can affect the heat-exchanger efficiency.

6.3 Inlet-Header Tests

The inlet-header tests consisted of a slice of a heat exchanger with the flow coming from one side, being turned by the inlet header and forced through the exchanger core. No heat transfer was added; only the flow and pressure distributions into the regenerator were recorded. The results of the many simulations suggest the following:

- The basic header contour has a large impact on the flow and pressure distributions across the heat-exchanger face. The most even flow was achieved by a 90° turn at the header inlet with a straight-line contour with a slope of approximately -1/8 to the other end of the header followed by another 90° turn.

  Other shapes that had been showed to have produced better flow distribution by Kohler [59] did not produce as desirable a distribution in these simulations. The discrepancy could be due to the modeling of only a slice of heat exchanger, different mass flow rates or different relative dimensions of the core and header. It is difficult to tell because Kohler does not give the details of the flow rate and dimensions of his experiments.

- Small variations in the header contour make relatively little difference in the flow distribution. Several tests with the circular-arc contour showed that if the header was tweaked slightly but still had the same general shape the flow was approximately unchanged.

- The aspect ratio of the core and header has little effect on the flow distribution. Simulations that changed the aspect ratio of the core and header showed the same type of flow maldistributions, only stretched or compressed relative to a shorter or longer core, respectively.

- The angle of the inlet flow has a large effect on the flow distribution. Simulations that varied the angle of the inlet flow from the vertical to the horizontal showed that the area of recirculation near the edge of the core disappeared as the angle that the flow had to turn was reduced. A similar effect to horizontal inlet flow was achieved by implementing turning vanes in the first 90° turn. Turning vanes are attractive because often there are dimensional constraints that could prevent a horizontal incoming flow. Using turning vanes requires no redesign of the piping and regenerator location or size; a header without turning vanes could simply be replaced with a model including turning vanes and thereby create a more uniform flow distribution with minimal effort.

- The pressure drop through the heat-exchanger core has a significant effect on the flow distribution. As the pressure drop through the core increases it forces the flow to be more evenly distributed. This can be utilized in conjunction with header contour and turning vanes to achieve the most uniform flow possible. Having a higher pressure drop in the compressed-air side of a rotary regenerator generally doesn't interfere with the system design. However, introducing a higher pressure drop in the exhaust gas side could be more problematic. The exhaust gas is exposed to atmospheric pressure at the heat-exchanger outlet. Therefore altering the pressure drop through the core requires changing the pressure at which the exhaust leaves the engine, reducing the engine efficiency. This limits the use of adjusting core pressure drop arbitrarily to the compressed-air side in a gas-turbine heat exchanger.

Future Work

More effort in the area of header design and simulation should be in the area of a more accurate, three-dimensional model of the header. Modeling a thin slice of a regenerator is faster computationally, but curvature of the regenerator and header most likely create somewhat different flow distributions than those modeled here. The trends seen here can probably be generalized but the specific flow patterns could possibly change significantly when a more-accurate three-dimensional model is used.

Heat transfer was not modeled here because of the use of the porous medium to represent the regenerator core. Modeling all the passages would allow for a more detailed look at the inlet conditions for each passage, allow for wall heat transfer to be modeled and also enable passage non-uniformities to be incorporated into the simulation.

More header shapes need to be modeled. The contours used here are only representative of the header designs that exist and perhaps others can also yield acceptable flow distributions given the proper conditions.

The outlet headers have not been modeled in these simulations. The outlet conditions were specified as a uniform-pressure at the core outlet. This might not hold true for all outlet headers. The outlet headers can also be used to vary the effective pressure drop through the core rather than changing passage dimensions, but quantifying these effects would require additional research.

Appendix A

Fluid Modeling Calculations

Incompressible Ideal-Gas Model

All simulations used variable properties except for the constant-property tests used to quantify the differences in effectiveness between the two methods. In the variable-property method, the density was specified according to what FLUENT calls an incompressible ideal-gas

$$\rho = \frac{P_{ambient}}{RT} \tag{A.1}$$

This approximation to the ideal-gas model is simpler computationally because the ambient pressure is specified by the user and is a constant that does not have to be calculated and adjusted locally as with the ideal-gas model. The term incompressible is somewhat misleading, it does not imply that the density is constant, only that ambient pressure is used in lieu of local pressure. Using the incompressible ideal-gas approximation can be justified if the internal pressure does not change much from ambient (atmospheric) pressure. In this case the difference in density compared to an ideal gas specification is minimal.

In many of the simulations performed in this study the gauge pressure can be as high as 50% above ambient pressure. It was decided to use the incompressible ideal-gas method regardless because of the computational expense that was saved. The objective of these simulations was not so much to have the precise efficiencies that would be observed in reality, but rather to quantify differences between these tests.

Since all tests used the incompressible ideal-gas method, they all have the same bias and hence it will not affect the comparisons.

Kolmogorov Length Scale

The inlet header tests used turbulence models to solve for the flow field. The resolution of the mesh was not sufficient to capture the Kolmogorov length scale of the turbulence. The Kolmogorove scale is the smallest length scale of turbulence that is encountered in a flow. It is calculated as follows [48]

$$\lambda_k \sim \frac{\nu^{3/4} L^{1/4}}{V^{3/4}} \tag{A.2}$$

where V is the average velocity and L is the characteristic length scale of the flow geometry. The length scale of the flow geometry is the hydraulic diameter of the passage, 0.13 m for the header tests, and the average velocity varied from 42 m/s to 70 m/s depending on the aspect ratio of the header. The kinematic viscosity of air at atmospheric pressure and 525°K is 42.18e-6 m^2/sec. This gives a Kolmogorov length scale in the range of

$$1e-6m \lesssim \lambda_k \lesssim 2e-5m \tag{A.3}$$

The smallest mesh dimension in the inlet header simulations was 2e-3 m. The computational expense of resolving the flow down to the Kolmogorov scale was prohibitive. Since the average flow distribution was the desired feature for these simulations, the Kolmogorov scale was deemed not important enough to justify the extra time.

Incompressibility Calculations

Modeling the streamline-curvature effects on the two-passage model inlet pressures utilized an assumption of incompressibility. Assuming incompressibility of a fluid is considered acceptable if the Mach number is below 0.3. The speed of sound in an ideal gas is given by

$$c = \sqrt{\gamma R T} \tag{A.4}$$

where γ is equal to 1.4 for a diatomic gas, R is the gas constant equal to $287 m^2/s^2 K$ for air and T is the temperature of the gas in degrees Kelvin, approximately 525°K.

The speed of sound at the two-passage model inlets is

$$c = \sqrt{1.4 \cdot 287 \cdot 525} = 459.3m/s \tag{A.5}$$

The Mach number is defined as

$$Ma = \frac{v}{c} \tag{A.6}$$

In these simulations the typical velocity, v, is 10 m/s. The Mach number is therefore

$$Ma = \frac{10}{459.3} = .218 \tag{A.7}$$

justifying the incompressible-fluid assumption.

Appendix B

Entrance and Exit Loss Coefficients

The entrance and exit pressure-loss coefficients for a multiple-square-tube heat exchanger core with abrupt-contraction entrance abrupt-expansion exit taken from Kays and London [38]. The coefficients used in equation 2.1 to predict the pressure-drop through the tubes analytically were obtained from this figure.

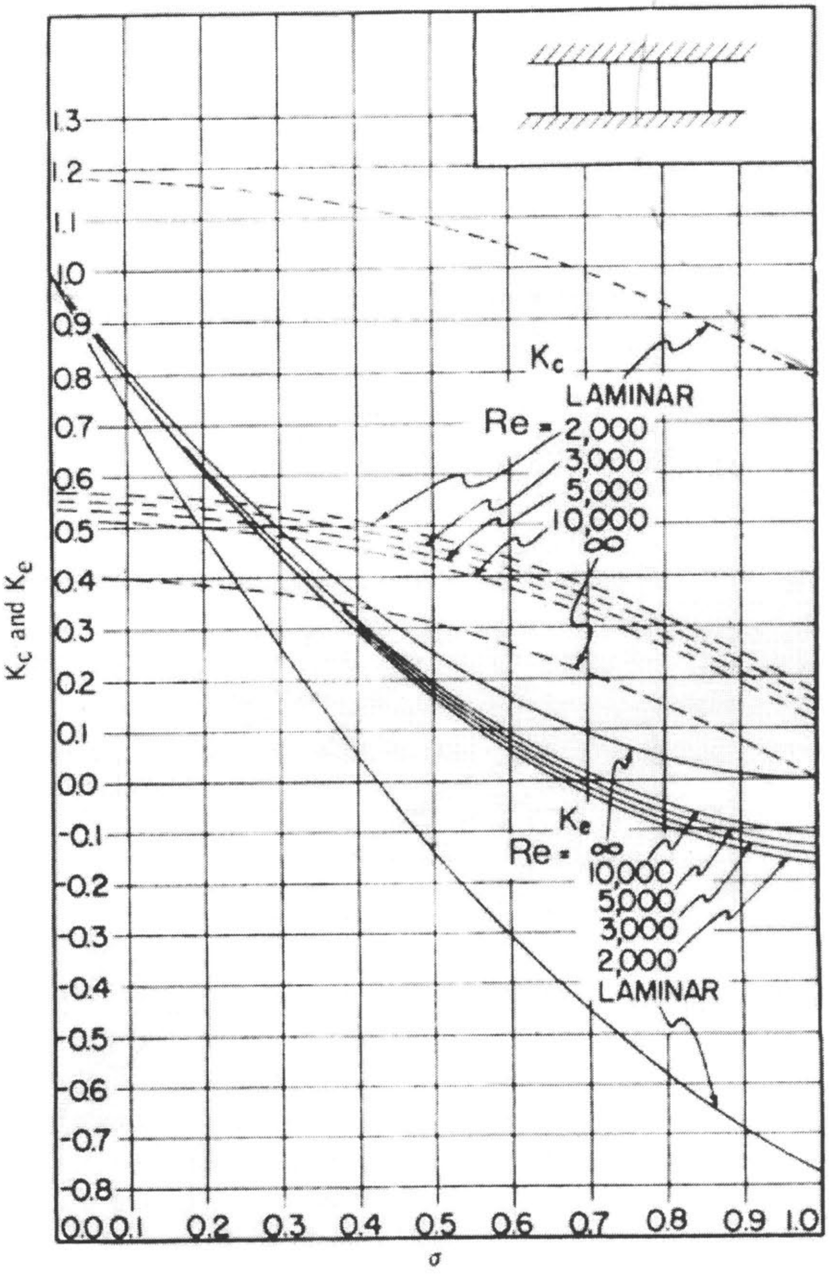

Figure B-1: Entrance and Exit Pressure-Loss Coefficients from Kays and London [49]

Appendix C

Reynolds-Number Calculations

The flow regime in the two-passage and the rounded-corner simulations was treated as laminar, while the inlet header tests were modeled as turbulent.

The laminar cases all averaged 10 m/s over the entire inlet. For configurations with large deviations, a disproportionate amount of the fluid flowed through the large chamber, raising the Re number in the large passage and lowering it in the smaller passage. The Reynolds number is so low that there is no turbulence present even in these large deviation cases. The inlet properties of air at atmospheric pressure and 525°K are:

$\rho = 0.665 kg/m^3$

$\mu = 279e - 7 kg/ms$

The outlet properties of air at atmospheric pressure and 1150°K are:

$\rho = 0.3034 kg/m^3$

$\mu = 472e - 7 kg/ms$

The range of Re numbers for a square-passage is

$$32 \lesssim Re_{D_h} \lesssim 119 \tag{C.1}$$

Clearly even with a larger hydraulic diameter as with a rectangular or square cross-section with corner rounding there is no turbulence at all in these passages.

The inlet header tests were all simulated at 525°K. The properties are the same as listed above with a characteristic length at the inlet of 0.075 m. The velocity at the inlet varies with the aspect ratio from 42 m/s to 70 m/s. This gives a range of Re at the inlet of

$$75,080 \lesssim Re_{L_{ch}} \lesssim 125,134 \tag{C.2}$$

The turbulent assumption is therefore justified.

Appendix D

Square Vs. Rectangular Cross-Sections

Traditional heat-exchanger cores, whether deep-fold metallic or ceramic, have used rectangular passage cross-sections. In this study the square has been used as the standard cross-section. This is because the square yields higher overall convective heat transfer given equal outside dimensions as other aspect ratios. Table D.1 shows the Nusselt number for fully developed flow from [49] and the overall heat transfer coefficient calculated at 525°K for passages with equal outside surface areas. The 1:1 aspect ratio includes four passages to equal the outside surface area of one 8:1 aspect ratio passage, and/or two 4:1 passages. All passages are 0.05 m long. This comparison was chosen so that if a given minimum dimension, d, is determined, perhaps for manufacturing reasons, each set of passages could fit into the same space if the wall thicknesses are neglected. The square passages clearly provide better heat transfer and are used as the base cross-section for the majority of tests in this study.

Table D.1: Overall Heat-Transfer Coefficients for Square and Rectangular Cross-Section Passages

Aspect Ratio	1:1	4:1	8:1
Nu_H	3.61	5.33	6.49
D_h (short dim.: d=5e-4 m)	d	$\frac{8}{5}d$	$\frac{16}{9}d$
$\bar{h}$	305.4 $\frac{W}{mK}$	281.8 $\frac{W}{mK}$	308.8 $\frac{W}{mK}$
$\bar{h}A_T$	0.122 $\frac{W}{K}$	0.07 $\frac{W}{K}$	0.069 $\frac{W}{K}$

Bibliography

[1] *members.aol.com/panzersgt/theory/theory.html.*

[2] *Chattanooga Daily Times*, www.roanetnheritage.com/c&p/cardiff/index.htm, July 18 1890.

[3] Open hearth process. *Encyclopaedia Brittanica ed. 15, Vol 8*, pages 962–963, 1998.

[4] M. Wolfshtein A.K. Runchal. Numerical integration procedure for the steady state navier-stokes equations. *J Mech Eng Science*, 11:445, 1969.

[5] O. Pironneau B. Mohammadi. *Analysis of the k-ϵ Turbulence Model.* Wiley, Chichester, U.K., 1994.

[6] D.B. Spalding B.E. Launder. *Mathematical Models of Turbulence.* Academic Press, New York, NY, 1972.

[7] D.S. Beck. Regenerator efficiency during transient operation. *J. of Eng. for Gas Turbines and Pwr*, 118:661–667, July 1996.

[8] K.V. Sreevatsan C. Ranganayakulu, K.N. Seetharamu. The effects of inlet fluid flow nonuniformity on thermal performance and pressure drops in crossflow plate-fin compact heat exchangers. *Int. J. Heat Mass Transfer*, 40(1):27–38, 1997.

[9] S. Thangam C.G. Speziale. Analysis of an rng based turbulence model for separated flows. *Int. J. Engng. Sci.*, 30(10):1379–1388, 1992.

[10] J.P. Day. Attap extruded ceramic regenerator disk development. In *Proceedings of SAE, nP-256*, pages 37–44, Warrendale, PA, 1993. SAE.

[11] J.P. Day. A rotary heat exchanger for automotive and other ground based gas turbines. In *Int. Gas Turbine and aeroengine Congress and Exposition, The Hague, Netherlands- June 13-16, 1994*, number 94-GT-124, pages 1–9. ASME, 1994.

[12] E.P. DeGarmo. *Materials and Processes in Manufacturing.* Macmillan, New York, NY, 1974.

[13] A. C. Pfahnl D.G. Wilson. A look at the automotive-turbine regenerator system and proposals to improve performance and reduce cost. In *SAE International Congress and Exposition, Detroit, MI Feb. 24-27, 1997*, Warrendale, PA, 1997. SAE.

[14] P.L. Sorrell D.W. Wendland, W.R. Matthes. Effect of header truncation on monolith converter emission-control performance. In *SAE International Fuels and Lubricants Meeting and Exposition San Fransisco, CA Oct. 19-22, 1992*, Warrendale, PA, 1992. SAE.

[15] James A. Fay. *Introduction to Fluid Mechanics.* MIT Press, Cambridge, MA, 1994.

[16] FLUENT Inc., Lebanon, NH. *FLUENT 5 Manual*, 1999.

[17] D.P. DeWitt F.P. Incropera. *Fundamentals of Heat and Mass Transfer.* Wiley, New York, NY, 1996.

[18] D.N. Assanis G.C. Papageorgakis. Comparison of linear and nonlinear rng-based k-ϵ models for incompressible turbulent flows. *Numerical Heat Transfer, Part B*, 35:1–22, 1999.

[19] Inst of Prof Engrs New Zealand. *Energy Performance of Swimming Pools*, 1996.

[20] H.L. Julien J.A. Kutchey. The measured influence of flow distribution on regenerator performance. *SAE*, (740164), 1974.

[21] et al K. Kawasaki, T. Matsuhisa. Heat transfer characteristics of rotating ceramic regenerators-numerical solution using a hybrid finite difference/laplace transform scheme. In *ASME Gas Turbine and aeroengine Congress and Exposition, Orlando, FL June3-6 1991*, New York, NY, 1991. ASME.

[22] S. Kalpakjian. *Manufacturing Engineering and Technology.* Addison-Wesley, Reading, MA, 1995.

[23] S.H. Wong K.C. Leong, K.C. Toh. Microcomputer-based design of rotary regenerators. *Heat Recovery Systems and CHP*, 11(6):461–470, 1991.

[24] M. Kohler. The inlfuence of flow path geometry and manufacturing tolerances on gas turbine regenerator efficiency. *SAE*, (740183), 1974.

[25] J.G. Lanning. The status and future of ceramic rotary regenerator cores and recuperators. In *Ceramic Materials and Components for Engines, Proceedings of the Second International Symposium. Luebeck-Travemuende, West Ger. 19860414-19860417. Conference Code: 09111*, pages 1073–1080, Bad Honnef, West Ger., 1986. Verlag Deutsche Keramische Gesellschaft.

[26] A.L. London. Laminar flow gas turbine regenerators-the influence of manufacturing tolerances. *Journal of Engineering for Power, Trans. ASME, Series A*, 92:46–56, January 1970.

[27] G. Mompean. Numerical simulation of a turbulent flow near a right-angled corner using the speziale non-linear model with rng k-ϵ equations. *Computers and Fluids*, 27(7):847–859, 1998.

[28] J.R. Mondt. Effects of nonuniform passages on deepfold heat exchanger performance. *Journal of Engineering for Power*, 99:657–663, October 1977.

[29] et al N. Nakazawa, S. Inaba. The turbine components development for the 100kw automotive ceramic gas turbine. In *Int. Gas Turbine and aeroengine Congress and Exposition, Cincinnati, Ohio-May 24-27, 1993*, number 93-GT-64, pages 1–10. ASME, 1993.

[30] A.J. Organ. Analysis of the gas turbine rotary regenerator. In *Proc Instn Mech Engrs Part D*, volume 211, pages 97–111, 1997.

[31] Patankar. *Numerical Heat Transfer and Fluid Flow.* McGraw-Hill, New York, NY, 1980.

[32] J. Sismey R. Wilson. *www.maisonblanche.co.uk/roverbrm.html.*

[33] D.W. Richerson. Ceramics for gas turbines. *Mechanical Engineering Magazine*, Sept. 1997.

[34] A.L. London R.K. Shah. *Lmainar Flow Forced Convection In Ducts: A Source Book for Compact Heat Exchanger analytical Data.* Academic Press, London, U.K., 1978.

[35] A.L. London R.K. Shah. Effects of nonuniform passages on compact heat exchanger performance. *Journal of Engineering for Power*, 102:653–659, July 1980.

[36] F. Mayinger S Kakac, A.E. Bergles, editor. *Heat Exchangers-Thermohydraulic Fundamentals and Design.* Hemisphere Publishing Corp., Washington, D.C., 1981.

[37] D. Choudhury S. Kim. A near-wall treatment using wall functions sensitized to pressure gradient. In *FED-Vol.217, Separated and Complex Flows, ASME 1995*, pages 273–280, New York, NY, 1995. ASME.

[38] et al S. Lalot, P. Florent. Flow maldistribution in heat exchangers. *Applied Thermal Engineering*, 19:847–863, 1999.

[39] et al T. Shih, W. Liou. A new k-ϵ eddy viscosity model for high reynolds number turbulent flows. *Computers and Fluids*, 24(3):227–238, 1995.

[40] Charles Tomlinson, editor. *Cyclopedia of Useful Arts, Mechanical and Chemical, Manufacturing, Mining and Engineering.* Virtue and Co., London, 1866.

[41] T. Yang T.P. Lewandowski. A procedure to reduce the effects of variable fluid temperatures in the flow direction: Application to the design of a rotary regenerator. Technical report, Clemson University, 1988.

[42] L.M. Smith V. Yakhot. The renormalization group, the ϵ-expansion and derivation of turbulence models. *J. Scientific Computing*, 7:35–61, 1992.

[43] S.A. Orszag V. Yakhot. Renormalization group analysis of turbulence, basic theory. *J. Scientific Computing*, 1:3–51, 1986.

[44] D.W. Wendland. Reducing catalytic converter pressure loss. *Automotive Engineering*, pages 69–74, June 1996.

[45] D.G. Wilson. A method of design for heat-exchanger inlet headers. In *ASME Heat Transfer Division Winter Annual Mtg., New York, NY, Nov. 27-Dec. 1, 1966*, pages 1–9, New York, NY, 1966. ASME.

[46] D.G. Wilson. U.s. patent #5,259,444 heat exchanger containing a component capable of discontinuous movement. November 5 1990.

[47] D.G. Wilson. Low-leakage and high-flow regenerators for gas turbine engines. *Journal of Power and Energy*, 207:195–202, 1993.

[48] D.G. Wilson. A new approach to low-cost high-efficiency automotive gas turbines. In *SAE International Congress and Exposition, Detroit, MI Feb. 24-27, 1997*, Warrendale, PA, 1997. SAE.

[49] A.L. London W.M. Kays. *Compact Heat Exchangers.* McGraw-Hill, New York, NY, 1984.

[50] P. Chen Z. Chang. Flow channeling effect on a regenerator's thermal performance. *Cryogenics*, 38:191–196, 1998.